

**Fabrication Characteristics and Performance Enhancement of  
 $\text{Nb}_{18}\text{W}_{16}\text{O}_{93}$  and  $\text{MoNb}_{12}\text{O}_{33}$  Nanowires for Lithium-Ion Batteries**

**Application**

FATILE BABAJIDE OLUWAGBENGA

A Thesis

In the Department

Of

Mechanical, Industrial and Aerospace Engineering

Presented in Partial Fulfilment of the Requirements for the Degree of

Doctor of Philosophy in Mechanical Engineering

at

Concordia University

Montreal, Quebec, Canada

June 2023

**Concordia University**  
**School of Graduate Studies**

This is to certify that the thesis prepared

By: Babajide Oluwagbenga Fatile

Entitled: Fabrication Characteristics and Performance Enhancement of Nb<sub>18</sub>W<sub>16</sub>O<sub>93</sub> and MoNb<sub>12</sub>O<sub>33</sub> Nanowires for Lithium-Ion Batteries

And submitted in partial fulfilment of the requirements for the degree of

**DOCTOR OF PHILOSOPHY (Mechanical Engineering)**

Complies with the regulations of the University and meets the accepted standards with respect to originality and quality.

Signed by the final examining committee:

_____	Chair
Dr. Pantcho Stoyanov	
_____	External Examiner
Dr. Xiaolei Wang	
_____	External to Program
Dr. Xia Li	
_____	Examiner
Dr. Charles Kiyanda	
_____	Examiner
Dr. Farjad Shadmehri	
_____	Thesis Supervisor
Dr. Mamoun Medraj	
_____	Thesis Supervisor
Dr. Martin Pugh	

Approved by \_\_\_\_\_

Chair of Department of Graduate Program Director

September 2023 \_\_\_\_\_

Chair of Department of Graduate Program Director

## Abstract

### **Fabrication Characteristics and Performance Enhancement of Nb<sub>18</sub>W<sub>16</sub>O<sub>93</sub> and MoNb<sub>12</sub>O<sub>33</sub> Nanowires for Lithium-Ion Batteries Application**

**Fatile Babajide Oluwagbenga, PhD**

**Concordia University, 2023**

To date, graphite is widely employed as an anode material for Lithium-ion batteries (LiBs) because it has demonstrated superior cycling stability and high specific capacity in comparison with other potential anode materials. However, the use of graphite as an anode material in LiBs has been limited by its safety concern as well as low energy density. Thus, it is imperative to develop a new anode material to address these shortcomings. To this end, niobium-based oxide nanowires had been proposed as one of the alternative materials as a potential anode for LiBs. These materials have demonstrated high theoretical capacity, significant structural stability, high power density, and environmental friendliness. Furthermore, the enhanced performance of nanowires compared to their bulk counterparts as a material for LIBs anodes has motivated researchers to focus more attention on nanowires. Nevertheless, the kinetics of electrochemical reactions in these compounds is hindered by their intrinsically poor electronic conductivity and electron transfer properties. These tend to be significant flaws restricting their practical use in LIBs. More so, it is desirable to enhance its electrochemical performance to meet the needs of current energy applications. Consequently, investigations are carried out on two niobium based compounds namely niobium tungsten oxide (Nb<sub>18</sub>W<sub>16</sub>O<sub>93</sub>) and niobium-molybdenum oxide (MoNb<sub>12</sub>O<sub>33</sub>) nanowires.

The nanowires of both materials were fabricated using the electrospinning technique. Firstly, the effect of working parameters on the electrospinning of Nb<sub>18</sub>W<sub>16</sub>O<sub>93</sub> and MoNb<sub>12</sub>O<sub>33</sub> nanofibers

were studied and optimized using central composite design (CCD) based on the response surface methodology (RSM). Experiments were designed to assess the effects of five variables including the applied voltage (V), spinning distance (D), polymer concentration (P), flow rate (F), and addition of NaCl (N) on the resulting diameter of the nanofibers. Prediction models obtained using these variables and verified through analysis of variance (ANOVA) showed that all variables, except flow rate, significantly influenced the nanofibers diameter. These models were used in subsequent experiments to set experimental variables for fabricating  $\text{Nb}_{18}\text{W}_{16}\text{O}_{93}$  and  $\text{MoNb}_{12}\text{O}_{33}$  nanofibers with reduced diameter.

To enhance the electrochemical activities of  $\text{Nb}_{18}\text{W}_{16}\text{O}_{93}$ , pristine and nickel-doped (Ni = 1 wt.%, 3 wt.%, 5 wt.%)  $\text{Nb}_{18}\text{W}_{16}\text{O}_{93}$  nanowires were fabricated using the electrospinning technique, followed by annealing. The effect of nickel doping content on the morphology, structure, and electrochemical performance of  $\text{Nb}_{18}\text{W}_{16}\text{O}_{93}$  nanowires was investigated. The findings from the electrochemical experiments reveal that the 3 wt.% nickel-doped nanowires display an impressive capacity retention of 93.1% over 500 cycles at a high current rate of 5 C. Moreover, Ni doping considerably boosted the electronic conductivity in  $\text{Nb}_{18}\text{W}_{16}\text{O}_{93}$  comparison to the pristine nanowires. The CV test results also demonstrate that Ni doping reduces polarization and enhances the lithium-ion diffusion coefficient.

Furthermore, the possibility of enhancing the electronic conductivity, lithium-ion mobility, and electrochemical kinetics of  $\text{MoNb}_{12}\text{O}_{33}$  was also explored by fabricating NMO and NMO@H-Ar nanowires (@H-Ar denotes heat treatment under Hydrogen and Argon mixture). The hydrogenation treatment resulted in outstanding electrochemical kinetics, including high reversible specific capacity, high initial coulombic efficiency, excellent long-term cycling stability, and good rate performance. This study concludes that Ni doping and hydrogenation

treatment considerably improved the electrochemical activities of  $\text{Nb}_{18}\text{W}_{16}\text{O}_{93}$  and  $\text{MoNb}_{12}\text{O}_{33}$  nanofibers, which is beneficial for developing new anode materials for LIBs.

## **Acknowledgments**

I would like to start by extending my deepest appreciation to my supervisors, Professor Mamoun Medraj and Professor Martin Pugh, for their invaluable guidance, unwavering patience, limitless support, and constant encouragement throughout my doctoral journey at Concordia University. I am grateful for your constructive suggestions and critiques that have played a vital role in the completion of this thesis.

My sincere appreciation to Dr. Dmytro Kevorkov for his invaluable contributions during my doctoral program. In addition, I am sincerely appreciative of Mazen Samara for his excellent administrative support in the TMG lab. To my wonderful TMG members, Dr. Abdullahi Gujba, Dr. Mohamed Elhadi, Dr. Rajwinder Singh, Mostafa Elyoussef, Johnny, Khaled, Carlos, Hosna, Manpreet, and Khaled, thank you for your support.

My profound gratitude also goes to my lovely wife Motunrayo Rachael, and my sons Fatile Rehoboth and Raymond, thanks for your understanding and support toward the success of this program. I also wish to say a big thank you to my parent late Mr. Emmanuel Fatile and Mrs. Bolajoko Fatile, I really appreciate all your support in every aspect. I am also indebted to my Brother and sister in the person of Fatile Ayobami and Fatile Olajumoke.

I gratefully acknowledge the financial support provided by Concordia University, Canada through the Concordia University International Tuition Award of Excellence, Faculty research support, and supervisor's research grant.

Finally, to my late father Mr. Fatile Emmanuel Bamidele, it is quite painful that you are not alive to witness the success of your son, but I know your soul will also rejoice with me. You are so dear to me, and I really miss you. May your gentle soul rest in peace.

## Table of Contents

List of Figures .....	xi
List of Tables .....	xv
List of Abbreviations.....	xvii
Chapter 1: Introduction.....	1
1.1 Background.....	1
1.2. Problem statement .....	2
1.3 Thesis structure .....	4
Chapter 2: Literature Review and Research Motivations .....	6
2.1. Component of lithium-ion batteries .....	6
2.1.1 Separator .....	6
2.1.2 Electrolyte.....	6
2.1.3 Cathode .....	7
2.1.4 Anode .....	8
2.2 Reaction mechanisms in lithium-ion battery anodes .....	8
2.2.1 Intercalation-based anode materials.....	8
2.2.2 Alloying reaction-based anode materials .....	9
2.2.3 Conversion reaction-based anode materials.....	9
2.3 Niobium-based compounds .....	12
2.4 Methods of improving the electrochemical performance of anode materials.....	15
2.4.1 hybridization.....	15
2.4.2 Hierarchical structures .....	16
2.4.3 Doping.....	18
2.4.4 Controlled annealing .....	18
2.4.5 Nanostructuring .....	19
2.5 Ceramic nanowires .....	21

2.6 Methods of fabricating ceramic nanowires .....	22
2.6.1 Template-assisted synthesis method .....	22
2.6.2 Vapor-liquid-solid method .....	23
2.6.3 Solution–liquid-solid method.....	25
2.6.4 Solvothermal method .....	26
2.6.5 Hydrothermal method .....	27
2.6.6 Chemical vapor deposition methods .....	28
2.6.7 Electrospinning technique .....	29
2.6.7.1 Principle of electrospinning technique and basic set-up .....	30
2.6.7.2 Electrospinning of ceramic nanofibers .....	30
2.6.7.3 Influence of working parameters on electrospinning of ceramic nanofibers .....	32
2.7 Objectives .....	33
Chapter 3: Optimization of the Electrospun Niobium–Tungsten Oxide Nanofibers Diameter Using Response Surface Methodology .....	
3.1. Introduction .....	35
3.2. Materials and methods .....	39
3.2.1 Design of experiment.....	39
3.2.3 Electrospinning of nanofibers .....	43
3.2.4. Measurement of the nanofibers diameter .....	44
3.2.5. Development of the CCD response surface model .....	46
3.3. Results and Discussions.....	46
3.3.1 Estimation of coefficients in the mathematical model equation .....	46
3.3.2. Verification of the response surface model.....	48
3.3.3. Visualization of the interactions between the model parameters .....	50
3.3.4. Optimization and validation of the response surface model.....	55
3.4. Conclusion.....	56
Overview of chapter 3 .....	58

Chapter 4: Nickel-doped Nb <sub>18</sub> W <sub>16</sub> O <sub>93</sub> nanowires with improved electrochemical properties for lithium-ion battery anodes.....	59
4.1 Introduction .....	60
4.2 Materials and Methods.....	64
4.2.1. Materials preparation .....	64
4.2.2. Material characterization.....	65
4.2.3. Electrochemical test .....	65
4.3. Results and discussion .....	66
4.3. Conclusion.....	79
4.4. Supporting Information.....	81
4.5. Overview of chapter 4.....	91
Chapter 5: Enhancing niobium-based oxides for high-performance lithium-ion batteries through hydrogenation .....	92
5.2 Experimental .....	97
5.2.1 Fabrication of MoNb <sub>12</sub> O <sub>33</sub> nanowires .....	97
5.2.2. Material characterization.....	98
5.2.3 Electrochemical test .....	99
5.3. Results and discussion .....	100
5.4. Conclusion.....	112
5.5. Supporting Information.....	113
Chapter 6: Conclusions, Contributions, and Recommendations.....	119
6.1. Conclusions .....	119
6.2 Contributions.....	121
6.3 Recommendations.....	124

Appendix .....	160
Appendix A .....	160

## List of Figures

Figure 1-1: Comparison of the volumetric ( $\text{Wh L}^{-1}$ ) and gravimetric ( $\text{Wh kg}^{-1}$ ) energy densities of battery systems .....	2
Figure 1-2: schematic diagram of lithium-ion battery.....	3
Figure 2-1: Lithium storage mechanism of $\text{N}_{18}\text{W}_{16}\text{O}_{93}$ .....	14
Figure 2-2: Methods of improving the electrochemical performance of anode materials.....	17
Figure 3-1: Schematic diagram of the electrospinning process .....	43
Figure 3-2: SEM micrographs and nanofibers diameter distribution corresponding to the experimental run numbers in Table 3, as follows: (a,b) 3, (c,d) 13, (e,f) 14, (g,h) 18, (i,j) 29, and (k,l) 36. ....	44
Figure 3-3: Validation of the nanofibres diameter model using (a) observed experimental data versus predicted values (b) internally studentized residuals versus predicted value.....	49
Figure 3-4: 3D response surface plots (a,c,e,g,i) and 2D contour plots (b,d,f,h,j) of interaction between the (a,b) applied voltage and spinning distance (VD); (c,d) spinning distance and polymer concentration (DP); (e,f) flow rate and polymer concentration (PF); (g,h) spinning distance and concentration of NaCl (DN); and (i,j) polymer concentration and concentration of NaCl (PN) .....	54
Figure 3-5: Model predicted nanofibers diameter in relation to the current experimental results .....	56
Figure 4-1: Schematic illustration of the fabrication process .....	66

Figure 4-2: XRD patterns of (a) undoped and nickel-doped Nb<sub>18</sub>W<sub>16</sub>O<sub>93</sub>, and (b) enlarged (160), (290), and (001) peaks ..... 67

Figure 4-3: SEM images of as-spun (a) NWO, (b) NWO-Ni-1, (c) NWO-Ni-3, (d) NWO-Ni-3, (e) STEM image of NWO-Ni-5, (f-j) corresponding EDS elemental mapping images of Nb, W, O, Ni elements in NWO-Ni-5, and (k) STEM image of NWO ..... 69

Figure 4-4: XPS survey scan of (a) NWO and, (b) NWO-Ni-5, XPS spectra of (c) Nb 3*d*, (d) W 4*f*; (e) Ni 2*p*, and (f) O 1*s*..... 71

Figure 4-5: (a) comparison of cell polarization with previous works, charge/discharge profile at 0.2 C for (b) NWO, (c) NWO-Ni-1 (d) NWO-Ni-3, (e) NWO-Ni-5, (f) capacity retention at 5 C..... 72

Figure 4-6: (a) Long-term cycling performance at 5 C, (b) rate capabilities of NWO, NWO-Ni-1, NWO-Ni-3, and NWO-Ni-5..... 75

Figure 4-7: (a,b) CV curves of NWO and NWO-Ni-3 at different scan rates, (c,d) relationships between peak current and the square root of the scan rate of NWO and NWO-Ni-3.....76

Figure 4-8: (a) Nyquist plots of NWO, NWO-Ni-1, NWO-Ni-3, and NWO-Ni-5; (b) the corresponding relationship between *Z'* and  $\omega^{-1/2}$  in the low-frequency region..... 79

Figure S4-1: Punched electrode disks..... 82

Figure S4-2: (a) XRD patterns of NWO-Ni-5, (b) Calculated XRD pattern of NOW..... 82

Figure S4-3: SEM images of (a) NWO, (b) NWO-Ni-5, STEM images of (c,d) NWO after annealing, EDS profile of (e) NWO, (f) NWO-Ni-1, (f) NWO-Ni-3, and (h) NWO-Ni-5..... 83

Figure S4-4: XPS spectra of NWO, NWO-Ni-1, NWO-Ni-3, and NWO-Ni-5 (a) W 4*f*; and (b) Nb 3*d* ..... 84

Figure 4-5: CV curve of (a) NWO, (b) NWO-Ni-1, (c) NWO-Ni-3, (d) NWO-Ni-5.....	85
Figure S4-6: CV curve of NWO, NWO-Ni-1, NWO-Ni-3, and NWO-Ni-5.....	86
Figure S4-7: Comparison of initial specific capacity of NWO-Ni-3 with previous works.....	86
Figure S4-8: Coulombic efficiency of NWO, NWO-Ni-1, NWO-Ni-3, and NWO-Ni-5 at 5 C... .....	87
Figure S4-9: (a,b) CV curves of NWO-Ni-3 and NWO-Ni-5 at different scan rates, (c,d) relationships between peak current and the square root of the scan rate of NWO-Ni-3 and NWO- Ni-5.....	89
Figure 5-1: Schematic illustration of the fabrication process.....	100
Figure 5-2: SEM images of (a) as-spun nanofibers; (b) NMO (c) NMO@H-Ar; (d-g) corresponding EDS elemental mapping images of Mo, O, and Nb elements in NMO; and (h) STEM image of NMO .....	101
Figure 5-3: (a) XRD pattern of NMO and NMO@H-Ar ; (b) XPS survey spectra of NMO and NMO@H-Ar; XPS spectra of (c) Nb 3d; (d) Mo 3d; (e) O 1s; (f) EPR spectra of NMO and NMO@H-Ar .....	102
Figure 5-4: (a) UV–Vis absorption data and (b) band gap energy of NMO and NMO@H-Ar .....	105
Figure 5-5: CV curve of (a) NMO; (b) NMO@H-Ar; charge/discharge profile for (c) NMO; and (d) NMO@H-Ar.....	106

Figure 5-6: (a) Long-term cycling performance of NMO and NMO@H-Ar at 10 C; (b) rate capabilities of NMO and NMO@H-Ar..... 108

Figure 5-7: (a,b) CV curves of NMO and NMO@H-Ar at different scan rates; (c) Nyquist plots of NMO@H-Ar and NMO; (d) relationship between impedance and low-frequency region... 110

Figure S5-1: CV curve of NMO and NMO@H-Ar..... 114

Figure S5-2: Average operating potential of Niobium-based anode materials ..... 114

Figure S5-3: Capacity retention rate of NMO and NMO@H-Ar..... 116

Figure S5-4: Relationships between peak current and the square root of the scan rate of (a) NMO and (b) NMO@H-Ar..... 118

## List of Tables

Table 2-1: Reversible specific capacity of anode materials based on their reaction mechanisms .. .....	10
Table 2-2: Advantages and disadvantages of anode materials based on their reaction mechanisms.....	11
Table 3-1: Summary of the preliminary investigation results .....	40
Table 3-2: The factors and associated levels for experimental design .....	41
Table 3-3: Experimental design and results .....	42
Table 3-4: Table 4: Estimation of the model coefficient and corresponding p-values .....	47
Table S4-1: Unit cell parameters of pristine and nickel-doped Nb <sub>18</sub> W <sub>16</sub> O <sub>93</sub> .....	83
Table S4-2: Comparisons of cycling performance of NWO-Ni-3 with other niobate anode materials.....	88
Table S4-3: The diffusion coefficients of Li <sup>+</sup> obtained from the CV curves.....	89
Table S4-4: Comparisons of Li <sup>+</sup> diffusion coefficients in this work with other niobate-based anode materials.....	90
Table S4-5: Lithium-ion diffusion coefficients obtained from the EIS.....	90
Table S5-1: Comparisons of reversible specific capacity of NMO and NMO@H-Ar with other niobate anode materials.....	115
Table S5-2: Comparisons of cycling performance of NMO and NMO@H-Ar with other niobate anode materials.....	117

Table S5-3: The Lithium-ion diffusion coefficients obtained from the CV curves..... 118

Table S5-4: Fitting parameters and diffusion coefficients obtained from EIS..... 118

## List of Abbreviations

<b>AMA</b>	Average Model Accuracy
<b>ANOVA</b>	Analysis of Variance
<b>CCD</b>	Central Composite Design
<b>CV</b>	Cyclic Voltammetry
<b>CVD</b>	Chemical Vapor Deposition
<b>D<sub>Li</sub></b>	Lithium-ion Diffusion Coefficient
<b>EDX</b>	Energy Dispersive X-ray Spectrometer
<b>EIS</b>	Electrochemical Impedance
<b>EPR</b>	Electron Paramagnetic Resonance
<b>GCD</b>	Galvanostatic Charge and Discharge
<b>LIBs</b>	Lithium Ion Batteries
<b>R<sub>CT</sub></b>	Charge transfer Resistance
<b>RSM</b>	Response Surface Methodology
<b>SEI</b>	Solid Electrolyte Interface
<b>SEM</b>	Scanning Electron Microscopy
<b>SLS</b>	Solid Liquid Solid
<b>STEM</b>	Scanning Transmission Electron Microscope
<b>STEOV</b>	Single Electron Trapped Oxygen Vacancy
<b>VLS</b>	Vapour Liquid Solid
<b>XPS</b>	X-ray Photoelectron Spectroscopy
<b>XRD</b>	X-ray Diffraction

# Chapter 1: Introduction

## 1.1 Background

Over the last few decades, there has been a steady increase in energy demand around the world which largely depends on fossil fuels such as natural gas, coal, and gasoline. The emission of carbon dioxide and other global warming gases associated with the continuous combustion of fossil fuels is a significant environmental concern currently being addressed globally [1]. Thus, it is imperative to seek alternative and sustainable energy sources to reduce the dependence on fossil fuels. Many renewable energy sources have been studied, including solar, hydroelectric, wind, and biomass [2]. Most of these renewable energy sources generate power intermittently due to their weather dependency. Besides, peak energy consumption and peak generation time may not coincide. Hence, high-performance energy storage systems are essential for the optimal utilization of renewable energy sources.

Energy storage devices such as lithium-ion batteries (LIBs) and supercapacitors have been studied [3]. However, LIBs have been regarded as the most promising energy storage device owing to their high efficiency, energy, and power density [3]. These unique attributes make LIBs the dominant choice for powering portable electronic devices, laptops, and electric vehicles [4]. Over the last few decades, several battery systems have been developed, including nickel-cadmium (Ni-Cd), nickel metal hydride (Ni-MH), lithium-ion, and lead-acid, as shown in Figure 1-1 [5]. The cell potential (V) and capacity ( $A \cdot h \cdot kg^{-1}$ ) of a battery, both of which are directly related to the chemistry of the system, determine how much electrical energy it can store per unit of weight ( $W \cdot h \cdot kg^{-1}$ ) or per unit of volume ( $W \cdot h \cdot l^{-1}$ ). Among all existing battery systems, lithium-based batteries outperform others due to their design flexibility and high energy density, as shown in Figure 1-1 [5]. These reasons justify why LIBs are preferred over other

battery systems in critical and more advanced applications. Nonetheless, it is desirable to develop high-performance and fast-charging LIBs with high power density and reversible capacities to meet future energy storage needs.

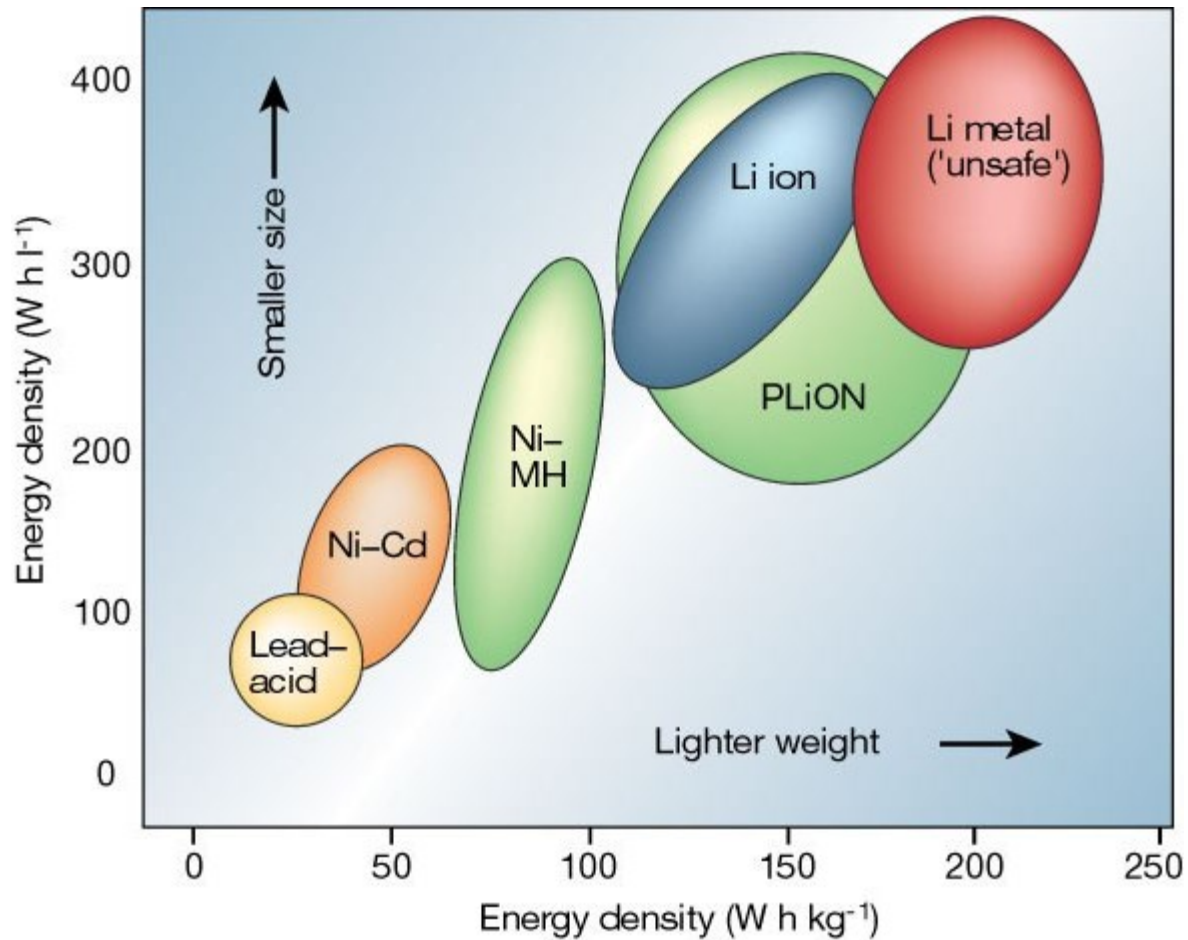


Figure 1-1: Comparison of the volumetric (Wh L<sup>-1</sup>) and gravimetric (Wh kg<sup>-1</sup>) energy densities of battery systems [5].

## 1.2. Problem statement

A conventional Li-ion battery is typically composed of three major parts: electrodes (anode and cathode), electrolytes, and separators, as shown in Figure 1-2. The electrolyte serves as the charge carrier in a lithium-ion battery cell. The two electrodes (the cathode and the anode) are constructed from materials that can host lithium ions at varying potentials. During the

charging process, electrical energy is transformed into chemical energy stored in LIBs. This is accomplished when lithium ions move from the cathode and pass through the electrolyte to the anode. On the other hand, the discharge process occurs when the chemical energy stored in a LIB is converted into electrical energy. At this time, the lithium ions migrate in the opposite direction.

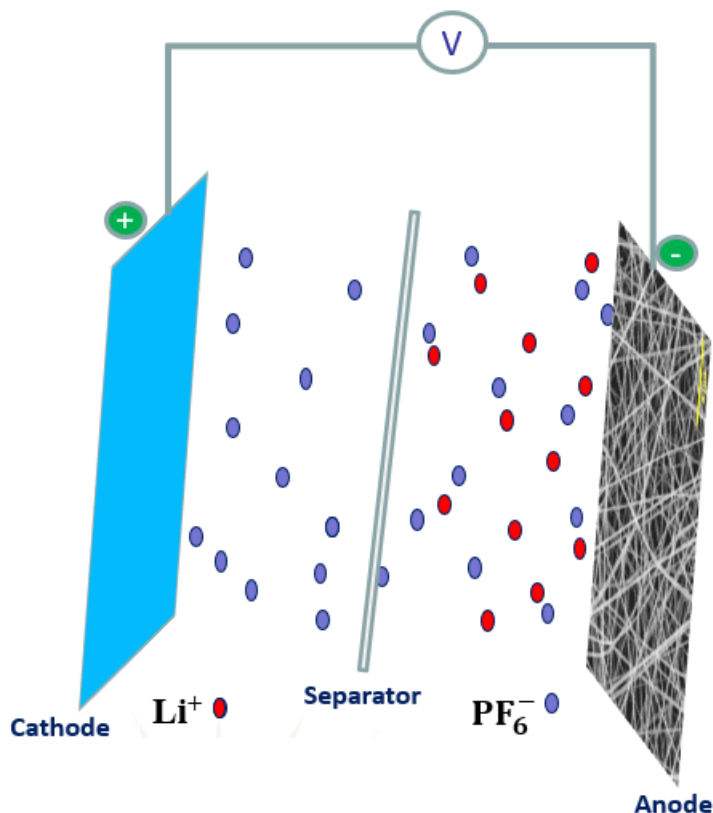


Figure 1-2: schematic diagram of lithium-ion battery.

Currently, most commercial lithium-ion batteries are made of graphite as the anode, lithiated metal oxide as the cathode, and 1M  $\text{LiPF}_6$  in an organic carbonate solvent as the electrolyte [6]. It is vital to select the right combination of components to fabricate LIBs with desired electrochemical properties. Graphite is extensively used as an anode in commercial LIBs owing to its low de-lithiation potential, low processing cost, and high theoretical/practical specific capacity (theoretical capacity of  $372 \text{ mAh g}^{-1}$ ) compared to other potential anode

materials [7,8]. However, a few drawbacks have been identified with the use of graphite as anode material for LIBs, including (i) the formation of lithium dendrites at its low working voltage ( $< 0.2$  V), which is a significant safety concern; (ii) poor cycling stability resulting from its volume change ( $\sim 9\%$ ) during Intercalation reactions; and (iii) low rate capability arising from its poor  $\text{Li}^+$  mobility [8], [9]. With the increasing demand for safe LIBs with high reversible capacity, excellent rate capability, and high cycling stability, it is imperative to develop an alternative anode material to replace graphite.

Over the last few years, various Nb-M-O compounds have been explored as potential anodes for LIBs, including  $\text{Nb}_{18}\text{W}_{16}\text{O}_{93}$  [3], [10],  $\text{TiNb}_6\text{O}_{17}$  [11],  $\text{FeNb}_{11}\text{O}_{29}$  [12], [13] and  $\text{BaNb}_{3.6}\text{O}_{10}$ [14]. These materials have been reported to demonstrate high theoretical capacity, significant structural stability, safe operating voltage, high power density, and environmental friendliness [15]–[17]. However, their intrinsic low electronic conductivity and poor electron transfer properties are significant drawbacks that still need to be addressed [15], [16]. Furthermore, it is vital to improve their electrochemical performance to fulfill modern energy applications' requirements. Thus, there is a need to identify the best methods/techniques that can be employed to improve their electronic conductivity and overall electrochemical performance.

### **1.3 Thesis structure**

The thesis is divided into six chapters based on the methodology used in this study. It should be noted that the thesis is based on a manuscript and includes three journal articles. Chapter 1 presents a concise overview of the entire thesis, focusing on the components and working principle of LIBs, the background and limitations of graphite as the current anode material in commercial LIBs, and the emergence of Nb-M-O compounds as potential anode materials for LIBs. Chapter 2 is an overview of the literature on research activities, starting from

the working and reaction mechanism of anode material for LIBs, Nb-M-O compounds, and methods of improving the performance of anode materials. The chapter also outlines the rationale for selecting electrospinning as the method for fabricating the nanowires in this work and other methods of fabricating nanowires. Furthermore, a brief history of electrospinning and the factors influencing electrospinning process parameters are reviewed. The research motivations and objectives are also discussed in relation to the literature findings and current work. Chapter 3 presents the first article on optimizing the electrospinning process of niobium-tungsten oxide nanofibers. Chapter 4 presents the second article focusing on nickel-doped  $\text{Nb}_{18}\text{W}_{16}\text{O}_{93}$  nanowires with improved electrochemical properties for lithium-ion battery anodes. An article that studies the electrochemical performance of oxygen-vacant  $\text{MoNb}_{12}\text{O}_{13}$  nanowires for lithium-ion battery anode is presented in chapter 5. The last chapter outlines the contents and contributions of the current work and recommendations for future research. Appendices are also provided for further information about the research work carried out.

## **Chapter 2: Literature Review and Research Motivations**

### **2.1. Component of lithium-ion batteries**

All battery system consists of three major components: the electrodes (anode and cathode), an aqueous/non-aqueous electrolyte, and a separator. The separator, which is an electrolyte-permeable membrane, physically separates the anode and cathode [18]. The following section discusses the components of LIBs.

#### **2.1.1 Separator**

The separator is an essential component of LIBs and impacts their overall performance. The separator separates the anode and cathode while allowing ions to pass freely, isolating electron flow, and preventing internal short circuits in the battery. The most commonly used materials in commercial batteries include microporous polymer films, such as high-density polyethylene (HDPE), polyethylene (PE), and polypropylene (PP) [19]. These separators have low porosity and poor liquid electrolyte wettability, which reduces heat shrinkage at high temperatures. A separator with high thermal stability is generally required to improve battery safety [18], [19]. Other properties of a good separator include high mechanical strength, high wettability, and uniform thickness [19]. Celgard polypropylene films was employed as a separator in this research owing to its high voltage stability and mechanical strength [19].

#### **2.1.2 Electrolyte**

The electrolyte is one of the most important components influencing the safety, performance, and capacity of LIBs, and it is also the most flammable component of batteries. A typical electrolyte must possess good physical and chemical properties such as rapid lithium ion transmission, chemical inertness, and electrode interface compatibility [20], [21]. The most widely used commercial organic electrolytes are lithium hexafluorophosphate ( $\text{LiPF}_6$ ), ethylene

carbonate (EC), dimethyl carbonate (DMC), and propylene carbonate (PC) [21]. The safety of the electrolyte can be improved by using additives such as cathodic protection agents,  $\text{LiPF}_6$  salt stabilizers, and safety protection agents [20]. A mixture of  $1 \text{ mol L}^{-1}$   $\text{LiPF}_6$  in ethylene carbonate and dimethyl carbonate solvent was employed as an electrolyte in this work due to its chemical stability and high ionic conductivity [20-21].

### 2.1.3 Cathode

In LIBs chemistry, the cathode material is the primary and active source of all Li-ions [22]. Cathode materials are typically transition metal oxides that can be oxidized to higher valences when lithium is removed [23], [24]. While oxidation of the transition metal can keep the compound charge neutral, large compositional changes frequently result in phase changes, so stable crystal structures over a wide range of compositions must be used as a cathode [23]. The most widely used cathode materials for LIBs include  $\text{LiCoO}_2$ ,  $\text{LiFePO}_4$ , Li-Mn-O, and lithium-layered metal oxides [22], [23]. In LIBs, the positive terminal must act as a source of lithium because the negative carbon electrode lacks lithium; thus, an intercalation compound is required for the cathode [24]. Since lithium-ion exchange with the electrolyte only takes place at the electrode-electrolyte interface, the cathode performance is directly influenced by the electrode microstructure and morphology as well as the cathode material's inherent electrochemical properties [18]. Energy can be stored in cathode materials through two distinct mechanisms: (1) intercalation and (2) conversion reaction [18]. Recently, lithium disks have been extensively used as cathodes for LIBs, owing to its remarkable electrochemical performance including high energy density, longer cycle life, and enhanced stability [18]. Hence, a lithium disk was utilized as cathode in this research.

#### **2.1.4 Anode**

The performance of LIBs also largely depends on their anode materials. Thus, an ideal anode material for LIBs must satisfy specific requirements, including low potential against cathode materials, long cycle life, high rate capability, low cost, and environmental friendliness [25]. Anodes can be classified into three main groups based on their reaction mechanisms: intercalation-based, conversion-reaction-based, and alloying-reaction-based materials [18]. The following section discusses these reaction mechanisms in detail.

### **2.2 Reaction mechanisms in lithium-ion battery anodes**

#### **2.2.1 Intercalation-based anode materials**

Intercalation materials have been considered potential anode materials for LIBs due to their promising physical and chemical properties. In intercalation-based materials, lithium ions are electrochemically intercalated into the space between material layers during the charging and discharging processes [25]. Typical examples of intercalation anode materials include graphite, Ti, Nb, and V based oxides [18], [25]. Metal-based oxides such as  $\text{Nb}_{18}\text{W}_{16}\text{O}_{93}$  and  $\text{TiO}_2$  have the potential to be safer alternatives to graphite anodes because they operate at a potential above 0.8 V compared to the graphite  $\text{Li}^+/\text{Li}$  intercalation/de-intercalation potential where the formation of a solid electrolyte interface (SEI) layer on the anode surface can be prevented [25]. Furthermore, metal-based oxides have demonstrated other superior properties, including low volume change during discharge/charge, high power density, and excellent cycling stability compared to graphite [25]. However, one of the limitations of this type of material is low electronic conductivity [25]. This problem of low electronic conductivity of Intercalation anode materials has been addressed in this work.

### 2.2.2 Alloying reaction-based anode materials

This group includes metals that can be alloyed with lithium, including silicon (Si), germanium (Ge), zinc (Zn), and tin (Sn), as well as their alloys [21]. The reaction mechanism of alloying-based anode materials is represented as:



Where M is the alloying metal. Typically, the lithium-ion storage capacity of these materials can be several times greater than that of graphite. For instance, the theoretical capacities of Si, Ge, and Al in their respective lithium compound is  $4200 \text{ mA h g}^{-1}$  (about 11.29 times that of graphite),  $1600 \text{ mAh g}^{-1}$  (about 4.3 times that of graphite), and  $993 \text{ mAh g}^{-1}$  (about 2.67 times that of graphite), respectively [26]. In addition, they have good cycling performance, which makes them excellent LIB anode materials [25]. However, these alloying anode materials undergo extremely high volume expansion (about 400% for Si and 370% for Ge) during alloying/dealloying process owing to their inherent structural limitations, resulting in electrochemical performance degradation, capacity fading, and loss of electrical contact [27].

### 2.2.3 Conversion reaction-based anode materials

Li storage in this material is accomplished through conversion reactions based on the faradaic reaction [18] shown in (eq. 2-2).



where M = transition metal (such as Cu, V, Mn, Co, W, Mo, and Fe), and B = anion (such as O, S, and P). A simple combination of candidates for M and B can produce a variety of anode materials in this group. Conversion-based anode materials offer high specific capacities of 700–

1200 mAh g<sup>-1</sup>, which is comparable to most alloying materials but much higher than intercalation materials [27].

Table 2-1: Reversible specific capacity of anode materials based on their reaction mechanisms

<b>Intercalation Type</b>	<b>Anode Material</b>	<b>Initial Specific Capacity (mA h g<sup>-1</sup>)</b>	<b>Ref</b>
Conversion	Nanoparticulate Mn <sub>3</sub> O <sub>4</sub> /VGCF	950 mA h g <sup>-1</sup> at 0.2 A g <sup>-1</sup>	[28]
Conversion	Mesoporous hollow CO <sub>3</sub> O <sub>4</sub>	1536.8 mA h g <sup>-1</sup> at 100 mA g <sup>-1</sup>	[29]
Conversion	CuO Nanohexagon	1007 mA h g <sup>-1</sup> at 215 mA g <sup>-1</sup>	[30]
Conversion	Porous Mn <sub>3</sub> O <sub>4</sub>	1412.2 mA h g <sup>-1</sup> at 0.1 C	[31]
Conversion	MoO <sub>3</sub> /G	1400 mA h g <sup>-1</sup> at 100 mA g <sup>-1</sup>	[32]
Alloying	Sb <sub>2</sub> Se <sub>3</sub> @CNF-500	1087.3 mA h g <sup>-1</sup> at 100 mA g <sup>-1</sup>	[33]
Alloying	Si/C graphite	750 mA h g <sup>-1</sup> at 0.6 C	[34]
Alloying	Octahedral Sb <sub>2</sub> O <sub>3</sub>	1031.3 mA h g <sup>-1</sup> at 200 mA g <sup>-1</sup>	[35]
Alloying	Si/SiO <sub>2</sub>	1772 mA h g <sup>-1</sup> at 1.8 A g <sup>-1</sup>	[36]
Alloying	Ultrafine SnO <sub>2</sub>	1196.6 mA h g <sup>-1</sup> at 100 mA g <sup>-1</sup>	[37]
Alloying	Cu/Si nanoflowers	1869 mA h g <sup>-1</sup> at 1.6 A g <sup>-1</sup>	[38]
Alloying	Spherical tremella-like Sb <sub>2</sub> O <sub>3</sub>	724 mA h g <sup>-1</sup> at 100 mA g <sup>-1</sup>	[39]
Intercalation	Al <sub>0.5</sub> Nb <sub>24.5</sub> O <sub>62</sub> -P	300 mA h g <sup>-1</sup> at 0.5 C	[17]
Intercalation	TiO <sub>2</sub> Nanowires	650 mA h g <sup>-1</sup> at 35 mA g <sup>-1</sup>	[39]
Intercalation	Mg <sub>2</sub> Nb <sub>34</sub> O <sub>87</sub> -P	338 mA h g <sup>-1</sup> at 0.1 C	[16]
Intercalation	NMO@S	312 mA h g <sup>-1</sup> at 0.5 C	[40]
Intercalation	Al <sub>0.5</sub> Nb <sub>24.5</sub> O <sub>62</sub> -M	321 mA h g <sup>-1</sup> at 0.5 C	[17]
Intercalation	H-TNO-1h	305.2 at 0.1 mA g <sup>-1</sup>	[41]

Conversion-type anodes, like alloying anodes, suffer from material pulverization at the individual particle level, an unstable SEI layer, and volume change at the whole electrode level [27]. In addition, the large voltage hysteresis (the difference between charge and discharge voltage) of the conversion type anodes, which reflects the slow charge/discharge pathways, is another drawback in this type of anode material [18]. The reversible specific capacity, merits, and demerits of various types of anode materials are summarized in Tables 2-1 and 2-2, respectively.

Table 2-2: Advantages and disadvantages of anode materials based on their reaction mechanisms

<b>Type</b>	<b>Advantages</b>	<b>Disadvantages</b>
Intercalation type	Safe working potential	Low theoretical/practical capacity
Metal oxide based	High structural stability	Poor electronic conductivity
	Low cost	
	Environmentally friendly	
Alloying type	High theoretical capacity	Large irreversible capacity loss
	Good safety	Extremely large volume expansion
	High energy density	Huge capacity fading
Conversion type	High specific capacity	Low coulombic efficiency
	Low-cost unstable SEI	Poor cycling
	Environmentally friendly	Large voltage hysteresis

### 2.3 Niobium-based compounds

Niobium-based compounds (M-Nb-O, where M = W, Zr, Li, Ti, P, Mo) are currently gaining attention as emerging anode materials. These compounds can exist in several polymorphs, including tetragonal, orthorhombic, monoclinic, and pseudohexagonal, each of which can be obtained through controlled thermal treatment of the material [42]. The charge and size of the metal ion that occupies the tunnel sites usually influence the properties of the resulting compound [43]. For this reason, many niobium-based compounds have been investigated for various applications, including energy storage [30], gas sensors [44], photocatalysts [45], and electrochromic [46].

Niobium-tungsten oxide is among the most important members of niobium-based compounds. These compounds had been reported to exhibit two crystal structures; the Wadsley Roth phase (WRP) with block-type structures and tetragonal tungsten bronze type structure (TTB) [47]. The TTB structure possesses regular or distorted corner-sharing  $\text{MO}_6$  octahedra at various M-O-M angles to form tunnels of different shapes and sizes [43]. Unlike the TTB structure, the WRP consists of blocks of corner-sharing octahedral which are connected by edge-sharing along the crystallographic shear planes [47]. The block size usually depends on the oxygen-to-metal ratio of the compound; a higher oxygen-to-metal ratio promotes the formation of larger blocks in the structure due to an increase in corner-sharing connections between octahedral [48]. These unique attributes of the two structures formed by niobium-tungsten oxide made them suitable as potential materials for storing lithium ions. This has prompted various researchers to investigate the niobium-tungsten compound as a potential material for storing lithium ions.

The lithium-ion storage mechanism of  $W_3Nb_{14}O_{44}$  was studied by Yan *et al.* [49]. The authors explained that three possible types of cavities could accommodate lithium ions in the compound; the cavities are denoted as type I, II, and III. Type I contains five side tunnels, type II contains four side tunnels, and type three contains three side tunnels. The size of each cavity determines the number of lithium atoms that can be accommodated. For instance, type I can accommodate two lithium ions, while type II and III can accommodate one lithium ion each [11]. Ye *et al.* [47] also reported a similar result when they investigated the lithium-ion storage mechanism of  $N_{18}W_{16}O_{93}$  with TTB structure. They reported that  $N_{18}W_{16}O_{93}$  has three different types of 4g location cavities that may hold lithium ions: A five-sided tunnel (type I), a four-sided tunnel (type II), and a three-sided tunnel (type III) as shown in Figure 2-1. The Li ions stored in each cavity largely depend on their sizes. Two Li atoms can be stored in a type I cavity, type II cavity can accommodate one Li atom, and type III cavity can accommodate two Li atoms [47].  $N_{18}W_{16}O_{93}$  could accommodate about 35 Li ions per formula, and the reaction between the insertion and extraction of lithium ions can be represented as follows:



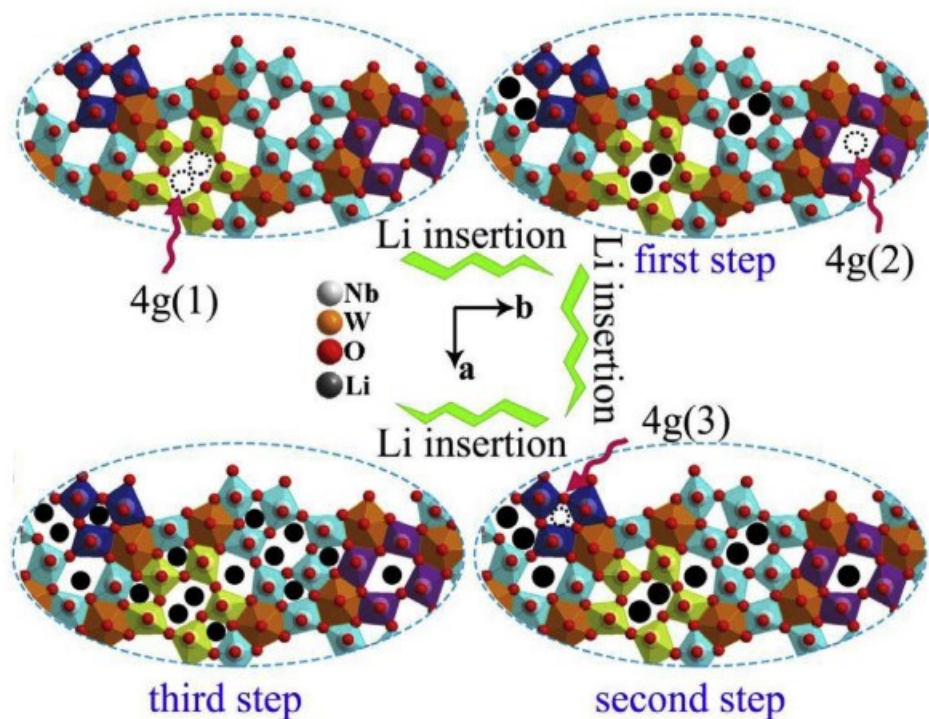


Figure 2-1: Lithium storage mechanism of  $N_{18}W_{16}O_{93}$  [47].

Lately, niobium-molybdenum oxides have been widely explored as potential anode materials for LIBs due to their unique crystal structure and remarkable electrochemical performance. These compounds also exhibit high theoretical capacity due to their multiple redox couples of  $Mo^{6+}/Mo^{5+}$ ,  $Mo^{5+}/Mo^{4+}$ ,  $Nb^{5+}/Nb^{4+}$ , and  $Nb^{4+}/Nb^{3+}$  [40]. Various niobium-molybdenum oxides have been studied, including  $Nb_{26}Mo_4O_{77}$  [50],  $Mo_3Nb_2O_{14}$  [51], and  $MoNb_{12}O_{33}$  [52]. Recently, Ma *et al.* [50] studied the electrochemical performance of  $Nb_{26}Mo_4O_{77}$ . They reported that the compound contains blocks of 3 x 4 corner-shared  $MO_6$  ( $M=Nb, Mo$ ) octahedra and 4 x 4 corner-shared  $MO_6$  octahedra occurring in an alternating sequence. These blocks are further linked by  $MoO_4$  tetrahedra at each corner, which is advantageous for  $Li^+$  intercalation and ensures minimal structural strain during the de-intercalation of  $Li^+$  [50].

Various studies on niobium-tungsten compounds show that they are promising materials for LIBs anode owing to their unique properties, including high theoretical/practical capacities, long-term cyclability, remarkable structural stability, and safe operating potential, which avoids the formation of dendrites. However, the electrochemical performance of these compounds is inhibited by inherent poor electronic conductivity, resulting in poor lithium-ion mobility and charge transfer [53], [54]. Therefore, it is imperative to address all these shortcomings before they can be commercialized. The following section described different methods of addressing the problem.

## **2.4 Methods of improving the electrochemical performance of anode materials**

Several approaches have been used to enhance the conductivity and electrochemical performance of anode materials for LIBs, including hybridization, hierarchical structures, doping, controlled annealing, and nanostructuring [55], [56], as shown in Figure 2-2. These approaches have resulted in the enhancement of certain features of anode materials, such as the improvement of lattice mismatch, surface structure, and the introduction of oxygen vacancies. In addition, a combination of these methods can also be adopted simultaneously to harness the synergetic optimization effect.

### **2.4.1 hybridization**

Hybridization has proven to be one of the most effective methods of overcoming the problem of inherent poor electronic conductivity and improving the electrochemical performance of anode materials for LIBs. This method involves the integration of the potential anode with other materials such as graphene, carbon nanotubes (CNTs), carbon nanofibers (CNFs), noble metals, and other conductive materials to form a hybrid structure [57]. Recently, Zhao *et al.* [58] prepared TiO<sub>2</sub> microsphere hybridized with a biomass-derived hierarchical 3D-carbon

framework (N, P-C@TiO<sub>2</sub>). They found that the charge transfer resistance (R<sub>ct</sub>) of TiO<sub>2</sub> decreased from 233.9 Ω to 111.1 Ω for N, P-C@TiO<sub>2</sub>; this indicates that the hybridization process resulted in improved electronic conductivity. They also reported that N, P-C@TiO<sub>2</sub> anode exhibits high reversible specific capacity with improved rate capability and cycling stability compared to the TiO<sub>2</sub> anode. Wang *et al.* [59] also fabricated Fe<sub>3</sub>O<sub>4</sub>@Ti<sub>3</sub>C<sub>2</sub> MXene hybrid anode through a simple ultrasonication of Ti<sub>3</sub>C<sub>2</sub> MXene and Fe<sub>3</sub>O<sub>4</sub> nanoparticles. The results obtained from the investigation show that the reversible specific and volumetric capacities of Fe<sub>3</sub>O<sub>4</sub>@Ti<sub>3</sub>C<sub>2</sub> were successfully improved through the hybridization process. The results obtained from the recent studies carried out by Xu *et al.* [60] and Zhou *et al.* [61] also confirm the hybridization process improved the electrochemical performance of FeS<sub>2</sub>/CNT and SnS (SnX), respectively.

#### **2.4.2 Hierarchical structures**

Hierarchical structures combine the advantages of materials of varied sizes (nanoscale/microscale), pores (macropore /micropore/mesopore), and phases (perovskite/layered compounds/spinel), which allows them to assemble systematically into a variety of advantageous morphologies [62], [63]. The benefits of employing materials with hierarchical structures as anode for LIBs include: (i) they possess porous structure to accommodate the mechanical strain associated with lithium intercalation and de-intercalation; (ii) the porous structures ensure efficient impregnation of the electrolyte and adequate contact area between the electrode and electrolyte, hence boosting rate performance; and (iii) the nanoscale building blocks guarantee short electronic and Li<sup>+</sup> transport distances, hence enhancing electrochemical activity [55]. In the work of Wang *et al.*, [64] they fabricated a hierarchically structured Li<sub>4</sub>Ti<sub>5</sub>O<sub>12</sub> material with a conductive carbon coating and studied its electrochemical characteristics for LIB applications.

They found that the hierarchically structured  $\text{Li}_4\text{Ti}_5\text{O}_{12}$  anode demonstrated enhanced  $\text{Li}^+$  mobility with improved electronic conductivity. Even at a high current rate of 25 C, the material still delivered a reversible discharge specific capacity of  $144.05 \text{ mA h g}^{-1}$  and capacity retention of 96.3% after 500 cycles. Jia *et al.* [65] also studied the electrochemical performance of hierarchical porous  $\text{CNT@Si@C-Gr}$ . They reported that the material exhibits a remarkable cycling performance with a reversible specific capacity of  $718 \text{ mAh g}^{-1}$  at a current density of  $0.75 \text{ mAcm}^{-2}$ . The improved electrochemical performance reported in the literature has shown the importance of the hierarchically structured strategy for improving the performance of anode material for LIBs.

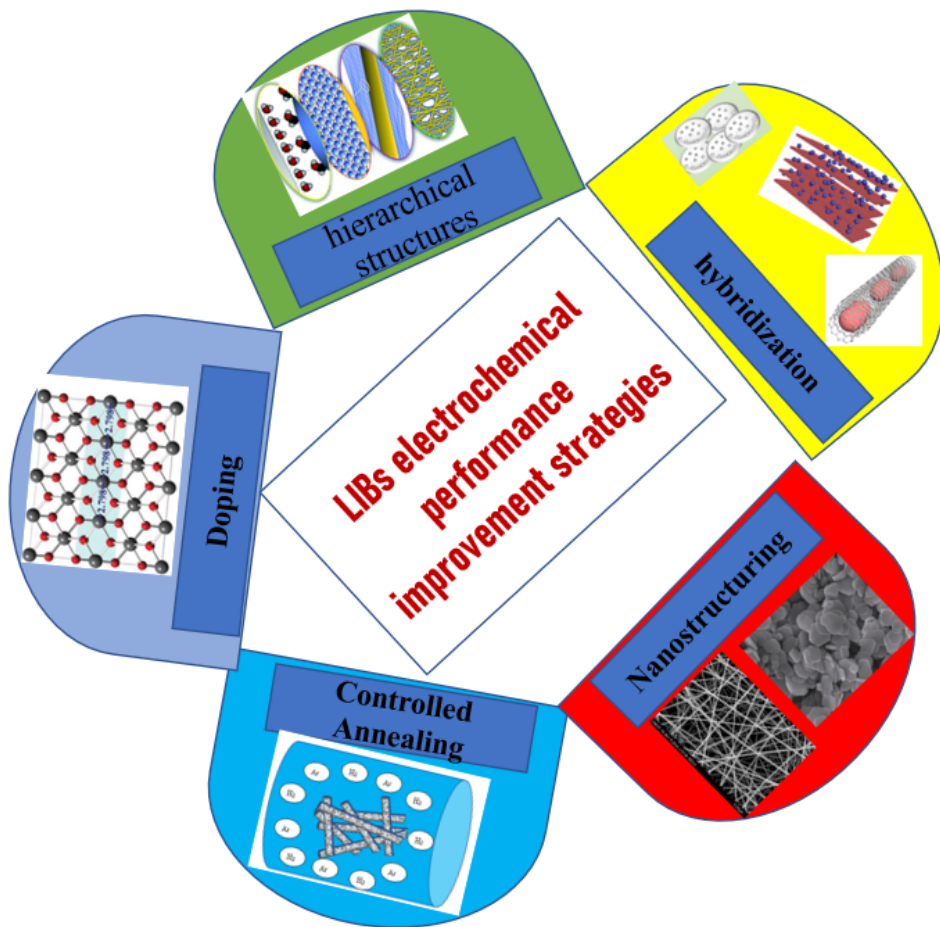


Figure 2-2: Methods of improving the electrochemical performance of anode materials.

### 2.4.3 Doping

Doping can increase the electrochemical performance of LIBs by altering the lattice constants and band gap, hence increasing the  $\text{Li}^+$  diffusion rate and electronic conductivity [57]. Doping can also create an unbalanced charge in a material, thereby resulting in the generation of oxygen vacancies. In addition, doping can induce impurity levels in the bandgap and enhance the inherent electrical conductivity of materials [66]. Hsiao *et al.* [67] studied the electrochemical activities of  $\text{W}^{6+}$  doped  $\text{TiNb}_2\text{O}_7$  (TNO). They reported that the lithium-ion diffusion coefficient of TNO increased from  $9.12 \times 10^{-11} \text{ cm}^2 \text{ s}^{-1}$  to  $2.29 \times 10^{-10} \text{ cm}^2 \text{ s}^{-1}$ . The reversible specific capacity also increased from 242.3 to 259.6  $\text{mAh g}^{-1}$ . The improvement in electrochemical performance of  $\text{W}^{6+}$  doped TNO was attributed to the substitution of  $\text{Ti}^{4+}$  and  $\text{Nb}^{5+}$  ions with  $\text{W}^{6+}$  ions and the release of electrons as a result of charge compensation which resulted in the partial reduction of  $\text{Ti}^{4+}$  and  $\text{Nb}^{5+}$  ions. Huang *et al.* [12] also studied the electrochemical performance of  $\text{Al}^{3+}$  ions doped  $\text{FeNb}_{11}\text{O}_{29}$ . The results of their studies confirmed that  $\text{Al}_{0.2}\text{Fe}_{0.8}\text{Nb}_{11}\text{O}_{29}$  shows improved electrochemical kinetics, with initial-cycle coulombic efficiency of 95.0%, a high reversible specific capacity of 318  $\text{mAh g}^{-1}$  at 0.1 C, and safe operating potential of  $\sim 1.61$  V. Consequently, the  $\text{Al}_{0.2}\text{Fe}_{0.8}\text{Nb}_{11}\text{O}_{29}$  anode exhibited remarkable cycling stability with capacity retention of 92.9% over after 1000 cycles. Based on the results reported in the literature, doping is a promising strategy for improving the conductivity and electrochemical performance of anode materials. This method has been employed in the current research to address the shortcomings of niobium-tungsten oxide anode material.

### 2.4.4 Controlled annealing

Controlled annealing is also an important method of modifying the structure and morphology of materials; this can also influence the conductivity and electrochemical

performance. The annealing process, for instance, improves the lattice mismatch, surface structure, and crystallinity of materials. It also leads to the creation of longer mean paths for the free electrons, which had been reported to enhance the electronic conductivity of materials [68]. For instance, Zhang *et al.* [69] fabricated oxygen-defective cobalt oxide using a two-step strategy. They found that the resulting anode retained a specific capacity of 896 mAh g<sup>-1</sup> after 200 cycles at a current density of 250 mA g<sup>-1</sup>. Zhang *et al.* [70] also found that the excellent electrochemical properties of TiNb<sub>2</sub>O<sub>7</sub> compounds annealed in a unique supercritical fluid system can be attributed to the contribution of oxygen vacancies. Zhu *et al.* [41] also reported that hydrogen treatment created oxygen vacancies in the TiNb<sub>24</sub>O<sub>62</sub> anode, which resulted in the creation of active sites for Li<sup>+</sup> diffusion and improved electronic conductivity. In general, controlled annealing can expand the unit cell volume and create abundant oxygen vacancies in anode materials. These could result in a reduced band gap, enhanced lithium-ion mobility, and improved electronic conductivity [11]. The use of controlled annealing has been explored in this research for enhancing the electrochemical performance of molybdenum-niobium oxide anode material.

#### **2.4.5 Nanostructuring**

The use of nanostructured materials for LIB anode is one of the most efficient strategies for improving the electrochemical performance of anodes. When particle sizes approach the nanoscale, particle surfaces and grain interfaces begin to play a determining role in the thermodynamics and kinetics, and a pseudo-capacitive storage mechanism occurs by accommodating lithium ions on the particle surface/interface, which is not observed with micron-sized particles [56], [71]. Nanostructured materials would offer a substantial contact area between the electrolyte solution and electrodes due to their short ion-diffusion paths.

Additionally, they can withstand more mechanical stress and structural distortion from the insertion and extraction of lithium, which results in a high specific capacity and high rate performance [1].

Various nanostructured materials have been studied for LIBs anode, including (0D) [40], (1D) [72], and (2D) [73]. Compared to (0D), (1D) nanostructures such as nanowires, nanotubes, and nanofibers can provide shortened lithium ion diffusion pathways, rapid electron transport, a large specific surface area, and limited self-aggregation [74]. Li *et al.* [75] fabricated  $\text{ZrNb}_{14}\text{O}_{37}$  nanowires and studied the electrochemical activities. The authors reported that  $\text{ZrNb}_{14}\text{O}_{37}$  nanowires deliver a high specific capacity of  $244.9 \text{ mAh g}^{-1}$ , high rate capability, and excellent cycle performance, with a capacity fading of 0.026% over 1000 cycles. The excellent electrochemical performance was attributed to the construction of the  $\text{ZrNb}_{14}\text{O}_{37}$  nanowires architecture. Ran *et al.* [72] also synthesized both bulk (B- $\text{GeNb}_{18}\text{O}_{47}$ ) and nanowires (N- $\text{GeNb}_{18}\text{O}_{47}$ )  $\text{GeNb}_{18}\text{O}_{47}$ . They confirmed that the N- $\text{GeNb}_{18}\text{O}_{47}$  displays lower redox polarization, higher  $\text{Li}^+$  diffusion coefficient, and lower charge transfer resistance compared to the bulk sample.

In general, nanostructure materials accommodate more mechanical strain and structural distortion during lithium intercalation/de-intercalation, thereby improving the reversibility, cycling stability, and rate performance of anode materials [66]. In this research, a synergetic effects of nanostructure and doping, as well as nanostructure and annealing have been explored to improve the electrochemical performance of  $\text{Nb}_{18}\text{W}_{16}\text{O}_{93}$  and  $\text{MoNb}_{12}\text{O}_{33}$  respectively. The combination of these approaches has been employed to improve the electrochemical activities of anode materials for LIBs as described in chapter three and four. Nonetheless, the combination of these approaches has been rarely explored to enhance the electrochemical performance of

$\text{Nb}_{18}\text{W}_{16}\text{O}_{93}$  and  $\text{MoNb}_{12}\text{O}_{33}$ . Hence, this study provides novel insights into the synergetic effect of these methods on the overall electrochemical performance of  $\text{Nb}_{18}\text{W}_{16}\text{O}_{93}$  and  $\text{MoNb}_{12}\text{O}_{33}$ .

## 2.5 Ceramic nanowires

Over the last few years, there is a growing interest in one-dimensional (1D) nanostructured materials due to their huge potential and numerous areas of applications when compared with other nanostructured materials. This class of materials includes nanofibers, nanotubes, nanorods, nanobelts, and nanowires. Among the existing 1D nanostructured materials, nanowires have attracted tremendous research interest owing to their fascinating properties and complex structures [76]. Nanowires (NWs) generally refer to large aspect ratio rods of 1-100 nm in diameter; the combination of the large aspect ratio and small diameter make them exhibit fundamental solid state phenomena such as the exciton diffusion length, phonon mean free path, exciton Bohr radius, and wavelength of light [77]. All these made it possible to control certain critical properties of nanowires which cannot be controlled in their parent bulk materials [77]. Nanowires have two quantum-confined and one unconfined directions, which endows them with significantly different electrical, magnetic, chemical, and thermal properties compared to their bulk counterparts [78], [79].

Recently, researchers have been focusing on the fabrication of ceramic NWs, and these materials exhibit excellent properties such as high corrosion resistance, larger surface area, interconnected porous structure, large aspect ratio, catalytic behavior, high strength, semiconducting, magnetic properties, wear resistance, high chemical stability, sensibility, high thermal stability, and bio-compatibility [79], [80]. These unique properties hold huge potential for applications in the fields of electronics, medical sensing, drug delivery, energy generation

and storage, optics, and thermoelectricity [76], [79]. The next section outlines various methods of fabricating ceramic nanowires.

## **2.6 Methods of fabricating ceramic nanowires**

The performance of ceramic nanowires in some applications greatly depends on the fabrication methods and the morphology of the end products [81]. In this current review, the most recent highly efficient methods of fabricating ceramic nanowires are the major focus, rather than discussing all existing methods of fabricating these materials.

### **2.6.1 Template-assisted synthesis method**

This is one of the most widely used methods of fabricating ceramic nanowires. The method involves using templates containing tiny cylindrical pores. These empty pores are filled with a chosen material to form ceramic nanowires with similar morphologies to the template pore structure [82]. The length, shape, and size of the resulting ceramic nanowires can easily be tuned by changing different parameters, such as the melting time, temperature, and structure of the templates. Various factors must be considered before selecting a template [83]. Some of these include; the mechanical properties and chemical stability of the template, and the density, diameter, and uniformity of the pores must also be considered [84]. The templates can be in various forms, such as colloids, supramolecular aggregates, molecules, nanoporous matrix, and nanoparticles [85]. It is often required to remove the template to harvest the ceramic nanowires if the template is involved physically. Post-synthesis treatments such as calcination or chemical etching are usually employed for this purpose. The template is usually consumed during the process, and pure ceramic nanowires can be obtained directly during the chemical process [76].

The types of templates used in this method can be categorized into two; the nanoconfined template and the oriented template [86]. Examples of nanoconfined templates include;

polycarbonate (PC) membranes and mesoporous templates, anodic alumina oxide (AAO) templates, and examples of oriented templates are metal nanowires, carbon nanofibres, carbon nanotubes, and inorganic metal oxide [86]. The use of AAO membrane templates is considered the most effective due to its advantages over other templates, including uniform pore distribution, high aspect ratio of pores, and high pore density. In addition, it is easier to fabricate AAO, and the distribution of the length, as well as the diameter of the pores of the template, can be controlled during the fabrication process [79]. There are various available techniques for fabricating ceramic nanowires using the template-assisted method. Some of the techniques include; pressure injection, electrochemical deposition, vapor deposition, and sol-gel deposition [87]–[89]. Ceramic nanowires can also be fabricated by combining two techniques under the template-assisted method. For instance, Miao *et al.* [90] fabricated TiO<sub>2</sub> single-crystal nanowire arrays with diameters of 10 - 40 nm using an electrochemically induced sol-gel technique from an aqueous solution of Ti precursor. The authors reported that combining the two techniques resulted in uniform, continuous, and parallel-aligned nanowires with smooth surfaces. They also explained that the combination of the two techniques made it possible to use templates with very small pores of 20 nm.

### **2.6.2 Vapor-liquid-solid method**

Vapor-liquid-solid (VLS) is the most successful vapor-based method of fabricating ceramic nanowires in large quantities [91]. The method was first developed for synthesizing single-crystal silicon whiskers by Wagner and Ellis in [91] 1964. Since, several researchers have utilized the method for fabricating ceramic nanowires [92]–[95]. The VLS process involves the dissolution of vapor components of the reactants into liquid droplets of metal catalyst nanoparticles. When the liquid metal catalyst becomes supersaturated, the process will result in

the nucleation of the ceramic nanowires to be formed; the nuclei serve as a preferential site for subsequent deposition of the gaseous reactant at the interface of the catalyst liquid droplet, thereby promoting the growth of the nuclei into ceramic nanowires [76]. One of the major requirements of the VLS method is the availability of a good solvent that can form a liquid alloy with the target material [76]. VLS requires a high temperature for the metal catalyst to form a liquid alloy, making it easier to use the method in conjunction with other chemical processes (chemical vapor deposition, carbothermal reduction, laser ablation, and molecular beam epitaxy) that occur at high temperatures [96]. The appropriate selection of metal catalyst plays a vital role in the success of the VLS method because not all metal catalysts are suitable for the process. A good metal catalyst for the VLS method must meet certain requirements: (1) It must be inert and chemically stable; (2) It must be able to form a liquid solution with a solid phase component; (3) The catalyst must not form an intermediate solid [96]–[98]. Previous investigations by various researchers have shown that many noble and transition metals meet these requirements, and for these reasons, they are the most widely used for the VLS process [96].

The properties of the resulting ceramic nanowires depend on the size and physical properties of the metal catalyst droplets [76]. For instance, the size and uniformity of the nanowires can be controlled by using monodispersed metal nanoparticles [86]. Men *et al.* [98] confirmed the correlation between catalyst droplet size and nanowires diameter in their studies. The authors investigated the effects of catalysts and gas input ratio on the size of SiC nanowires using the VLS method. They used different concentrations and diameters of Ni and Fe droplets; the results obtained show that the diameter of SiC nanowires grown using Ni-based catalyst decreased with decreasing diameter of the catalyst droplet, while the diameter of nanowires grown using Fe catalyst was independent of the size of the catalyst droplet. They also reported

that the diameter of nanowires synthesized using Ni catalyst increased with increasing concentration, while the Fe concentration has no effect on the diameter of SiC nanowires. The non-dependence of the diameter of SiC nanowires on the size and concentration of the Fe catalyst was attributed to the high concentration of the catalyst. The dependence of ceramic nanowires' diameter on the size of metal catalyst was also affirmed in the studies carried out by other authors [99], [100].

Recent efforts by researchers [94], [101] have led to the fabrication of ceramic nanowires using the self catalyzed VLS technique. This approach has eliminated the need to carry out after-treatment that is often required to remove the metallic catalyst droplets from the nanowires. The presence of a residual metallic catalyst in ceramic nanowires has been reported to affect their purity, thereby influencing their performance. Self-catalyzed VLS involves an in situ formation of the target ceramic nanowires. This process was demonstrated by Park *et al.* [101] when they studied the growth and mechanism of one-dimensional Al<sub>2</sub>O<sub>3</sub> nanostructures. They reported that the use of the self-catalyzed VLS technique resulted in a high yield of Al<sub>2</sub>O<sub>3</sub> nanowires with uniform diameter and morphology. The same approach was also employed by Wei *et al.* [94] for fabricating zinc oxide nanowires. This method has huge potential for fabricating ceramic nanowires without contamination. However, the mechanisms responsible for controlling the diameters and lengths of nanowires in self-catalyzed VLS is not yet fully understood.

### **2.6.3 Solution–liquid–solid method**

The solution-liquid–solid (SLS) method is quite similar to the VLS technique; one of the major differences between the two methods is that in SLS, the precursors react in the solution rather than the vapor phase. This method was developed for fabricating ceramic nanowires at relatively low temperatures by Trentler and his co-worker [102]. This method has been

successfully used for fabricating ceramic nanowires by various researchers [102]–[104]. The method utilizes a low melting point metal as the catalyst to generate the target material through the decomposition of organometallic precursors in a hydrocarbon solvent. The use of a low melting point metal catalyst makes it possible to reduce the operating temperature of the SLS method to a value below the boiling points of aromatic solvents commonly used [76].

In related work, Li *et al.* [104] successfully fabricated CdSe NWs using SLS. They used low-melting Bi nanodroplets to induce the growth of the NWs. The results obtained from the investigation show that the reactivity and concentration of the nanodroplet Bi precursors, together with the concentration and reactivity of the Cd precursors, determine the morphology and partially determine the crystal structure of the resulting NWs. They also affirmed that the diameter of the resulting NWs varied with reaction parameters such as reaction time, concentration, organic ligands, and temperature. The same approach was also used for fabricating straight and branched PbSe nanowires NWs by Hull *et al.* [103].

#### **2.6.4 Solvothermal method**

Recently, the solvothermal method has been extensively utilized as an effective route for fabricating ceramic NWs by using a solvent under temperature and pressures above its critical point to increase the rate of reactions between solids and enhance the solubility of a solid [76]. This technique usually produces ceramic NWs at low temperatures in comparison with the vapor phase techniques [82]. In this process, a predetermined proportion of precursor and a reagent capable of controlling the crystal growth (such as amines) are added into a solvent. The resulting mixture is then placed in an autoclave to allow the process of crystal growth to proceed at a relatively high temperature and pressure [105]. The process is followed by annealing to create porous ceramic nanowires. This approach is quite versatile because most materials can be made

soluble in a solvent by pressurizing and heating the system within the range of its critical point. This makes solvothermal a suitable method of fabricating ceramic NWs from any solid material [76].

The morphology and diameter of the resulting NWs can be controlled by changing different parameters, such as the solvent and reaction temperature, during the process, as exemplified by the investigations carried out by various researchers [106]–[110]. For instance, Zhang and co-workers [107] studied the effect of solvent concentration and reaction temperature on the morphology and size of ZnS NWs using the solvothermal method. They used a mixture of oleylamine and thiourea as solvents, and the process was carried out at different temperatures. The results obtained from the investigation show that NWs of diameter within the range of 1.7 nm – 3 nm were successfully synthesized by varying the reaction temperature between 140°C and 180°C; the results also indicate that the diameter of the resulting NWs increase with increasing temperature. Similar results were also reported from the studies carried out by other authors [108], [109].

### **2.6.5 Hydrothermal method**

Hydrothermal is a low-temperature method of fabricating ceramic NWs in an autoclave under controlled temperature and pressure using the aqueous solution as a solvent; the amount of solution and temperature of the system usually determine the internal pressure generated in the autoclave [111]. The technique is quite similar to the solvothermal method as both of them can be used for fabricating ceramic NWs at low temperatures using an autoclave [82]. The use of this method has been demonstrated for fabricating ceramic NWS such as  $Y_3BO_7$  [112],  $Na_{0.5}Bi_{0.5}TiO_3$  [113],  $V_2O_5$  [114], ZnO [115], and BaTiO<sub>3</sub> [116]. The crystallinity of ceramic NWs synthesized through the hydrothermal technique can be influenced by various parameters such as reaction

temperature, time, and PH of the solution [113]. The effects of time and reaction temperature on the precipitation of  $\text{Na}_{0.5}\text{Bi}_{0.5}\text{TiO}_3$  (NBT) NWs were studied by Jiang and his co-worker [113]. They synthesized NBT NWs in an autoclave under auto-generated pressure by varying the reaction temperature between  $120^\circ\text{C}$  and  $170^\circ\text{C}$  and the reaction time between 1 h and 48 h. They observed that the crystallinity of the NBT NWs increases with increasing temperature and the NWs fabricated at  $170^\circ\text{C}$  exhibited the highest diffraction peak. The same trend was also observed for the reaction time with the NBT NWs synthesized at 48 h exhibiting the highest crystallinity. They concluded that reaction temperature and time played an important role in determining the final morphologies of the NBT NWs. A similar investigation was also carried out by Alshehri *et al.*, [117] they studied the influence of the zinc precursor, growth temperature, growth duration time, and concentration of  $\text{Na}_2\text{CO}_3$  on the morphology of ZnO synthesized using the hydrothermal method. The results of their investigations show that the length of the ZnO NWs increases with the growth duration time, but it does not have a significant influence on the NWs diameter. They also observed that the aspect ratio of the resulting ZnO NWs increases with increasing base concentration, the average length of the ZnO NWs increased, while the average diameter decreased with increasing concentration of  $\text{Na}_2\text{CO}_3$ . However, the authors affirmed that the use of different salt precursors had no significant influence on the resulting ZnO NWs.

### **2.6.6 Chemical vapor deposition methods**

Chemical vapor deposition (CVD) is a process in which materials in a vapor state are condensed to a solid phase. The method has been widely used for fabricating ceramic NWs by reacting the vapors of the precursor species, and the product gets deposited when it comes into contact with the surface of a heated substrate [118]. The method has been widely used for fabricating various ceramic NWs, including ZnO [119], SiC [88],  $\text{Mg}_2\text{B}_2\text{O}_5$  [120], and  $\text{Si}_3\text{N}_4$

[121]. In a typical CVD process, thermal energy heats the reacting gases in the chamber and drives the deposition process. Various process parameters such as deposition temperature, gas composition, pressure, and flow rate can be varied to control the deposition process [111]. CVD could be carried out using different reactor process types, such as atmospheric pressure chemical vapor deposition (APCVD), plasma-enhanced chemical vapor deposition (PECVD), and low-pressure chemical vapor deposition (LPCVD). The choice of a reactor process for CVD is usually influenced by factors such as type of substrate, morphology, cost, and uniformity [118].

Different forms of CVD have been carried out to fabricate ceramic NWs. Fu and co-workers [88] fabricated SiC NWs using CVD without a metallic catalyst and investigated the effect of deposition temperature and concentration of methyl trichlorosilane (MTS) on the process. The process was carried out in a furnace at 1050 –1150 °C for 2 h under normal atmospheric pressure using H<sub>2</sub>S as both carrier and diluent gas. The results obtained from the investigation show that the SiC crystal dimensions increased with increasing deposition temperature and MTS concentration, while the morphologies of the as-grown SiC crystal also changed from NWs to grains. Therefore, it is crucial to control different process parameters in CVD to fabricate ceramic NWs of desired morphology.

### **2.6.7 Electrospinning technique**

Electrospinning has been widely employed to produce nanofibers from the majority of organic polymers. This has prompted several researchers to investigate electrospun polymer nanofibers, and the process has been utilized primarily to produce polymer nanofibers. In contrast, ceramics are often not regarded as electrospinnable unless they are in a molten condition at high temperatures [122]. Electrospinning has become the most widely used technique for fabricating ceramic nanowires due to its low cost, simplicity, high yield, tunable porosity, high surface-to-

volume ratio, control over various process parameters, and ability to control the nanofiber composition [123].

#### **2.6.7.1 Principle of electrospinning technique and basic set-up**

The electrospinning technique is based on an earlier observation of William Gilbert while studying the interaction of the liquid with electrostatic force in the year 1600 [124]. He discovered that a drop of water on a surface was drawn into a cone when a piece of rubbed amber was held at a certain distance above. He explained that the electric field induced charges to form on the surface of the water droplet, which resulted in the surface tension of the liquid being opposed by electrostatic forces.

Electrospinning requires three key components: a high-voltage power supply, a collector, and a syringe [124]. In a typical electrospinning process, a polymer solution is delivered to the tip of the syringe, and a high voltage is then applied to generate a potential difference between the solution at the tip of the needle and the collector. This voltage difference causes the droplet to deform into a Taylor cone. An increase in the applied voltage results in jet initiation from the cone when the electrostatic force is greater than the surface tension of the polymer solution at the tip of the needle, and the polymer jet is expelled into the electric field. The electric field renders the jet unstable; consequently, the jet experiences a bending motion in response to coulombic repulsion, and the polymer jet is stretched into nanofibers [125]. The dry or semi-dry nanofibers are deposited on a collector [125]. The next section discusses the electrospinning of ceramic nanofibers.

#### **2.6.7.2 Electrospinning of ceramic nanofibers**

Typical procedures for fabricating ceramic nanofibers involve preparing an electrospinnable solution by dissolving precursor salt and a polymer in a suitable solvent,

spinning the prepared solution to produce composite nanofibers consisting of the precursor salt and carrier polymer, and finally sintering the electrospun nanofibers composite at high temperatures to remove the associated organic components [126]. Several precursor solutions that can be used for fabricating ceramic nanofibers exist, and each of these precursor solutions has advantages and shortcomings. For instance, an inorganic solution has been reported to be thermostatically unstable because its viscosity changes with aging time, making it difficult to fabricate uniform nanofibers continuously [127].

Recent advances have led to the development of two methods for fabricating electrospun ceramic nanofibers via solutions: the first method involves the spinning of an aged metal alkoxide precursor sol-gel solution, and the second method involves the spinning of solutions containing metal alkoxides precursor and polymer [127]. The first method generally results in the formation of dense ceramic nanofibers in the micrometer range because it is difficult to control the uniformity and size of the fibers. Therefore, the second method, which utilizes an organic polymer solution has been reported to be the most suitable and efficient way of fabricating ceramic nanofibers because the process could be easily adjusted to produce more uniform nanofibers with a smaller diameter [127]. The most widely used polymer for fabricating ceramic nanofibers is polyvinyl pyrrolidone (PVP) because of its spinnability and ability to dissolve in water and ethanol [125]. Other polymers such as polyvinyl alcohol (PVA), poly methyl methacrylate (PMMA), poly acrylic acid (PAA), and polyethylene oxide (PEO) have also been reported to be suitable for fabricating ceramic nanofibers [126]. The following section outlines the important parameters to be considered while fabricating ceramic nanowires.

### 2.6.7.3 Influence of working parameters on electrospinning of ceramic nanofibers

Various researchers have studied the effect of process parameters on the properties of electrospun ceramic nanofibers [128]–[134]. The results obtained from these investigations show that the properties of electrospun ceramic NWs are influenced by various working parameters such as applied voltage, solution composition, electric field strength, type of collector, polymer solution feed rate, and drop height. Therefore, it is important to understand how these parameters influence the morphology and properties of electrospun nanofibres; this will help in selecting a combination of suitable processing parameters for fabricating nanofibres with desired characteristics for different applications using this technique. These working parameters can be categorized into three types; (i) processing parameters (polymer solution flow rate, applied voltage, types of collector and needle-to-collector distance), solution parameters (polymer concentration, molecular weight of polymer, solution conductivity, and solution viscosity), and ambient parameters (temperature and humidity).

Someswararao *et al.* [129] investigated the effect of process parameters on the morphology and diameter of electrospun TiO<sub>2</sub> nanofibers; they varied process parameters such as spinning distance, applied voltage, polymer (PVP), and solution flow rate. The results of the studies show that increasing the applied voltage and the spinning distance resulted in the reduction of the average diameter of the nanofibers from 293 to 175 nm and 259 to 147 nm, respectively. They explained that increasing the applied voltage usually enhances the electrostatic force on the solution thereby causing stretching of the jet, hence, leading to the reduction of the nanofibers' diameter. Furthermore, they observed that decreasing the flow rate and PVP concentration led to a corresponding reduction in the average diameter of the nanofibers. This trend was attributed to the fact that a high flow rate decreases the charge

density, which usually results in a large nanofibers diameter. A similar result was also reported by Panda *et al.* [132] and Evcin *et al.* [135] when they investigated the effect of process parameters on the diameter and morphology of alumina and aluminum titanate nanofibers, respectively. Hence, various researchers have confirmed that it is necessary to determine the combination of working parameters at which nanofibres with optimum characteristics can be synthesized. This forms an integral part of the objectives of this study, which are highlighted in the next section.

## 2.7 Objectives

The main objective of this research is to fabricate  $\text{Nb}_{18}\text{W}_{16}\text{O}_{93}$  and  $\text{MoNb}_{12}\text{O}_{33}$  oxide nanowires using an electrospinning technique and enhance their electrochemical performance through doping and controlled annealing in a mixture of argon and hydrogen. The following are the specific objectives of this research:

1. Study the influence of process parameters on morphology and diameter of electrospun  $\text{Nb}_{18}\text{W}_{16}\text{O}_{93}$  and  $\text{MoNb}_{12}\text{O}_{33}$  nanofibers.
2. Fabricate  $\text{Nb}_{18}\text{W}_{16}\text{O}_{93}$  and  $\text{MoNb}_{12}\text{O}_{33}$  oxide nanowires using the electrospinning technique.
3. Investigate the effect of nickel doping on the electrochemical performance of  $\text{Nb}_{18}\text{W}_{16}\text{O}_{93}$  nanowires.
4. Study the effect of controlled annealing on the electrochemical properties of  $\text{MoNb}_{12}\text{O}_{33}$  nanowires for lithium-ion battery application.

## **Chapter 3: Optimization of the Electrospun Niobium–Tungsten Oxide Nanofibers Diameter Using Response Surface Methodology**

**Babajide Oluwagbenga Fatile<sup>1</sup>, Martin Pugh<sup>1</sup> and Mamoun Medraj<sup>1,\*</sup>**

<sup>1</sup>Department of Mechanical, Industrial and Aerospace Engineering, Concordia University, Montreal, Canada; mamoun.medraj@concordia.ca

This paper has been published in *Nanomaterials*, Vol. 11, 2021, 1644.  
doi:10.3390/nano11071644

### **Abstract**

The present research aimed to investigate the effect of working parameters on the electrospinning of niobium-tungsten oxide nanofibers and optimize the process using central composite design (CCD) based on the response surface methodology (RSM). An experiment was designed to assess the effects of five variables including the applied voltage (V), spinning distance (D), polymer concentration (P), flow rate (F), and addition of NaCl (N) on the resulting diameter of the nanofibers. Meanwhile, a second-order prediction model of nanofibers diameter was fitted and verified using analysis of variance (ANOVA). The results show that the diameter of the nanofibers was significantly influenced by all the variables except the flow rate. Some second-order and cross factor interactions such as VD, DP, PF, PN, and P<sup>2</sup> also have significant effects on the diameter of the nanofibers. The results of the ANOVA yielded R<sup>2</sup> and adjusted R<sup>2</sup> values of 0.96 and 0.93 respectively. This affirmed that the predictive model fitted well with the experimental data. Furthermore, the process parameters were optimized using the CCD method and a maximum desirability function of 226 nm was achieved for the diameter of the nanofibers. This is very close to the 233 nm diameter obtained from a confirmatory experiment using the optimum conditions. Therefore, the model is representative of the process and it could be used for future studies for the reduction of the diameter of electrospun nanofibers.

**Keywords:** Niobium-tungsten oxide; nanofibers; electrospinning; optimization; response surface methodology

### **3.1. Introduction**

Over the last few years, researchers are focusing on the fabrication of ceramic nanofibers with large surface-to-volume ratios as these materials have potential applications where high porosity is desirable [82]. In the previous decades, there were difficulties in synthesizing one-dimensional nanostructures of high purity due to the lack of suitable manufacturing routes [86]. Various techniques for fabricating nanofibers had been reported in the literature and some of the most widely used techniques include; flash spinning, self-assembly, phase separation, drawing-processing, electrospinning, template-assisted synthesis, melt blowing, electrochemical deposition and solvent casting [47], [136]–[138]. Among these methods, electrospinning has become the most widely used technique due to its low cost, simplicity, high yield, tunable porosity, high surface-to-volume ratio, control over various process parameters, and ability to control the nanofiber composition [123], [139]. Electrospinning is regarded as an efficient method of synthesizing nanofibers due to its ability to process different types of polymers and its consistency in synthesizing nanofibers with controllable morphology and diameter [86]. Additionally, the electrospinning technique is beneficial for fabricating nanostructures from varieties of raw materials. This method combines the use of electrospray and spinning processes to achieve a highly efficient technique suitable for spinning different types of fibers from polymer solutions or melts [86]. These unique advantages of electrospinning had attracted researchers from different fields for synthesizing different nanostructures for various applications such as; optical electronics, healthcare, filtration, biomedical, defence and security,

nanocatalysis, environmental engineering, biotechnology, protective clothing, pharmaceutical, and nanofiber reinforced composites [124], [139].

Electrospinning has been widely used for fabricating nanofibers from most organic polymers because it is easier to prepare a polymer solution with the required rheological properties for electrospinning [140], [141]. This has motivated several researchers to carry out investigations on electrospun polymer nanofibers and the technique has been majorly used for fabricating polymer nanofibers. On the other hand, ceramics are generally considered not to be electrospinnable alone except at high temperatures when they are in a molten state [122]. Recent efforts [79], [127], [136] by several researchers have led to the fabrication of ceramic nanofibers through electrospinning using spinnable precursors. Typical procedures for fabricating ceramic nanofibers involve the preparation of an electrospinnable sol by dissolving precursor salt and a polymer in a suitable solvent: the next step is to spin the prepared solution to produce composites nanofibers consisting of the precursor salt and a carrier polymer, while the last step is to sinter the electrospun nanofibers composite at high temperatures to remove the associated organic components [126], [127].

Most recently, ceramic nanowires are being explored as potential electrode materials for electrochemical energy storage devices. One of the ceramic nanowires currently being explored for this purpose is niobium-tungsten oxide nanowires [142]. This material has been reported to exhibit open crystal structures as well as valence state changes of niobium and tungsten ions [142]. These unique attributes offer high specific capacity and cycling performance which makes it suitable for storing lithium (Li) ions without any noticeable structural changes [142]. The theoretical capacity of niobium-tungsten oxide nanowires is  $293.56 \text{ mAh g}^{-1}$  [49], this is significantly higher than those of  $\text{H}_2\text{Ti}_{12}\text{O}_{25}$  ( $229 \text{ mAh g}^{-1}$ ) [143],  $\text{Li}_4\text{Ti}_5\text{O}_{12}$  ( $175 \text{ mAh g}^{-1}$ )

[144], and  $\text{Li}_2\text{Ti}_3\text{O}_7$  ( $198 \text{ mAh g}^{-1}$ ) [145]. Besides, niobium-tungsten oxide nanowires have demonstrated, significant structural stability, high power density, as well as environmental friendliness in comparison with other potential anode materials [49]. Several approaches including sol-gel and solid-state methods have been used to fabricate niobium-tungsten oxide nanowires. However, these methods have been reported to involve complicated processes [144]–[146]. As a result of this, it is desirable to develop a simple, versatile and highly efficient technique for fabricating niobium-tungsten oxide nanowires. In 2017, Yan *et al.* [142] made the first attempt to fabricate niobium-tungsten oxide nanowires using the electrospinning technique and these authors also studied the lithium-ion storage capability of the material. In 2018, the authors went further by characterizing niobium-tungsten oxide nanowires as a potential anode for lithium-ion batteries (LiBs) [49].

Over the last few decades, various attempts had been made to understand the effects of working parameters such as applied voltage, solution composition, electric field strength, type of collector, and polymer solution flow rate on the diameter and morphology of electrospun ceramic nanofibers such as  $\text{TiO}_2$  [129]. However, the control of nanofibers' diameter, morphology, and properties still poses some challenges. Moreover, the combination of precursor salt, solvent and polymer usually influence the behaviour of the electrospinning solution. Thus, it is imperative to understand how the contents of the electrospinning solution and other working parameters influence the morphology and properties of electrospun ceramic nanofibers, this will help in selecting a combination of suitable processing parameters for fabricating nanofibers with desired characteristics for various applications.

The use of various statistical experimental design methods for studying the effects of variables on chemical processes had been reported by several authors [147]–[150]. These tools

are useful for the design of experiments, construction of numerical models, evaluation of the effects of variables, and optimization of processes. Among the available experimental design methods, Response Surface Model (RSM) has been widely used by various researchers for process optimization [131], [151]. RSM utilizes a set of advanced experimental design techniques that makes it easier to study the effects of factors on a system and optimize the response. It is also suitable for fitting a second-order prediction equation for the response from fewer experimental results: the quadratic terms in the model equation are useful for modeling curvature in the true response function and this provides additional information for a better understanding of a process [152]. Central Composite Design (CCD) is one of the most widely used RSM. It is an advanced factorial design with center points, complimented with a star or axial points. The additional centre and star points help to increase the accuracy of the estimate for the first and second-order terms in the model equation [152]. The use of CCD is suitable for this current research. However, it can be practically impossible in certain processes to perform experiments at the extreme levels of some variables which tend to be a drawback of this design [153]. Nevertheless, optimization of the electrospinning process for fabricating nanofibers is currently receiving attention, demonstrating the suitability of this design for the optimization of the electrospinning process [154]–[156]. In addition to RSM, other systematic approaches with new algorithms and designs are currently being explored for materials optimization [157]–[159].

The process of fabricating niobium-tungsten oxide nanofibers and their potential as an anode material for LIBs had been reported [49], [142]. To the best of our knowledge, the effects of working parameters on the electrospinning of niobium-tungsten oxide nanofibers have not been investigated. To this end, this current research aims at (1) investigating the effects of applied voltage, spinning distance, polyvinylpyrrolidone (PVP) content, flow rate, and addition

of sodium chloride (NaCl) on the morphology and diameter of niobium-tungsten nanofibers, (2) developing a response surface model (Box–Wilson Central Composite Design (CCD)) to predict the diameter of niobium-tungsten nanofibers, and (3) finding the optimum conditions for fabricating niobium-tungsten oxide nanofibers with minimum diameter.

## **3.2. Materials and methods**

### **3.2.1 Design of experiment**

The experimental design and results analysis in this research were carried out using JMP Pro version 9.0.2 software. Potential parameters that can influence the electrospinning process are numerous and it is difficult to investigate all of them in one single research due to time and cost. In this regard, series of preliminary investigations and extensive literature review were carried out to select the most influential factors. Furthermore, the factors selected in this research appeared to be similar to those investigated by other authors [129], [131], [156].

Before optimization, screening experiments were conducted using fractional factorial design. These helped in identifying the most significant factors from the list of all potential factors. The screening experiment was much more useful because it also provided the feasibility range for each factor to obtain uniform nanofibers. The results obtained from the screening experiments are summarized in Table 3-1. After the screening experiments were completed, the Box–Wilson Central Composite Design (CCD) was utilized to design experiments involving five continuous factors. The factors included applied voltage, spinning distance, polymer concentration, flow rate, and addition of NaCl at five coded levels,  $+\alpha$ ,  $+1$ ,  $0$ ,  $-1$ , and  $-\alpha$  (the value of  $\alpha$  is 2.00 in this work) as shown in Table 3-2.

The CCD generated thirty-six experimental runs including ten as the replication of the central points. All the experiments were executed in random order and the corresponding values of the diameter of the nanofibers were recorded as the response.

Table 3-1: Summary of the preliminary investigation results

<i>Parameters</i>	<i>Effect on the nanofibers diameter and morphology</i>
Applied voltage	Electrospinning process requires an applied voltage beyond the critical value before nanofibers can be obtained. During the screening process, nanofibers were not produced when the voltage was below 14 kV. Nonetheless, nanofibers with irregular shapes and sizes were obtained when the voltage was between 15 kV and 18 kV. Further increase in the applied voltage between 19 kV and 27 kV resulted in the formation of uniform nanofibers. As the voltage increased beyond 28 kV, nanofibers with beads and irregular morphology were obtained.
Polymer concentration	Nanofibers were not obtained when the polymer concentration was below 7.3 wt. %. Above a polymer concentration of 7.3 wt. %, nanofibers with fairly uniform morphology were obtained. As the polymer concentration exceeded 11.8 wt. %, the morphology of the resulting nanofibers became irregular.
Spinning distance	Nanofibers with large diameters were obtained at a spinning distance below 16 cm, while beaded nanofibers were obtained above a spinning distance of 27 cm.
Flow rate	Deposition of unspun droplets on the collector was observed when the flow rate was set above 2.2 mlhr <sup>-1</sup> . It is also observed that a flow rate below 0.65 ml/hr. was not suitable for obtaining continuous nanofibers.
Type of collector	The screening experiments were carried out using a stationary plate and rotating drum collectors. The results showed that there is no significant difference in the diameter of the nanofibers obtained from the two collectors.

Table 3-2: The factors and associated levels for experimental design

Factors	Coded factors	Coded levels				
		+ $\alpha$	+1	0	-1	- $\alpha$
Applied Voltage (kV)	V	25	24	23	22	21
Spinning Distance (cm)	D	26	24	22	20	18
Polymer Conc. (wt.%)	P	11.20	10.30	9.40	8.50	7.60
Flow Rate (ml/hr.)	F	2.05	1.70	1.35	1	0.65
NaCl Conc. (wt.%)	N	1.05	0.80	0.55	0.30	0.05

### 3.2.2 Preparation of the precursor solution

The precursor solution for electrospinning was prepared using niobium oxalate (98%, Sigma Aldrich), ammonium metatungstate hydrate (99.5%, Sigma Aldrich), polyvinylpyrrolidone (MW 1,300,000  $\text{g mol}^{-1}$ , 100% purity, Sigma Aldrich), ethanol (96.9%, Sigma Aldrich) and nitric acid (99.5%, Fischer Scientific). All the materials used in this research were of analytical grade. Firstly, a certain amount of NaCl (as listed in Table 3-3) was dissolved in the mixture of deionized water (5 ml) and ethanol (15 ml) with continuous stirring for 12 h. This was followed by the addition of 0.5 g niobium oxalate, 0.2 g ammonium metatungstate, and 1.0 g citric acid to the mixture with continuous stirring for 24 h to obtain a homogeneous solution. Then, a variable amount of PVP was added according to the experimental design in Table 3-3. The resulting mixture was stirred continuously for 12 h to obtain a viscous precursor solution. The procedure was repeated for preparing the precursor solution for all the experimental runs.

Table 3-3: Experimental design and results

Run Order	Applied Voltage (kV)	Spinning Distance (cm)	Polymer Conc. (wt.%)	Flow Rate (ml hr <sup>-1</sup> )	Conc of Nacl (wt.%)	Nanofibers Diameter (nm)
1	23	22	9.40	2.05	0.55	287.2
2	23	22	9.40	1.35	0.55	303.0
3	22	20	10.30	1.70	0.30	390.1
4	23	26	9.40	1.35	0.55	263.1
5	24	24	10.30	1.70	0.30	312.0
6	23	22	9.40	1.35	0.55	288.2
7	23	22	9.40	1.35	0.55	274.0
8	24	20	8.50	1.70	0.30	245.2
9	24	24	8.50	1.70	0.80	239.9
10	23	22	9.40	1.35	0.55	285.1
11	23	22	9.40	0.65	0.55	287.3
12	22	20	8.50	1.00	0.30	294.5
13	24	20	8.50	1.00	0.80	231.6
14	23	22	11.20	1.35	0.55	404.8
15	21	22	9.40	1.35	0.55	323.2
16	23	22	9.40	1.35	0.55	300.6
17	24	20	10.30	1.00	0.30	312.3
18	25	22	9.40	1.35	0.55	260.1
19	22	24	8.50	1.00	0.80	302.1
20	22	20	10.30	1.00	0.80	346.5
21	22	24	8.50	1.70	0.30	253.4
22	23	22	9.40	1.35	0.55	285.3
23	24	20	10.30	1.70	0.80	299.4
24	23	22	9.40	1.35	0.55	294.3
25	22	24	10.30	1.70	0.80	305.0
26	23	22	7.60	1.35	0.55	272.5
27	22	20	8.50	1.70	0.80	277.3
28	23	22	9.40	1.35	0.05	301.1
29	23	22	9.40	1.35	0.55	276.4
30	23	18	9.40	1.35	0.55	319.0
31	23	22	9.40	1.35	0.55	286.4
32	23	22	9.40	1.35	0.55	288.2
33	24	24	10.30	1.00	0.80	276.4
34	23	22	9.40	1.35	1.05	269.5
35	22	24	10.30	1.00	0.30	313.2
36	24	24	8.50	1.00	0.30	255.8

### 3.2.3 Electrospinning of nanofibers

The niobium-tungsten oxide nanofibres were fabricated based on the experimental design in Table 3-2. All experiments were randomly carried out to eliminate systematic bias in the responses. The fabrication process was carried out by transferring the precursor solution into a plastic syringe with a stainless steel needle. An aluminum foil was employed as the collector with the spinning distance of 18 – 26 cm, while the flow rate of the pump was varied between 0.65 and 2.05 ml hr<sup>-1</sup>. A potential difference of (21–25 kV) was applied to the droplet of the precursor solution at the tip of the needle, the application of high voltage results in the deformation of the droplet. The polymer jet is ejected into the electric field and this causes the jet to undergo a bending movement under columbic repulsion and the polymer jet is stretched into nanofibres before being deposited on the collector. A schematic diagram of the electrospinning process is shown in Figure 3.1.

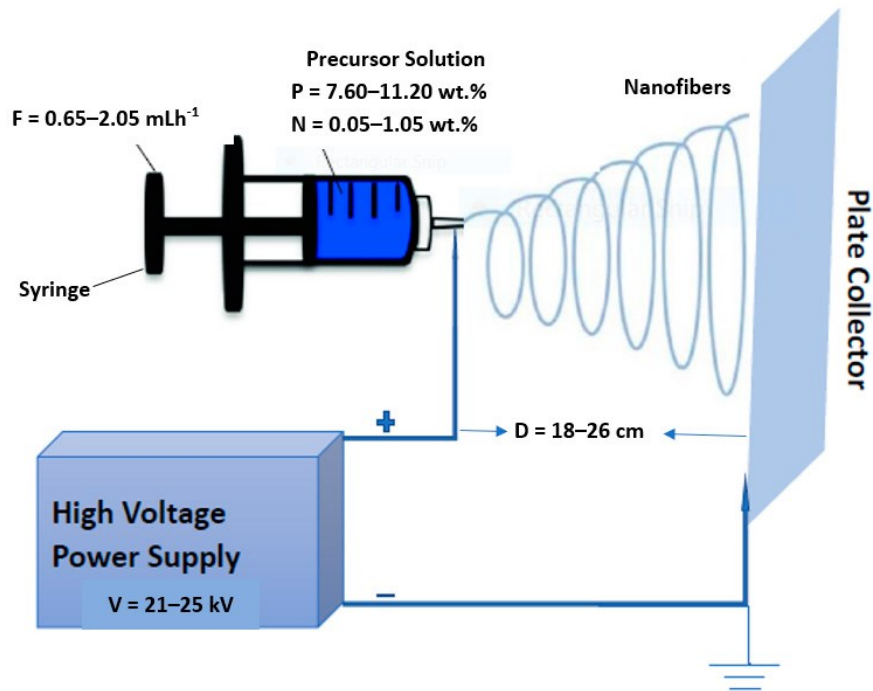
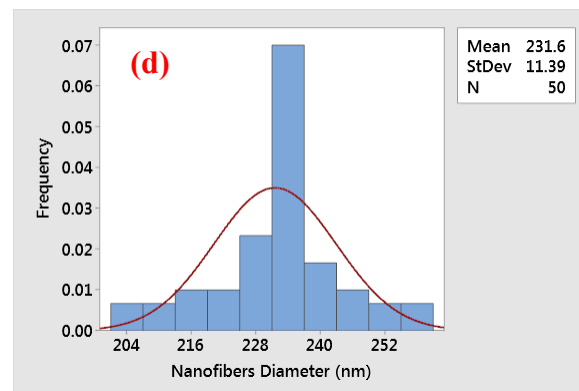
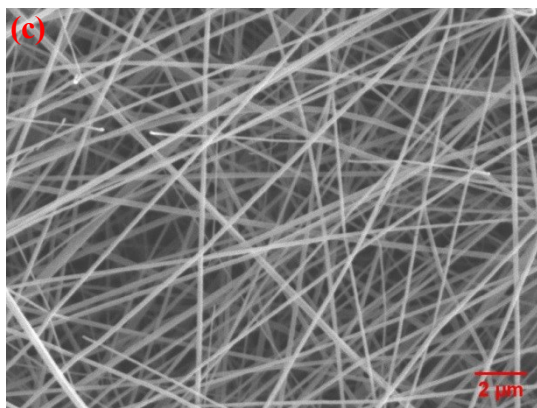
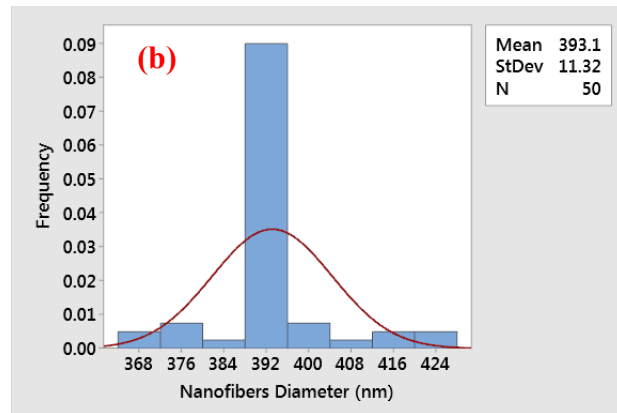
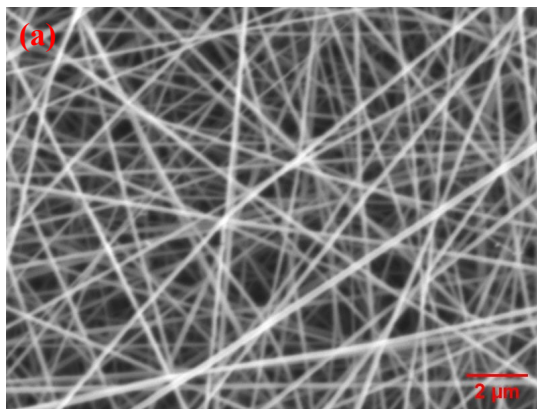
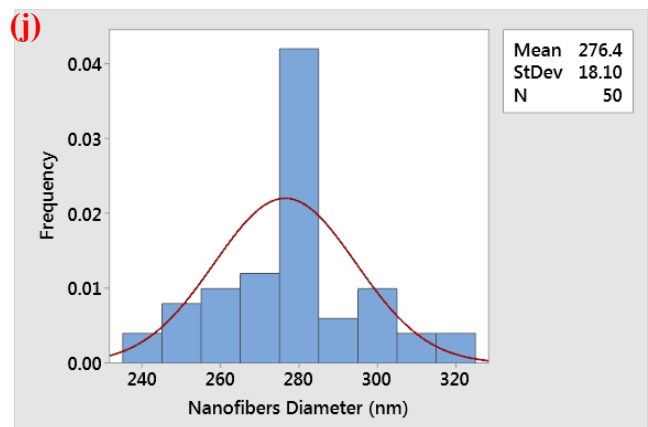
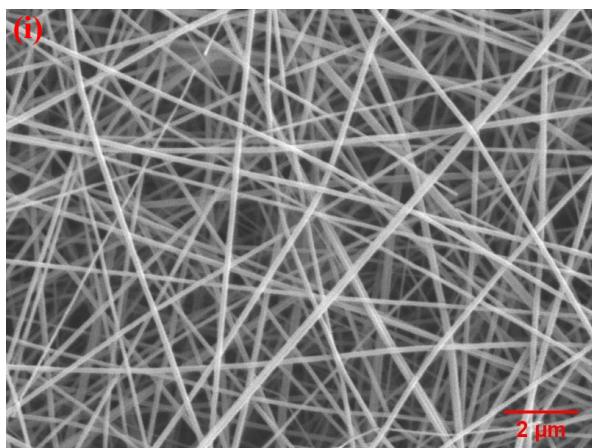
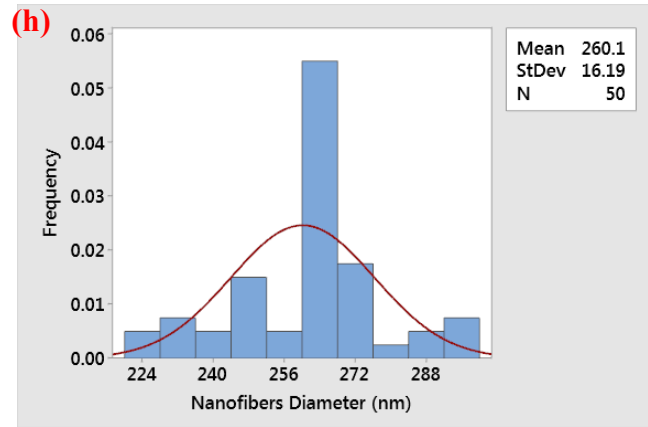
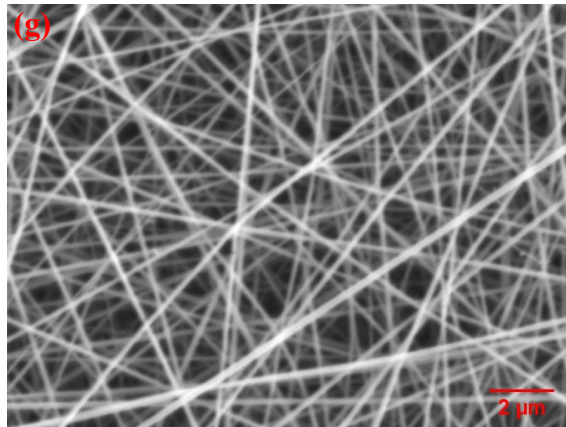
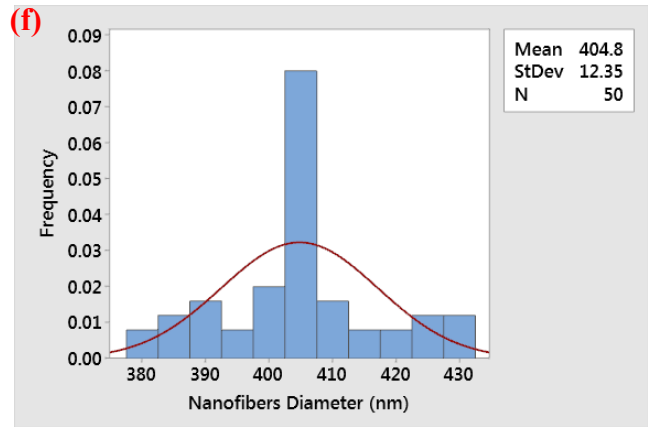
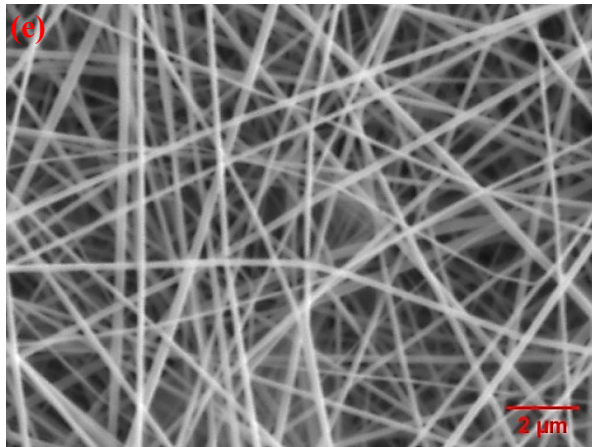


Figure 3-1: Schematic diagram of the electrospinning process

### 3.2.4. Measurement of the nanofibers diameter

Micrographs of the nanofibers fabricated under different experimental conditions were obtained using a Scanning Electron Microscope (SEM) (HITACHI, Chiyoda-Ku, Tokyo, Japan). The average nanofiber diameter for each of the experiments was determined by measuring the diameter of 50 randomly selected nanofibers (Figure 3-2) using Image J software [160]. Before the average nanofibers diameter for each of the experiments was determined, the diameter of the selected nanofibers was initially measured at various spots, and it was observed that each of the nanofibers has a fairly uniform diameter. The results obtained for each of the experiments are presented in Table 3-3.





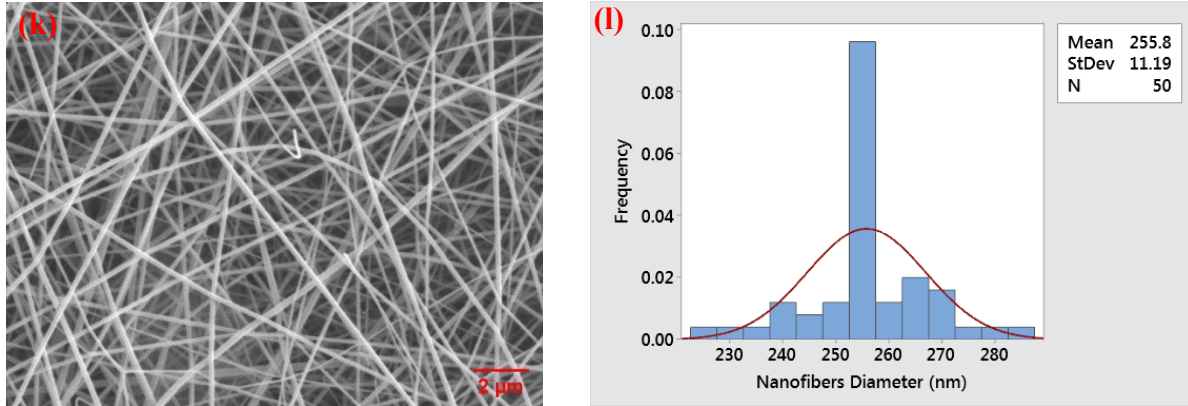


Figure 3-2: SEM micrographs and nanofibers diameter distribution corresponding to the experimental run numbers in Table 3, as follows: (a,b) 3, (c,d) 13, (e,f) 14, (g,h) 18, (i,j) 29, and (k,l) 36.

### 3.2.5. Development of the CCD response surface model

A model Equation (3-1) that describes the diameter of the niobium–tungsten oxide nanofibers ( $df$ ) as a function of the five factors ( $V$ ,  $D$ ,  $P$ ,  $F$ , and  $N$ ) was determined in terms of the coded factors by performing multiple regression analysis on the experimental data. An analysis of variance (ANOVA) of the response was also conducted to evaluate the full second-order polynomial approximation of the response surface model. The significance of each coefficient of the model equation was determined using the corresponding p-value.

## 3.3. Results and Discussions

### 3.3.1 Estimation of coefficients in the mathematical model equation

The result of the multiple regression analysis (Table 3-4) yielded equation (1) which represents a mathematical relationship between the response (nanofibers diameter,  $df$ ) and the factors in a coded unit:

$$df = 2887 - 112.1 V - 49.3 D - 127 P - 252 F + 463 N + 13.42 P^2 - 16.1 F^2 - 39.5 N^2 + 4.07 VD + 9.09 VF - 14.43 VN - 5.01 DP - 5.74 DF + 9.54 DN + 25.06 PF - 28.40 PN - 42.80 FN \quad (3-1)$$

Table 3-4: Estimation of the model coefficient and corresponding p-values

Source	Sum of Squares	DF	f-values	p-values
Model	42538.10	17	26.94	<0.0001
V	7909.77	1	85.16	<0.0001
D	2622.95	1	28.24	<0.0001
P	21582.00	1	232.36	<0.0001
F	4.42	1	0.05	0.8298
N	1086.76	1	11.70	0.0030
VD	1061.13	1	11.42	0.0033
DP	1301.41	1	14.01	0.0015
VF	161.93	1	1.74	0.2033
DF	258.41	1	2.78	0.1126
PF	996.98	1	10.73	0.0042
VN	208.08	1	2.24	0.1518
DN	363.86	1	3.92	0.0633
PN	654.08	1	7.04	0.0162
FN	224.25	1	2.41	0.1376
P <sup>2</sup>	3782.33	1	40.72	<0.0001
F <sup>2</sup>	125.22	1	1.35	0.2608
N <sup>2</sup>	194.54	1	2.09	0.1650
Lack of fit	899.74	9	1.17	0.4117
Pure error	772.13	9		
Cor total	44209.96	35		

$$R^2 = 0.96, \text{Adj. } R^2 = 0.93$$

The significance of each parameter in the model equation including quadratic, cross factor interactions, and linear was evaluated to affirm the effect of each term in the model together with their interactions using ANOVA at 95% confidence level and probability values (p-values) from Fisher's (F) exact test. At 95% confidence level, model equation parameters with p-values less than 0.05 are significant while the model equation parameters with p-values greater than 0.05 are non-significant [148], [151], [161]. The results obtained from this study show that the terms V, D, P, N, VD, DP, PF, PN, and  $P^2$  were significant in the model. The f-value was also used to confirm the level of significance of the model terms. The level of significance was based on the magnitude of f-values, with a higher value representing a larger influence on the process being studied [147]. Hence, the results obtained from the f-values are in agreement with those of the p-values.

### **3.3.2. Verification of the response surface model**

The efficiency of the developed model was verified by computing the linear correlation coefficient as shown in Figure 3-3a. This was used to obtain the determination coefficient ( $R^2$ ) and the adjusted  $R^2$  for the model by plotting the diameter of the experimental nanofibers against the model predicted nanofibers diameter. The value of the ( $R^2 = 0.96$ ) shows that only 4.0% of the total variations are not explained by the model. Additionally, the value obtained for the adjusted  $R^2$  (0.93) is high,  $R^2$  and adjusted  $R^2$  close to 1.0 indicate that there are minor discrepancies between the predicted and experimental nanofibers diameter [147], [148], [151]. The assumption of the constant variance was also confirmed using the plot of the internally studentized residual against the predicted values. The results presented in Figure 3-3b show that the sample points were randomly scattered within the outlier detection limits of -2 to +2 [151]. This confirms the correlation of the prediction model with the experimental data.

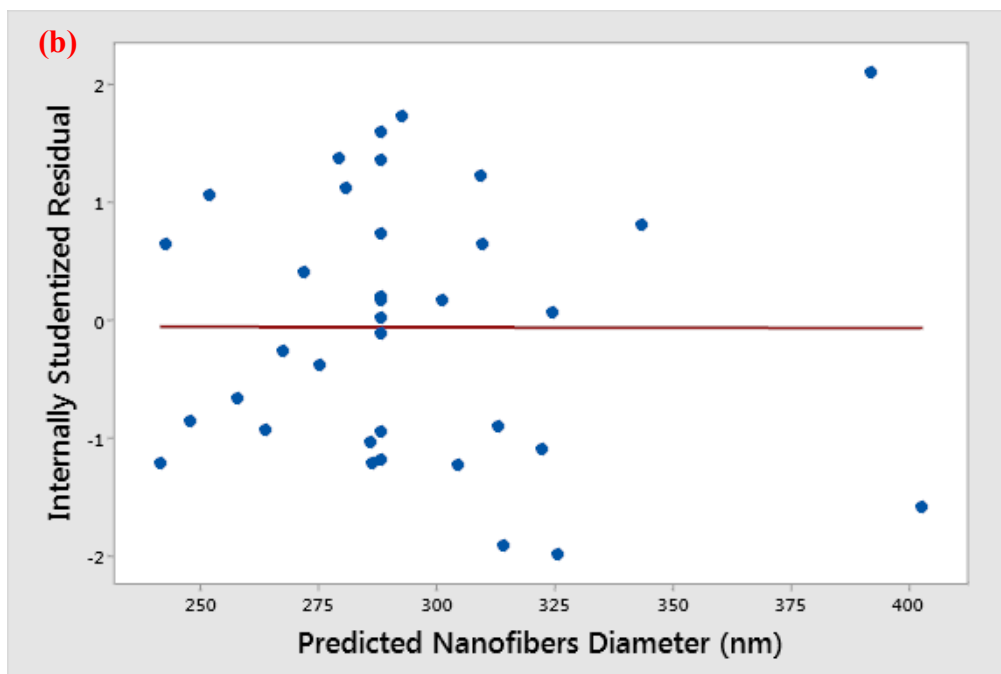
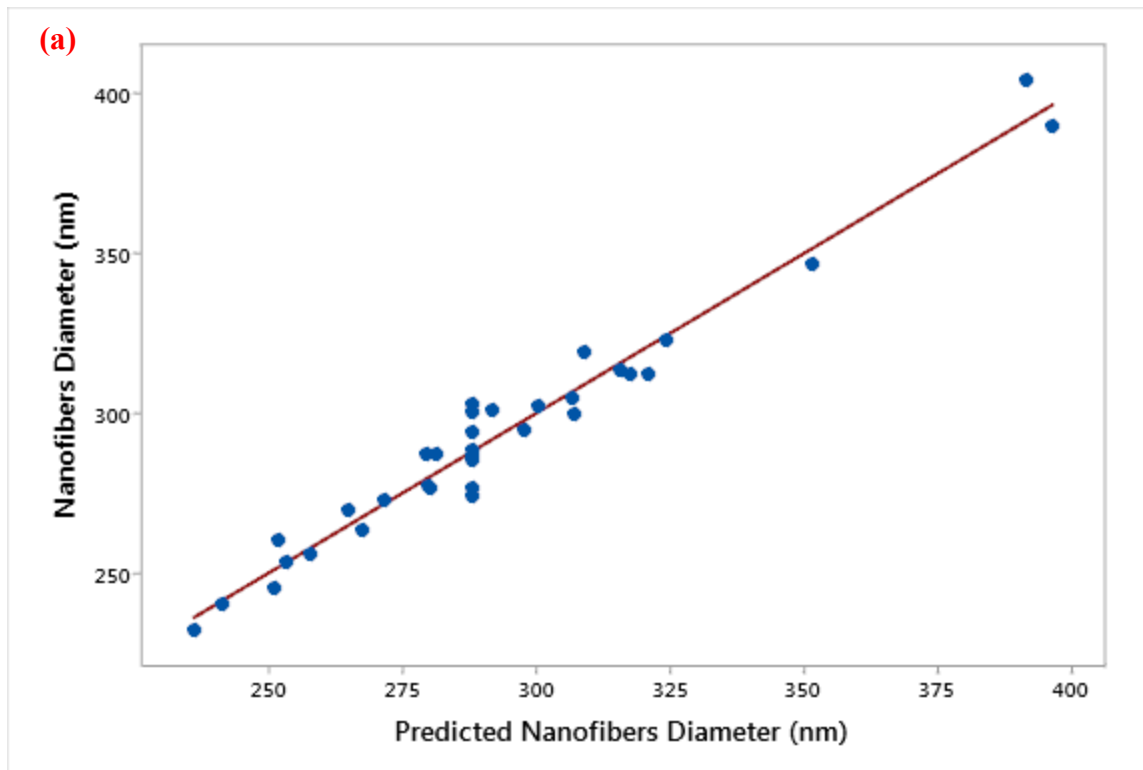


Figure 3-3: Validation of the nanofibres diameter model using (a) observed experimental data versus predicted values (b) internally studentized residuals versus predicted value.

The accuracy of the prediction model was also verified by ANOVA. The results presented in Table 3-4 show that the regression model is highly significant owing to its very low p-value. The insignificant lack of fit also affirms that the predictive model fitted well with the observed data [131], [147], [151]. All these results show that the predicted model is accurate, and it is reliable for representing and optimizing the diameter of the nanofibers.

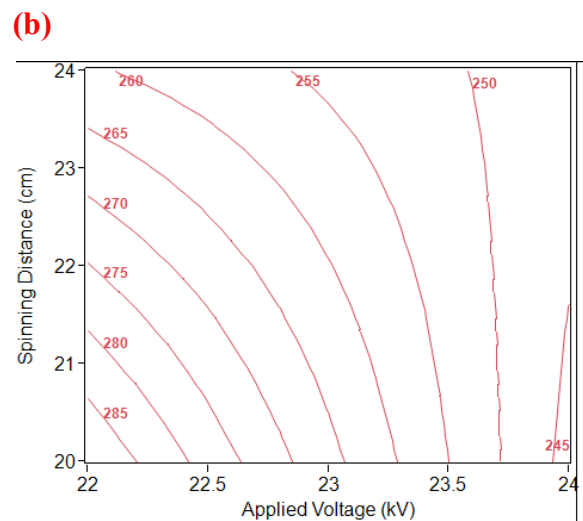
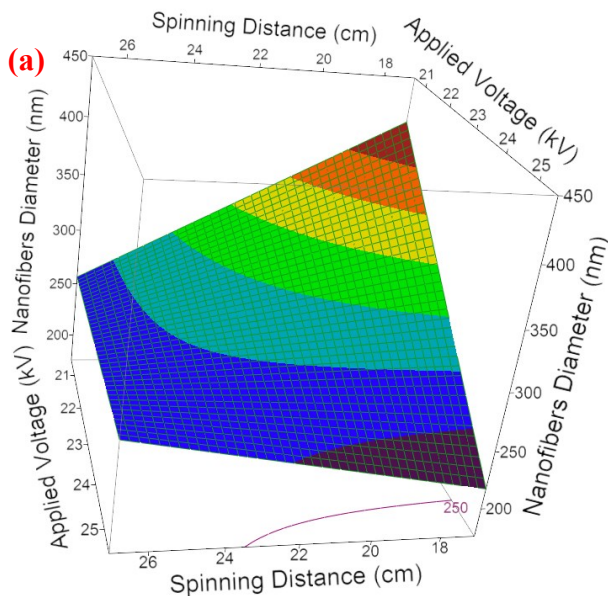
### **3.3.3. Visualization of the interactions between the model parameters**

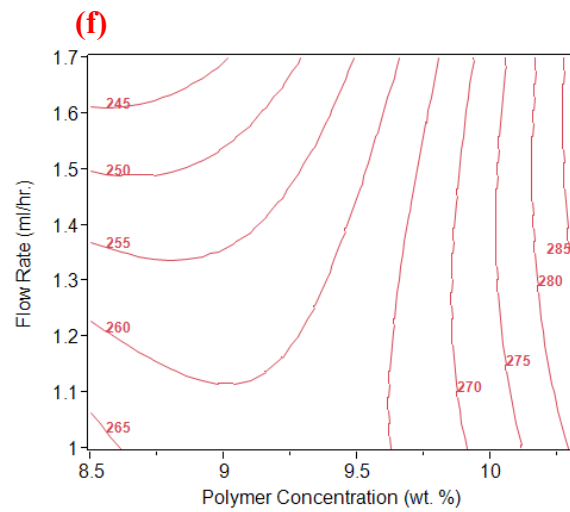
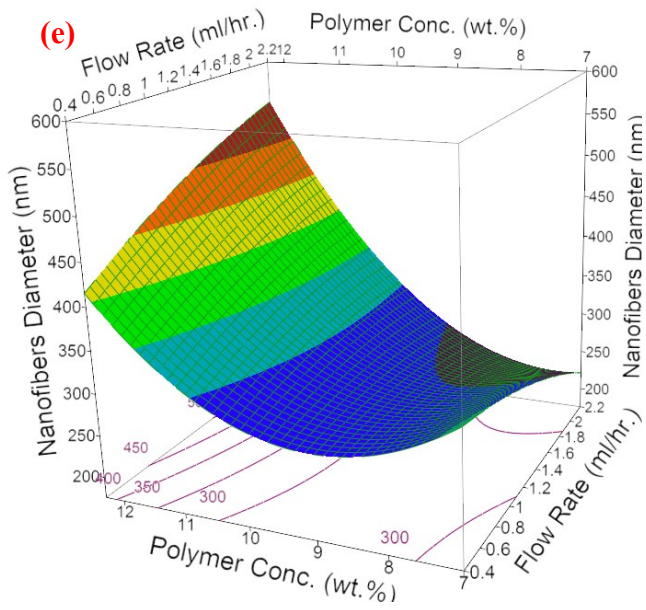
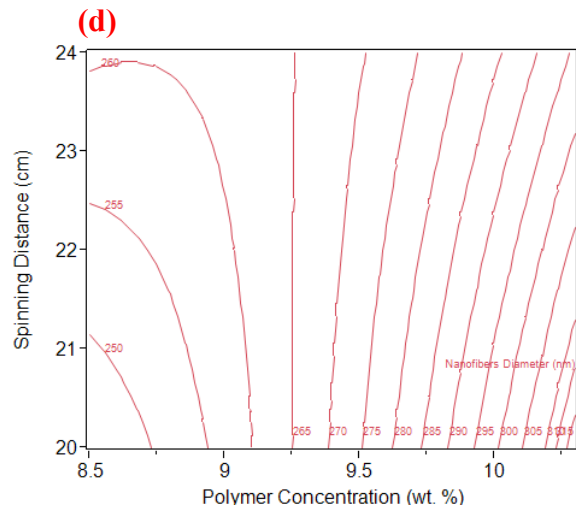
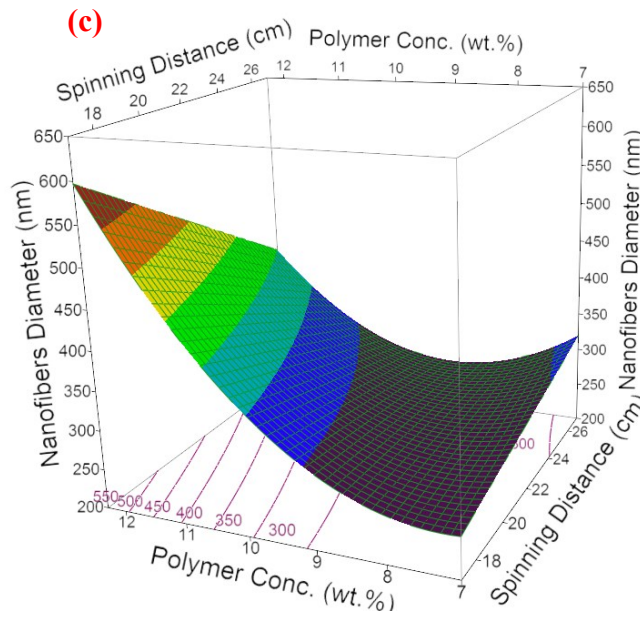
The three-dimensional (3D) response surfaces and two-dimensional (2D) contour plots of the cross-factor interaction effects between the model parameters are presented in Figure 3-4. The surface of the model parameters and interaction between two variables were presented while other parameters were kept constant. The cross-factor interaction effect between the applied voltage and spinning distance is shown in Figure 3-4a,b. It is observed that the nanofibers diameter is highly dependent on both applied voltage and spinning distance as diameter generally decreases with increasing applied voltage and spinning distance. However, an applied voltage above 23 kV has a larger influence than the spinning distance. The decrease in nanofibers diameter with increasing applied voltage and spinning distance could be attributable to the fact that an increase in the applied voltage enhances the electrostatic force on the solution, this usually causes the polymer jet to be stretched further thereby leading to the formation of thinner nanofibers [129], [162]. Furthermore, evaporation of solvent usually occurs after the polymer jet has been stretched into nanofibers and before deposition on the collector [139]. Thus, the optimum spinning distance is required for complete evaporation of the solvent before the nanofibers reach the collector. This will also result in more stretching of the nanofibers thereby reducing the diameter [139], [161]. Therefore, the combined effect of applied voltage and spinning distance at the optimum level results in the reduction of the diameter of the nanofibers.

Figure 3-4c,d depict the interaction between spinning distance and polymer concentration. It is observed that the cross-factor interaction between the predictors significantly affects the diameter of the nanofibers. The nanofiber diameter increases with increasing polymer concentration at low spinning distance. At high spinning distance, the diameter of the nanofibers initially decreases with increasing polymer concentration up to 9 wt %. Nonetheless, the nanofiber diameter increases with increasing spinning distance beyond 9 wt % polymer concentration. This trend could be attributable to the fact that the optimum distance required to stretch the nanofibers was attained at 9 wt % polymer concentration. Therefore, an increase in the spinning distance could not stretch the nanofibers further. Thus, the effect of polymer concentration becomes the dominant factor. This trend is in line with the results obtained by other authors [129], [163], [164]. Generally, a minimum solution concentration is required for the formation of nanofibers during the electrospinning process. The results of the investigation carried out by previous authors revealed that a mixture of beads and discontinuous nanofibers were obtained at low polymer concentration, and as the solution concentration increases, smooth and uniform nanofibers with increased diameter were obtained [163], [165].

Figure 3-4e,f show the cross-factor interaction between the polymer concentration and the flow. These figures show that the diameter of the nanofibers decreases with increasing flow rate at low polymer concentration. However, the effect of flow rate on the diameter of the nanofibers was reversed at high polymer concentration as the nanofiber diameter increases with increasing flow rate. As the flow rate increases at high polymer concentration, the influence of polymer concentration becomes dominant, and this causes an increase in the fiber diameter. Moreover, Figure 3-4g,h reveal the cross-factor interaction between spinning distance and concentration of NaCl. These figures show that the diameter of the nanofibers decreases with increasing spinning

distance at low NaCl concentration. Contrarily, the effect was opposite at high NaCl concentration as the nanofibers' diameter slightly decreases with increasing spinning distance. The combined effect of spinning distance and NaCl concentration at the optimum level results in a 24% reduction in nanofiber diameter. Finally, Figure 3-4i,j show the interaction between polymer concentration and concentration of NaCl. The figures reveal that interaction between the two variables has a significant effect on the diameter of the nanofibers. This diameter generally decreases with increasing NaCl concentration at high polymer concentration. However, the effect was inverted at low polymer concentration as the nanofiber diameter slightly increases with increasing NaCl concentration. Beachley and Wen [166] explained that the addition of salts to the polymer solution increases the conductivity and the surface charge density of the solution jet thereby resulting in the formation of beadless nanofibers with reduced diameter. In the current research, a 28% reduction in the nanofiber diameter was obtained by changing the NaCl concentration from 0.05 to 1.05 wt %. Furthermore, the addition of NaCl to the precursor solution also prevented the formation of beaded nanofibers. This trend is consistent with the results reported by other authors [165], [166].





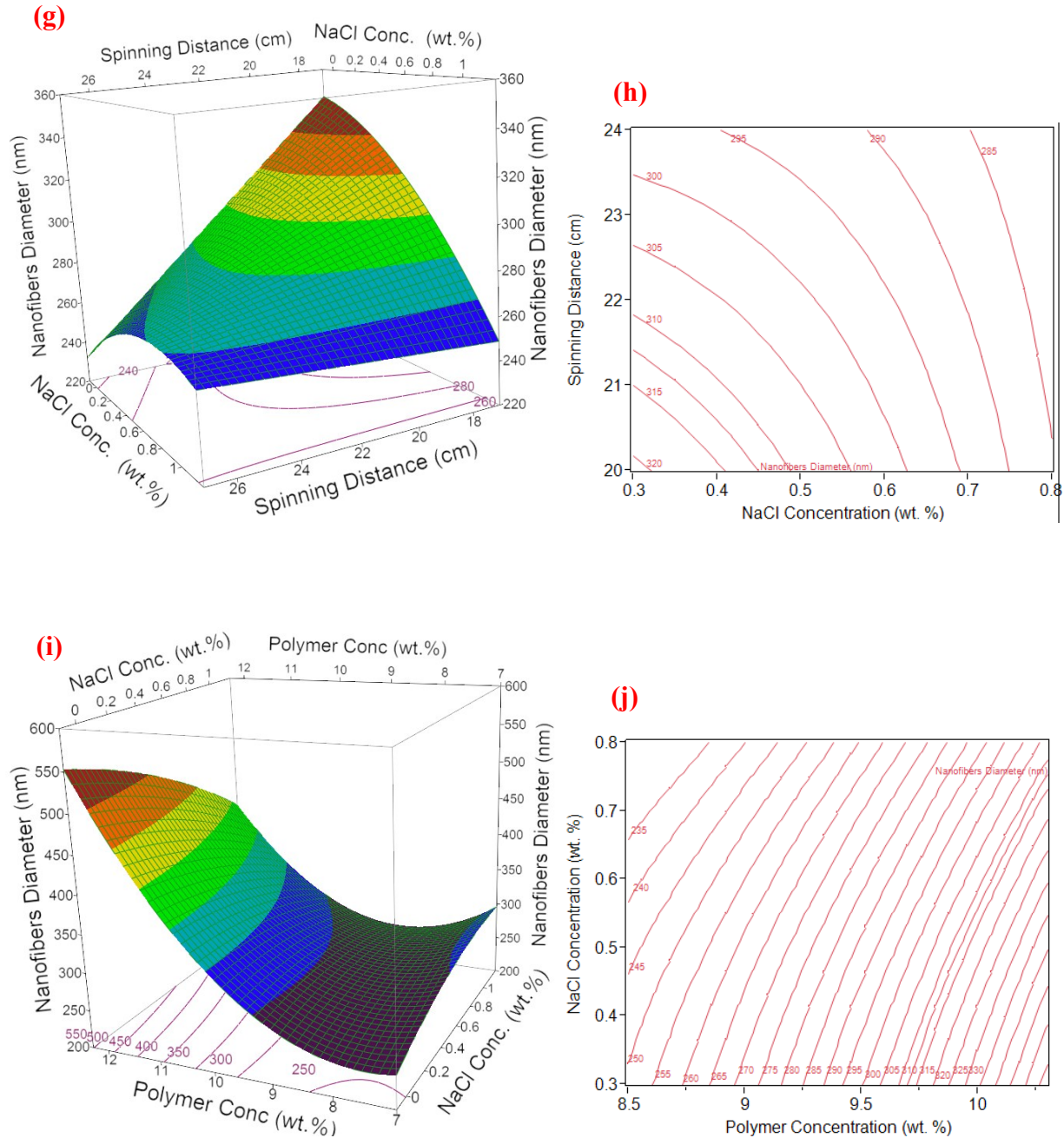


Figure 3-4: 3D response surface plots (a,c,e,g,i) and 2D contour plots (b,d,f,h,j) of interaction between the (a,b) applied voltage and spinning distance (VD); (c,d) spinning distance and polymer concentration (DP); (e,f) flow rate and polymer concentration (PF); (g,h) spinning distance and concentration of NaCl (DN); and (i,j) polymer concentration and concentration of NaCl (PN).

### 3.3.4. Optimization and validation of the response surface model

The optimum experimental conditions of the five variables; the applied voltage (V), spinning distance (D), polymer concentration (P), flow rate (F), and NaCl concentration (N) have been determined to meet the previously set goal of minimizing the diameter of the nanofibers. The maximum desirability function was achieved with nanofiber diameter of 226 nm under optimum conditions of 24 kV applied voltage, 20 cm spinning distance, 8.5 wt % polymer concentration, 1.7 ml h<sup>-1</sup>, flow rate, and 0.8 wt % NaCl concentration. The model has been validated by conducting another experiment using the obtained optimum conditions. The experimental result obtained under the optimum conditions is 233 nm, which is very close to the 226 nm predicted value. This further confirms the reliability of the developed model. It also implies that this method can be successfully employed for fabricating niobium-tungsten oxide nanofibers with controlled morphology and diameter for various applications.

Furthermore, the model was verified using the graphical representation of the experimental and predicted values of the diameter of the nanofibers shown in Figure 3-5. The values were also used to calculate the average model accuracy (AMA) using equation (2) [156], [167] where  $X_i$  is the experimental nanofibers diameter at the run (i),  $Y_i$  is the predicted nanofibers diameter at the run (i), and n is the total number of experimental runs.

$$AMA = \sum_{i=1}^n \frac{\left[1 - ABS \frac{(X_i - Y_i)}{X_i}\right]}{n} \times 100 \quad (3-2)$$

The result obtained from Equation (3-2) shows an average model accuracy of 98%, this is considered as an acceptable model [160], [161].

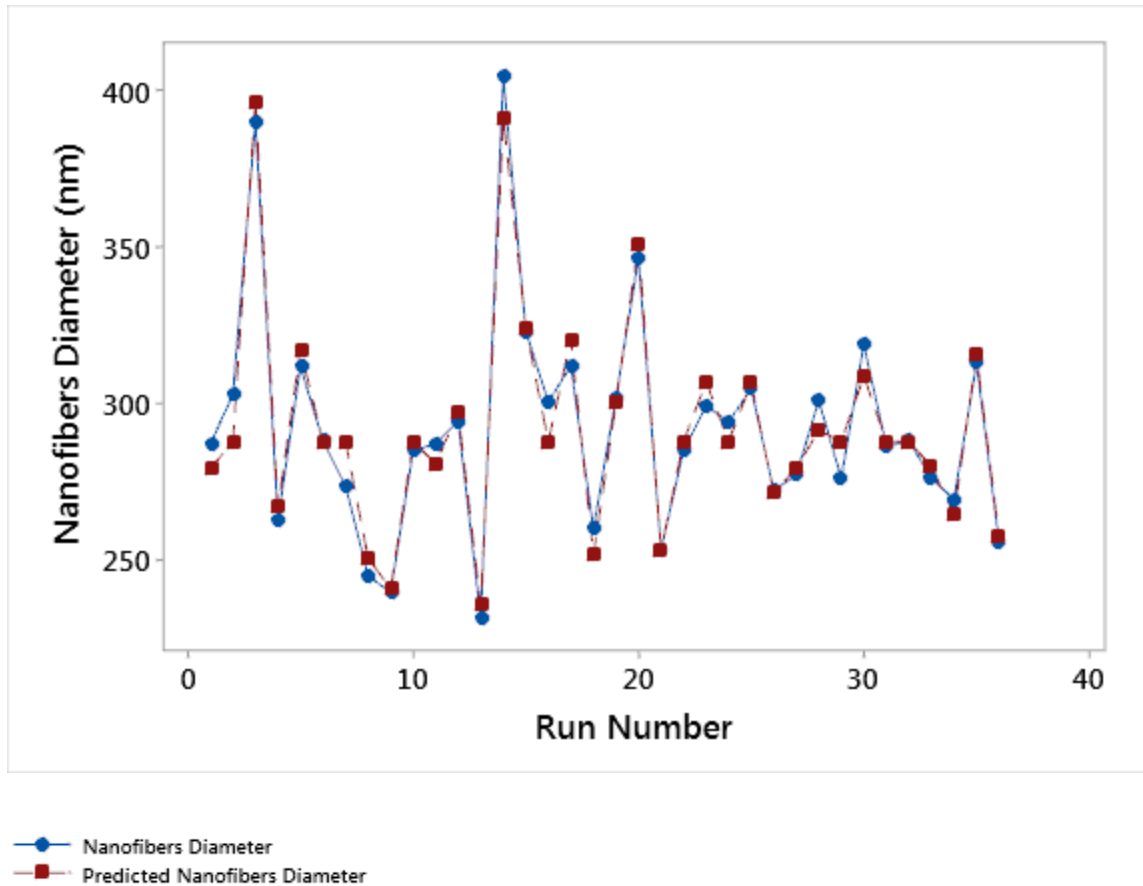


Figure 3-5: Model predicted nanofibers diameter in relation to the current experimental results

### 3.4. Conclusion

The influence of process parameters on the electrospinning of niobium-tungsten oxide nanofibers was investigated and optimized using the response surface method. The predictive model developed using RSM together with CCD was found to be accurate and reliable for representing the diameter of the nanofibers. The reliability of the predictive model was assessed using ANOVA and linear correlation coefficient. The determination coefficient ( $R^2$ ) and the adjusted  $R^2$  of 0.96 and 0.93 were obtained, with an average model accuracy of 98%. Furthermore, the result of the ANOVA test performed on the model indicates that the applied voltage (V), spinning distance (D), polymer concentration (P), NaCl concentration (N), and other cross factor interactions such as VD, DP, PF, PN, and  $P^2$  have a significant effect on the diameter

of the nanofibers. The CCD method was utilized to optimize the process parameters. Under the optimum conditions of the applied voltage (24 kV), spinning distance (20 cm), polymer concentration (8.5 wt.%), flow rate ( $1.7 \text{ ml hr}^{-1}$ ), and NaCl concentration (0.8 wt.%), experimental nanofibers of 233 nm were obtained. This is very close to the 226 nm diameter predicted by the model. Therefore, the proposed model is representative of the process and it could be employed as a base for future studies for the reduction of nanofiber diameter within the range of the factors used in the research. Furthermore, the approach presented in this study can be employed as a basis for fabricating uniform ceramic nanofibers for various applications. Nevertheless, it should be noted that the electrospinning of ceramic nanofibers is dependent on the choice of precursor salt and type of polymer. In terms of future work, it is suggested that the influence of other relevant working parameters on the electrospinning of niobium-tungsten oxide nanofibers are investigated using other approaches such as machine learning and artificial neural networks.

### Overview of chapter 3

Chapter three discusses the optimization of electrospinning process of  $\text{Nb}_{18}\text{W}_{16}\text{O}_{93}$  nanofibers. The same approach was also employed for optimizing the electrospinning process of  $\text{MoNb}_{12}\text{O}_{33}$  nanofibers, and the results are presented in appendix A. The results show that both  $\text{Nb}_{18}\text{W}_{16}\text{O}_{93}$  and  $\text{MoNb}_{12}\text{O}_{33}$  nanofibers exhibit similar characteristics.

The results obtained from optimizing the electrospinning process of  $\text{Nb}_{18}\text{W}_{16}\text{O}_{93}$  nanofibers were employed to select suitable parameters for fabricating  $\text{Nb}_{18}\text{W}_{16}\text{O}_{93}$  nanowires. The nanowires were doped with nickel to enhance their electrochemical kinetics and electronic conductivity. The next chapter focuses on the fabrication and assessment of the electrochemical activities of nickel doped  $\text{Nb}_{18}\text{W}_{16}\text{O}_{93}$  nanowires.

## Chapter 4: Nickel-doped Nb<sub>18</sub>W<sub>16</sub>O<sub>93</sub> nanowires with improved electrochemical properties for lithium-ion battery anodes

Babajide Oluwagbenga Fatile<sup>1</sup>, Martin Pugh<sup>1</sup>, Mamoun Medraj<sup>1</sup>

<sup>1</sup>Department of Mechanical, Industrial, and Aerospace Engineering, Concordia University, Montreal, Canada

This paper has been published in Materials Chemistry and Physics, doi:  
<https://doi.org/10.1016/j.matchemphys.2023.128179>

### Abstract

Recently, niobium tungsten oxide nanowires have been reported to be a promising anode material for lithium-ion batteries (LiBs). This material has demonstrated high theoretical capacity, significant structural stability, high power density, and environmental friendliness. Nonetheless, its low electronic conductivity is a significant drawback that needs to be addressed. More so, it is desirable to enhance its electrochemical performance to meet the needs of current energy applications. In this study, pristine and nickel-doped (Ni = 1 wt.%, 3 wt.%, 5 wt.%) niobium tungsten oxide nanowires were fabricated using the electrospinning technique, followed by annealing. The effect of nickel doping content on the morphology, structure, and electrochemical performance of niobium tungsten oxide nanowires was investigated. The XRD results show that the Ni doping expanded the unit cell and enhanced the lithium-ion diffusion in the Nb<sub>18</sub>W<sub>16</sub>O<sub>93</sub> nanowires. The electrochemical test results indicate that the 3 wt.% nickel-doped condition exhibits remarkable capacity retention of 93.1% over 500 cycles at a high current rate of 5 C. Furthermore, the Ni doping significantly enhanced the electronic conductivity compared to the pristine Nb<sub>18</sub>W<sub>16</sub>O<sub>93</sub> nanowires. The results obtained from the CV test also show that Ni doping lowered the polarization and increased the lithium-ion diffusion coefficient.

**Keywords:** Nb<sub>18</sub>W<sub>16</sub>O<sub>93</sub> nanowires, doping, nickel, lithium-ion batteries, anode

## 4.1 Introduction

Over the last few years, **LiBs** have been regarded as one of the most significant energy storage devices thanks to their low relative cost and lightweight. For these reasons, they have been extensively used for powering portable electronic devices, laptops, and electric vehicles [4], [168]. Typically, **LiBs** consist of three major parts: electrodes (anode and cathode), electrolytes, and separators [169]. The choice of electrode materials has been reported to significantly influence the quality and electrochemical performance of LiBs [169]. Thus, it is vital to select suitable electrode materials for LiBs. Presently, graphite is widely employed as an anode because it has demonstrated superior cycling stability and a high specific capacity compared to other potential anode materials [47]. Nevertheless, some limitations have been identified regarding the use of graphite as an anode material for LiBs [170]. For instance, Han *et al.* [171] reported that the Fermi energy ( $E_F$ ) of graphite is not perfectly matched to the lowest unoccupied molecular orbital (LUMO) of the electrolyte, and this usually induces the formation of a solid electrolyte film layer on the surface of the graphite anode; this could result in capacity degradation and low coulombic efficiency [3], [9]. This could further degenerate to the formation of hazardous lithium dendrites on the anode, which is a safety concern. These shortcomings have necessitated the quest for a new anode material with high cycling performance and high energy density while being environmentally friendly [172], [173].

Lately, titanium-based oxides have been proposed as an alternative anode material to address some of the shortcomings associated with graphite. Titanium-based oxides have a working voltage between 1.55 and 1.8 V [172], [173]. This prevents the formation of solid electrolyte interphase (SEI) and facilitates high-rate lithium intercalations when they are employed as an anode material. The investigation by Yao *et al.* [174] shows that  $\text{Li}_4\text{Ti}_5\text{O}_{12}$

nanosheets embedded in three-dimensional amorphous carbon exhibited a superior rate performance of 140 mAh g<sup>-1</sup> at 8 C (xC means that the battery was charged in x<sup>-1</sup> hours) after 700 cycles. Zhang *et al.* also reported that dual-phase Li<sub>4</sub>Ti<sub>5</sub>O<sub>12</sub>-TiO<sub>2</sub> delivered a high delithiation capacity of 105 mAh g<sup>-1</sup> and capacity retention of ~95% after 150 cycles at 5 C [175]. Nevertheless, the low theoretical capacity of titanium-based oxides still limits their practical application as anode materials [175]. To this end, niobium-tungsten oxides are another promising candidate currently being explored as potential anode materials for LiBs [6], [10], [49], [142], [146], [176], [177]. These materials have been reported to possess a relatively higher lithium-ion diffusion coefficient and initial specific capacity compared to titanium-based oxides. The lithium diffusion coefficients in Nb<sub>18</sub>W<sub>16</sub>O<sub>93</sub> ( $1.312 \times 10^{-13} \text{ m}^2 \text{ s}^{-1}$ ) [47] and W<sub>3</sub>Nb<sub>14</sub>O<sub>44</sub> ( $8.020 \times 10^{-13} \text{ m}^2 \text{ s}^{-1}$ ) [49] are much higher than Li<sub>4</sub>Ti<sub>5</sub>O<sub>12</sub> ( $3.270 \times 10^{-16} \text{ m}^2 \text{ s}^{-1}$ ) [178], and TiO<sub>2</sub> ( $2.200 \times 10^{-15} \text{ m}^2 \text{ s}^{-1}$ ) [179]. This implies that lithium diffuses faster in niobium tungsten oxides than in titanium-based oxides [3], [47]. In addition, niobium-tungsten oxides (NWO) have demonstrated significant theoretical capacity, structural integrity, high power density, and environmental friendliness owing to their unique crystal structure [47], [142], [180]. Nonetheless, their inherent poor electron transfer properties that inhibit the kinetics of electrochemical processes are significant drawbacks that need to be addressed [176], [181], [182]. In addition, it is desirable to enhance their electrochemical performance to meet the needs of the current energy applications. The current research is an attempt to overcome these drawbacks.

Several approaches have been used to enhance the conductivity and cycling performance of anode materials for LiBs; some include doping [54], [67], [183]–[186], annealing [41], [187], conductive coating [187], [188], and nanostructured strategy [47]. These approaches had been

judged to yield promising results. The use of nanostructured materials can improve the capacity and cycling life of LiBs due to their short lithium-ion insertion, large specific surface area in contact with an electrolyte, and high electrochemical activity [74]. Saritha *et al.* [146] also established that the rate at which a material can store lithium-ion depends on the structure, shape, morphology, and particle size. This has motivated many authors [33], [47], [49] to investigate the use of nano-sized materials for LiB applications. Ye *et al.* [47] investigated the reversible specific capacity of  $\text{Nb}_{18}\text{W}_{16}\text{O}_{93}$  in both bulk and nanowire structures; the results obtained show that the  $\text{Nb}_{18}\text{W}_{16}\text{O}_{93}$  nanowires demonstrate a higher reversible specific capacity of  $195 \text{ mAh g}^{-1}$ , in comparison with  $171 \text{ mAh g}^{-1}$  for the bulk material. Xia *et al.* [3] also demonstrate that the lithiation dynamics of  $\text{Nb}_{18}\text{W}_{16}\text{O}_{93}$  were significantly enhanced by reducing the size below 100 nm. Their investigations further suggest that the grain boundaries of  $\text{Nb}_{18}\text{W}_{16}\text{O}_{93}$  greatly influence its electrochemical performance. The use of carbon layer coating for enhancing the electronic conductivity, rate performance, and cycling stability of  $\text{Nb}_{18}\text{W}_{16}\text{O}_{93}$  was attempted by Liu *et al.* [10] They reported that the  $\text{Nb}_{18}\text{W}_{16}\text{O}_{93}/\text{C}$  anode demonstrates a good rate performance, delivering  $182.8 \text{ mAh g}^{-1}$  at a high rate of 5 C and retaining 81% of its initial capacity.

Nowadays, the use of metal ions as a dopant has been demonstrated to be a viable technique for enhancing the intrinsic conductivity and lithium ions diffusion coefficient of anode materials by modifying their lattice structure and bandgaps, thereby improving their rate performance and cycling stability [133]. For instance, Yang *et al.* [15] prepared  $\text{Cu}^{2+}/\text{Nb}^{5+}$  Co-doped  $\text{TiNb}_2\text{O}_7$ , and they reported that doping enhanced the Li-ion diffusion coefficient and electronic conductivity of the resulting material by 14.8 times and at least 220 times, respectively. Likewise, Bini *et al.* [13] found that the doping of  $\text{FeNb}_{11}\text{O}_{29}$  with V and Mn ions

greatly enhanced the niobate compounds' cycling stability and overall electrochemical performance. Cai *et al.* [54] also studied the combined effect of doping and conductive coating by preparing sulfur-codoped carbon-coated  $\text{Cu}_2\text{Nb}_{34}\text{O}_{87}$  nanowires ( $\text{Cu}_2\text{Nb}_{34}\text{O}_{87}/\text{NSC}$ ). They found that combining the two approaches improved the lithium-ion diffusion coefficient, rate capability, and electronic conductivity of  $\text{Cu}_2\text{Nb}_{34}\text{O}_{87}/\text{NSC}$ . These results further motivated us to employ a similar approach in our investigation.

In recent years, approaches such as thermal  $\text{NH}_3$  modification and carbon layer coating have been employed to enhance the electrochemical kinetics of niobium-tungsten oxide, and the results obtained from these investigations were promising [176]. However, the influence of metal ion doping on the electrochemical kinetics of niobium-tungsten oxide is still rare. Therefore, it remains a point of contention and requires a thorough investigation. This will be attempted in this paper. Nickel doping has been demonstrated to be an effective means of enhancing the electrochemical performance of anode materials. Opra *et al.* [186] established that nickel doping tremendously improved the electronic properties and rate capability of  $\text{TiO}_2$  nanobelts. Notably, the improved electrochemical kinetics was attributed to the introduction of *3d* energy levels within the band structure of the  $\text{TiO}_2$  nanobelts, which resulted in the creation of oxygen vacancies and narrowed its band gap.

Herein, we propose the combination of nanostructure and Ni doping strategies for improving the electron transfer properties and electrochemical kinetics of niobium-tungsten oxide nanowires. This synergetic effect can lead to a remarkable improvement in the electrochemical performance of niobium-tungsten oxide nanowires. In this work, Ni-doped niobium-tungsten oxide nanowires were successfully fabricated using the electrospinning technique, and the

influence of Ni doping on the morphology, structure, and electrochemical performance of the niobium-tungsten oxide nanowires was investigated.

## **4.2 Materials and Methods**

### **4.2.1. Materials preparation**

The  $\text{Nb}_{18}\text{W}_{16}\text{O}_{93}$  nanowires were fabricated using the electrospinning technique. First, the precursor solution was prepared by dissolving 0.93 mmol niobium oxalate (98%, Sigma Aldrich) and 0.068 mmol ammonium metatungstate hydrate (99.5%, Sigma Aldrich) in a mixture of 17 mL ethanol and 5 mL deionized water at room temperature under vigorous mechanical stirring for 12 h. Then, a weighed portion of nickel nitrate (99.5%, Fischer Scientific) was added to the solution while continuously stirring for 12 h to obtain a homogeneous solution of 1 wt.% nickel-doped precursor solution (denoted as NWO-Ni-1). This was followed by adding 2.1 g poly(vinyl pyrrolidone) (MW 1,300,000  $\text{g mol}^{-1}$ , 100% purity, Sigma Aldrich). The resulting mixture was agitated for 12 h to obtain a homogenous viscous precursor solution. The procedure was repeated for preparing the precursor solution for 3 wt.% and 5 wt.% nickel doped precursor solution (denoted as NWO-Ni-3 and NWO-Ni-5 respectively) and undoped without the use of nickel nitrate (denoted as NWO). The resulting precursor solution for each sample was transferred into a syringe which has a stainless steel needle. Electrospinning was performed using an aluminum foil collector situated 20 cm from the needle's tip. At the same time, a potential difference of 22 kV was applied to the precursor solution droplet at the tip of the needle, and a flow rate of 0.8  $\text{mL h}^{-1}$  was maintained throughout the process. The as-spun nanofibers obtained from the precursor solution were annealed in a box furnace at 900 °C for 6 h in air.

#### 4.2.2. Material characterization

The morphologies of as-spun and annealed NWO, NWO-Ni-1, NWO-Ni-3, and NWO-Ni-5 were studied by Scanning Electron Microscope (SEM) (HITACHI S-3400N) and Scanning Electron Microscope (Hitachi Regulus 8230) equipped with a Scanning Transmission Electron Microscopy (STEM) detector and energy dispersive X-ray spectrometer (EDX) detector for the elemental mapping analysis. The crystal structure was studied using X-ray diffraction (XRD, (PANAnalytical X'pert Pro X-ray diffractometer) equipped with a **CuK  $\alpha$**  radiation source ( $\lambda = 1.5406 \text{ \AA}$ ). The scanning range ( $2\theta$ ) from  $10^\circ$  to  $50^\circ$  was selected using a step width of  $0.02^\circ$ . X-ray photoelectron spectroscopy (XPS) analysis was conducted on an ESCALAB 250 XI X-ray photoelectron microprobe (Thermo Scientific K-Alpha) using an AlK  $\alpha$  source and a spot size of  $400 \text{ }\mu\text{m}$ .

#### 4.2.3. Electrochemical test

The electrochemical performance was measured using coin-type cells (CR2032). The working electrodes were fabricated using active material (NWO, NWO-Ni-1, NWO-Ni-3, and NWO-Ni-5), acetylene black, and a binder (polyvinylidene fluoride). Firstly, a certain amount of N-methyl-2-pyrrolidone was transferred into a porcelain mortar with 10 wt.% of polyvinylidene fluoride; the mixture was stirred until the binder dissolved completely. 10 wt.% of acetylene black and 80 wt.% of active material were weighed and transferred into the mixture in the mortar and mixed thoroughly to obtain a homogeneous slurry. The resulting slurry was cast uniformly onto a copper foil pretreated with acetone and dried in a vacuum oven at  $110^\circ \text{C}$  for 18 h, pressed on a hydraulic press at  $1250 \text{ kg cm}^{-2}$ , and then punched into disks to obtain working electrodes with a mass loading of active material of about  $1.0 \text{ mg cm}^{-2}$  (Figure S4-1). The coin cells were assembled in an argon-filled glove box with oxygen and moisture level below 0.01 ppm. The

lithium disk was used as a counter electrode and separated from the working electrode by Celgard polypropylene films. A mixture of  $1 \text{ mol L}^{-1} \text{ LiPF}_6$  in ethylene carbonate and dimethyl carbonate solvent (Sigma-Aldrich, Canada) in a volume ratio of 1:1 was employed as an electrolyte. Galvanostatic charge/discharge tests were performed on the coin cells at various current rates in a voltage range of 3.0 V to 1.0 V using a potentiostat (Corrtest CS 2350 Bipotentiostat). Cyclic voltammetry (CV) data was also obtained at a sweep rate of  $0.1 \text{ mV}\cdot\text{s}^{-1}$ , and electrochemical impedance (EIS) was measured under open-circuit voltage after ten initial CV cycles. All the electrochemical tests were performed at room temperature, and measurements were repeated to ensure the reproducibility of the results. A schematic illustration of the fabrication process of the nanowires is presented in Figure 4-1.

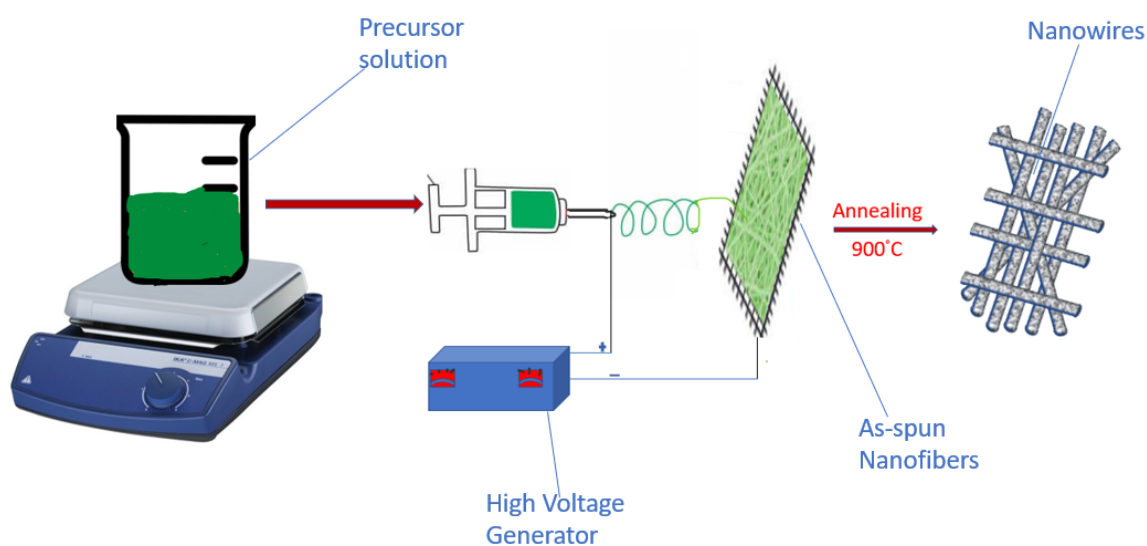


Figure 4-1: Schematic illustration of the fabrication process

### 4.3. Results and discussion

XRD of NWO, NWO-Ni-1, NWO-Ni-3, and NWO-Ni-5 are presented in Figure 4-2(a-b). All the diffraction peaks observed are indexed to the tetragonal tungsten bronze crystal structure (space group: Pbam) (JCPDS card No. 75- 0561). The reflections of other phases ( $\text{Nb}_2\text{O}_5$ ,  $\text{NiO}_2$ ,

and  $\text{WO}_3$ ) are not detected in NWO, NWO-Ni-1, and NWO-Ni-3 samples; this affirms that the nickel ions were successfully introduced into the crystal structure of  $\text{Nb}_{18}\text{W}_{16}\text{O}_{93}$ . However, an increase in the nickel content beyond 3 wt.% resulted in the formation of two new peaks in the XRD pattern of NWO-Ni-5, the peaks labeled with asterisks are located at  $2\theta$  of  $13.55^\circ$  and  $27.23^\circ$ , as shown in Figures 4-2a and S4-2a. This implies that the solubility limit of nickel in  $\text{Nb}_{18}\text{W}_{16}\text{O}_{93}$  is between 3 and 5 wt.%. The calculated XRD pattern of NWO based on its crystal structure data is also presented in Figure S4-2b. Furthermore, Figure 4-2b also show that peaks at (160), (290), and (001) shifted to lower angles as the nickel contents increased. This phenomenon was also observed at other peaks but was not as apparent. This indicates that the lattice parameters increase with increasing nickel content at the octahedral sites owing to the larger ionic radius of  $\text{Ni}^{2+}$  (0.69 Å) than that of  $\text{W}^{6+}$  (0.62 Å). Nevertheless, the effect of this on the crystallographic defects is perhaps more important as according to previous reports [67], [179], [186], such difference in the ionic radii is expected to result in lattice distortion, hence generating defects in nickel-doped conditions.

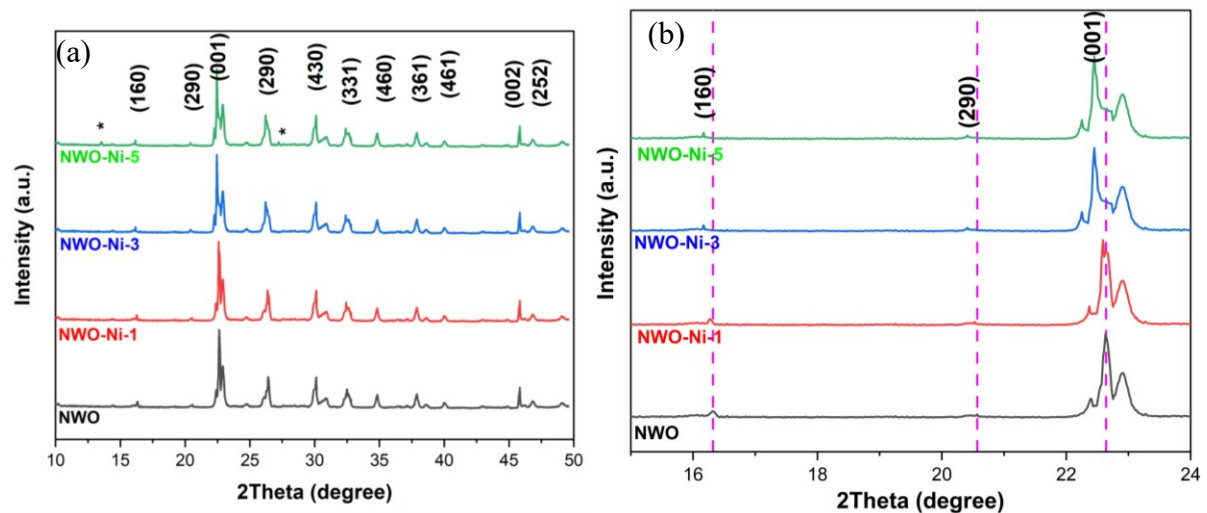


Figure 4-2: XRD patterns of (a) undoped and nickel-doped  $\text{Nb}_{18}\text{W}_{16}\text{O}_{93}$ , and (b) enlarged (160), (290), and (001) peaks

The lattice parameters and corresponding unit cell volumes were calculated, and the results are presented in Table S4-1. The unit cell volume also increases with increasing nickel content, reaching the highest value of 1780 Å<sup>3</sup> for NWO-Ni-3, which is about 1.14% larger than the undoped condition (NWO). The increase in unit cell volume is larger than the 0.31% and 0.35% reported for Cu<sub>0.02</sub>Ti<sub>0.94</sub>Nb<sub>2.04</sub>O<sub>7</sub> [15], and TiNb<sub>6</sub>O<sub>17</sub> [189]. The increase in unit cell volume along with the additional defects could enhance the interstitial diffusion of lithium ions, which could be beneficial for the improvement of their electrochemical performance. This is also supported by the results reported in [11], [189], [190].

The SEM and STEM images of NWO, NWO-Ni-1, NWO-Ni-3, and NWO-Ni-5 are unveiled in Figure 4-3 and Figure S4-3. The SEM images in Figure 4-3 (a-d) and Figure S4-3 (a,b) show that the undoped and the doped nanowires exhibited similar morphology. The NWO, NWO-Ni-1, NWO-Ni-3, and NWO-Ni-5 have an average nanofiber diameter of 277 nm, 253 nm, 246 nm, and 238 nm, respectively. After annealing, the diameter of the nanowires decreased, and the morphology changed from a smooth to a rough and porous surface, as shown in Figure 4-3 (e,k) and Figure S4-3 (c,d). The grains of the nanowires and the grain boundaries are clearly shown in Figure 4-3 (k) and Figure S4-3 (c). All these features are advantageous in terms of the electrochemical performance of anode materials for lithium-ion batteries. The EDS mappings presented in Figure 4-3 (f-j) clearly show that W, Nb, O, and Ni elements are evenly distributed in the NWO-Ni-5; the composition of NWO and NWO-Ni-5 obtained from EDS point analysis are also presented in Figure S4-3 (e-h). XPS analysis was performed on the undoped and nickel-doped samples to gain more insight into the chemical composition. The survey scan presented in Figures 4-4 (a,b) also confirms the presence of W, Nb, Ni, and O in the NWO-Ni-5 sample.

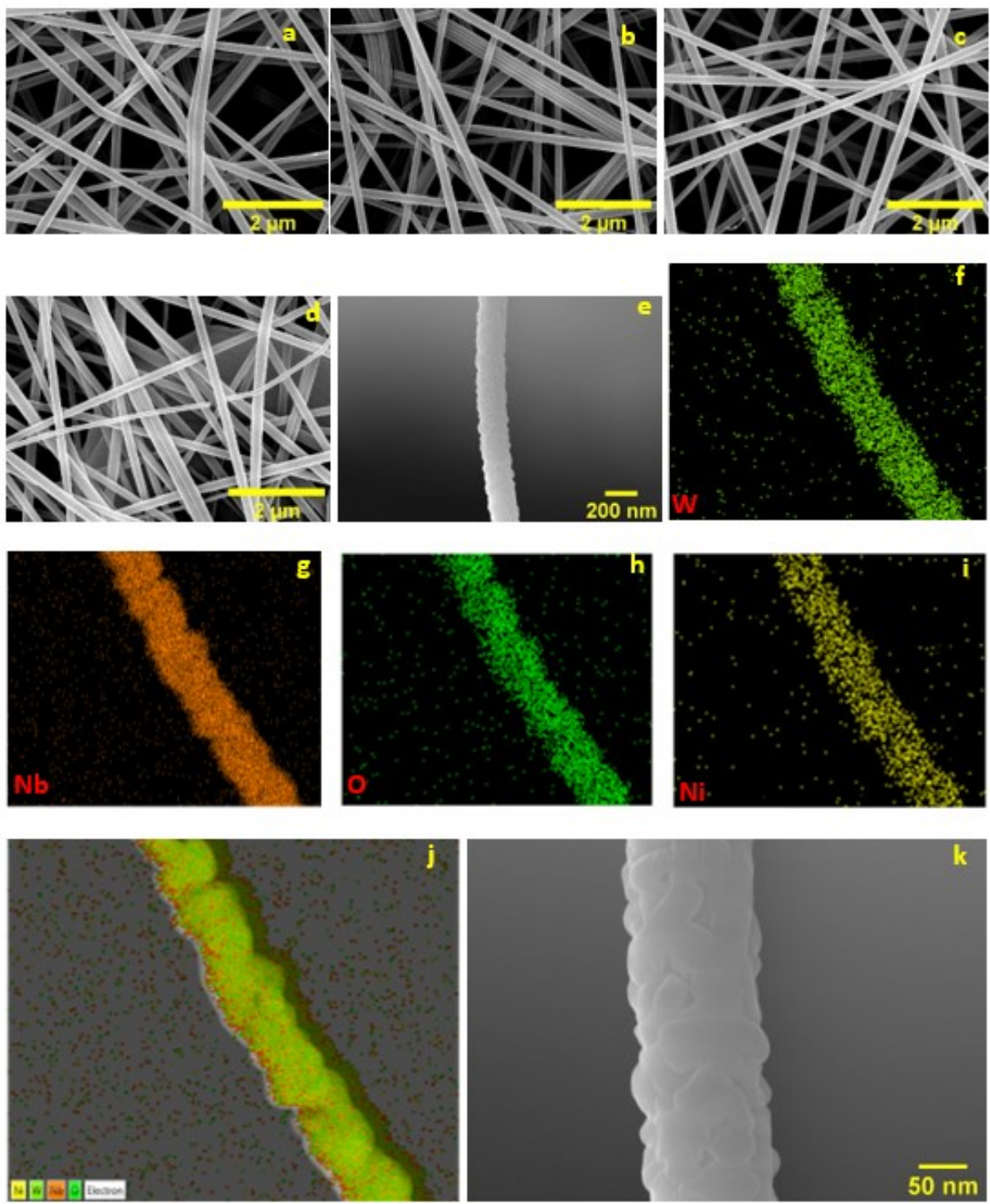


Figure 4-3: SEM images of as-spun (a) NWO, (b) NWO-Ni-1, (c) NWO-Ni-3, (d) NWO-Ni-3, (e) STEM image of NWO-Ni-5, (f-j) corresponding EDS elemental mapping images of Nb, W, O, Ni elements in NWO-Ni-5, and (k) STEM image of NWO

The sharp peak of carbon detected at 285.3 eV could have resulted from the adventitious contamination from the XPS instrument, as reported by other authors [179], [186]. Figure 4-4c shows the Nb 3d spectrum with two peaks localized at 207.4 eV and 210.2 eV corresponding to Nb 3d<sub>5/2</sub> and Nb 3d<sub>3/2</sub>. This confirms the presence of Nb<sup>5+</sup> in the NWO compound [10], [67]. The W 4f 5/2 and W 4f 7/2 peaks of W 4f spectrum (Figure 4-4d) are centered at 38.5 and 36.4 eV, respectively, indicating that tungsten was in +6 oxidation state in NWO [10]. Figure 4-4e shows the spectrum of Ni 2p<sub>3/2</sub> localized at 855.5 eV, indicating the +2 state of nickel in NWO-Ni-3 [179,186]. The signal at 530.8 eV (Figure 4-4 f) can be attributed to O 1s (Figure 4-4f) of O<sup>2-</sup> [186]. Interestingly, the binding energy of NWO-Ni-1, NWO-Ni-3, and NWO-Ni-5 shifted to a lower direction (Figure S4-4), this indicates that the nickel doping resulted in the formation of oxygen vacancy [41].

The electrochemical performance was assessed by CV tests, as presented in Figure S4-5 (a-d). The CV curves of all the samples clearly show a pair of sharp redox peaks at about 2.15/2.11, 2.15/2.11, 2.16/2.12, and 2.17/2.12 V for NWO, NWO-Ni-1, NWO-Ni-3, and NWO-Ni-5, respectively. This is attributable to the conversion of W<sup>6+</sup>/W<sup>5+</sup> during the Li<sup>+</sup> intercalation and deintercalation encountered in the Nb<sub>18</sub>W<sub>16</sub>O<sub>93</sub> compounds. Another pair of two broad peaks are observed around the low voltage region at about 1.63/1.71, 1.65/1.72, 1.67/1.74, and 1.67/1.75 V for NWO, NWO-Ni-1, NWO-Ni-3, and NWO-Ni-5, respectively. This could be ascribed to the reduction of Nb<sup>5+</sup> into Nb<sup>4+</sup>. All these observations agree with the previous results reported by various authors [3], [10], [47]. Interestingly, the NWO-Ni-1 and NWO-Ni-3 conditions exhibited the lowest polarization of 0.07 V between the cathodic and anodic peaks; this represents a significant improvement compared to the polarization of other niobium-tungsten

oxide compounds previously reported [3], [6], [10], [47], [49], [146], [176], [177], [191] as shown in Figure 4-5 (a).

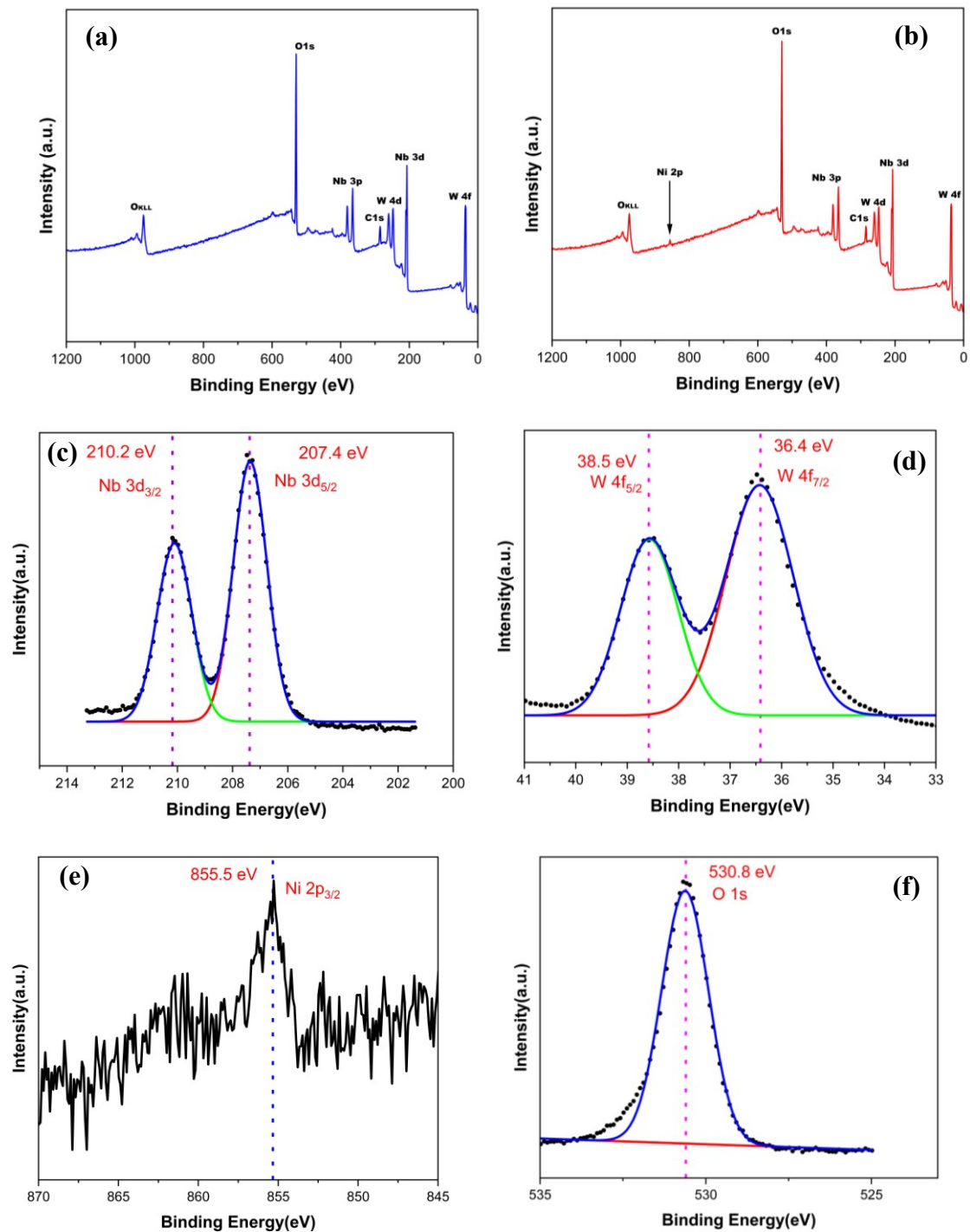


Figure 4-4: XPS survey scan of (a) NWO; (b) NWO-Ni-5, XPS spectra of (c) Nb 3d; (d) W 4f; (e) Ni 2p; and (f) O 1s

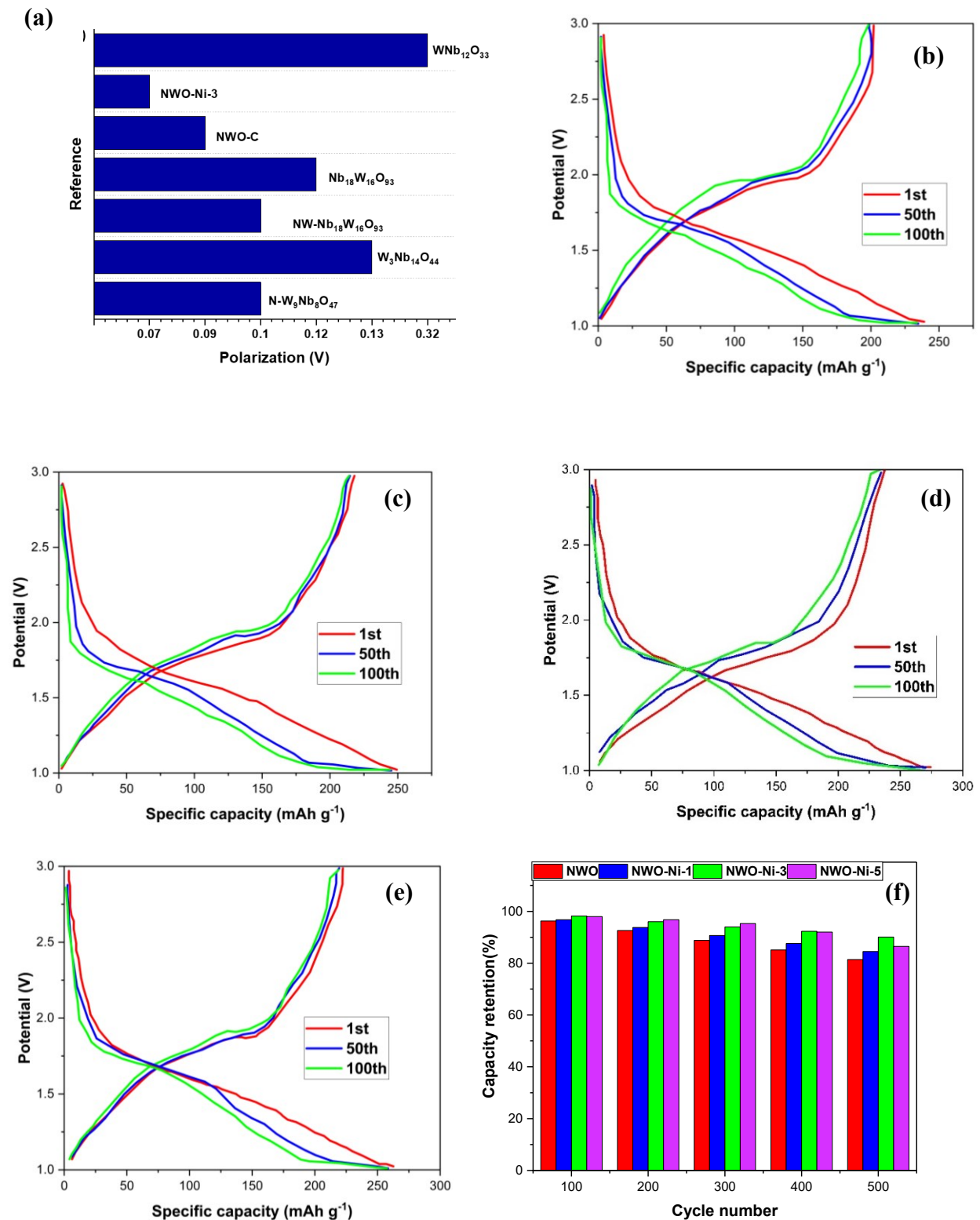


Figure 4-5: (a) comparison of cell polarization with previous works, charge/discharge profile at 0.2 C for (b) NWO, (c) NWO-Ni-1 (d) NWO-Ni-3, (e) NWO-Ni-5, (f) capacity retention at 5 C

This low polarization is associated with an increase in the electrical conductivity and electrochemical kinetics of electrode material [176]. Moreover, it is noticeable that the cathodic and the corresponding anodic peaks in NWO-Ni-1, NWO-Ni-3, and NWO-Ni-5 are higher than those in NWO, as shown in Figure S4-5 (a-d) and Figure S4-6. This implies that nickel doping improved their electrochemical activities [47].

Figure 4-5(b-e) depicts the galvanostatic charge and discharge (GCD) profiles of the electrodes at 0.2 C within the potential window of 1-3 V. It is observed that the GCD curves for all the electrodes exhibited a long and short plateau at around 1.72 V and 2.09 V, respectively. This agrees with the redox reactions of tungsten and niobium in the CV curves. A similar trend was also reported by other authors [47], [49], [146]. The initial discharge/charge capacities for NWO, NWO-Ni-1, NWO-Ni-3, and NWO-Ni-5 are  $239.0 \pm 10.3/202.1 \pm 11.6$ ,  $249.3 \pm 13.1/218.1 \pm 13.7$ ,  $274.1 \pm 10.8/ 237.4 \pm 10.1$ , and  $262.3 \pm 11.8/222.4 \pm 10.2$  mAh g<sup>-1</sup>, respectively, and the corresponding initial coulombic efficiencies are 84.5%, 87.5%, 86.6%, and 84.7%. It is evident that the nickel-doped electrodes exhibited superior specific capacity compared to the undoped condition. In addition, the specific capacity of the doped conditions exceeded 215.1 mAh g<sup>-1</sup> reported for the values reported for other niobium-based anodes in Figure S4-7 [6], [10], [47], [49], [142], [146], [176]. The GCD curves also show that the specific capacity faded slowly over the first 100 cycles; as shown in Figure 4-5(b-e), the discharge capacity after 100 cycles is  $233.8 \pm 10.6$ ,  $244.2 \pm 9.4$ ,  $269.7.0 \pm 11.3$ , and  $257.5 \pm 10.9$  mAh g<sup>-1</sup> for NWO, NWO-Ni-1 NWO-Ni-3, and NWO-Ni-5, respectively. The NWO-Ni-3 exhibited the lowest specific capacity loss of 1.6% over the first 100 cycles compared to 2.2%, 2.0%, and 1.8% exhibited by NWO, NWO-Ni-1, and NWO-Ni-5, respectively. The long-term cycling stability of the electrodes and their corresponding coulombic efficiency is evaluated by GCD at 5

C over the voltage range of 1 V to 3 V, and the corresponding capacity retention rate is presented in Figure 4-5(f). NWO, NWO-Ni-1, NWO-Ni-3, and NWO-Ni-5 show higher initial capacity of  $159.8 \pm 9.5$ ,  $172.7 \pm 9.1$ ,  $184.2 \pm 11.4$ , and  $179.4 \pm 9.8$  mAh g<sup>-1</sup>, respectively as shown in Figure 4-6(a). During the process of cycling, the specific capacity slightly decreases progressively to respectively reach  $138.3 \pm 9.4$ ,  $157.1 \pm 11.1$ ,  $171.5 \pm 8.7$ , and  $165.6 \pm 10.6$  mAh g<sup>-1</sup> after 500 cycles; this corresponds to an average capacity decay of about 0.0270%, 0.0180%, 0.0138%, and 0.0154% per cycle for NWO, NWO-Ni-1, NWO-Ni-3, and NWO-Ni-5. It is quite obvious that all the nickel-doped electrodes show excellent cycling stability performance compared with the undoped condition. The NWO-Ni-3 exhibited superior cycling stability and capacity retention among the nickel-doped conditions. It is also worth mentioning that the coulombic efficiency of NWO-Ni-3 and NWO-Ni-5 is almost 99% compared to 97% and 98% reported for NWO and NWO-Ni-1 respectively at the end of the 500 cycles (Figure S4-8). This remarkable performance affirms that nickel doping significantly enhanced cycling performance. The rate performance was evaluated by increasing the current density from 0.5 C, 1 C, 2 C, 5 C, 10 C, and finally recovered at 0.5 C, as depicted in Figure 4-6(b). It is observed that the specific capacity descends gradually with increasing current density. Nonetheless, the nickel-doped electrodes exhibited much less capacity loss compared to the undoped sample. At 1, 2, 5, and 10 C, the specific capacity of NWO significantly decreased, respectively, to 195.2, 181.4, 159.8, and 135.7 mAh g<sup>-1</sup>. Even at a high current rate of 10 C, the NWO-Ni-1, NWO-Ni-3, and NWO-Ni-5 still deliver higher reversible capacities of 148.7, 162.1, and 158.6 mAh g<sup>-1</sup> compared to the pristine condition with a capacity of 134.3 mAh g<sup>-1</sup>. The specific capacity nearly ascended to the initial values when the current rate returned to 0.5 C, as shown in Figure 4-6(b). This result confirmed that NWO-Ni-3 exhibited the best rate performance among other nickel-doped electrodes.

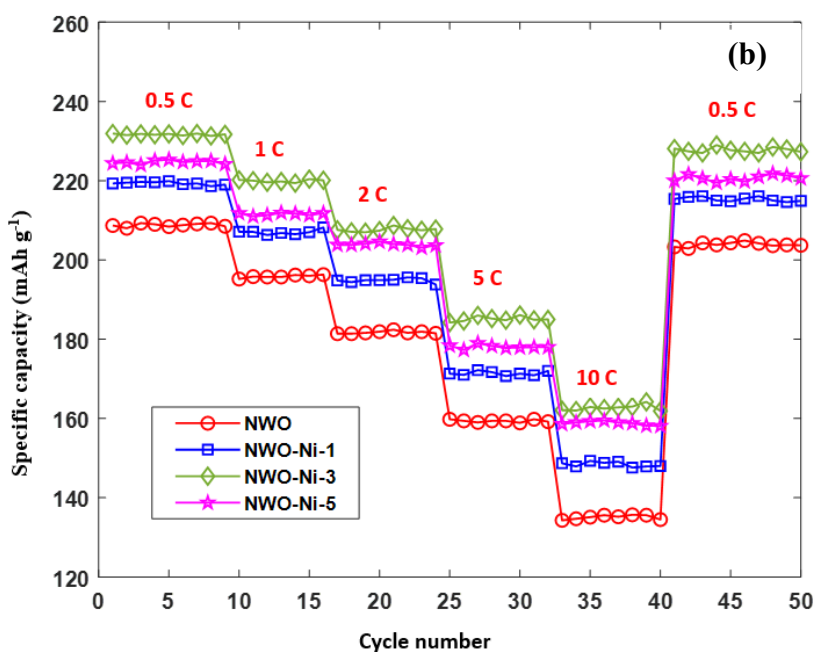
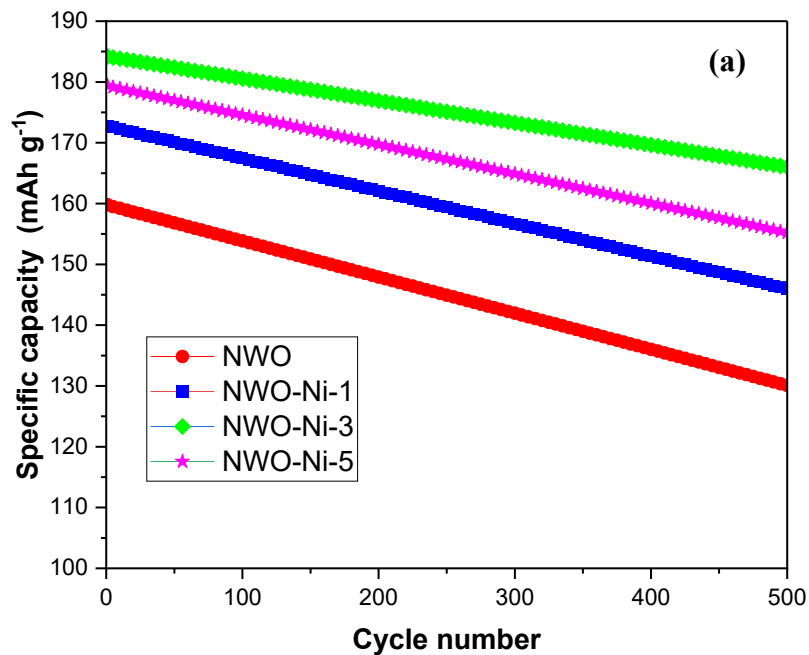


Figure 4-6: (a) Long-term cycling performance at 5 C, (b) rate capabilities of NWO, NWO-Ni-1, NWO-Ni-3, and NWO-Ni-5.

The results obtained in this work are consistent with Kang *et al.* [179] and Opra *et al.* [186], who studied the effect of Ni doping on the electrochemical performance of TiO<sub>2</sub> nanomaterial. The electrochemical performance of the anode materials in this work is also

compared to that of previously reported anode materials [6]–[8], [10], [12], [41], [50], [67], [176], [188], [192], [193] in Table S4-2.

The electrochemical kinetics were probed further by CV tests at various scan rates from 0.1 to 2 mV s<sup>-1</sup>, as depicted in Figure 4-7(a-b) and Figure S4-9(a-b). The NWO, NWO-Ni-1, NWO-Ni-3, and NWO-Ni-5 electrodes were prepared using the same loading mass of active materials for better comparison. During cycling, the cathodic and anodic peaks move respectively to the lower and higher potentials.

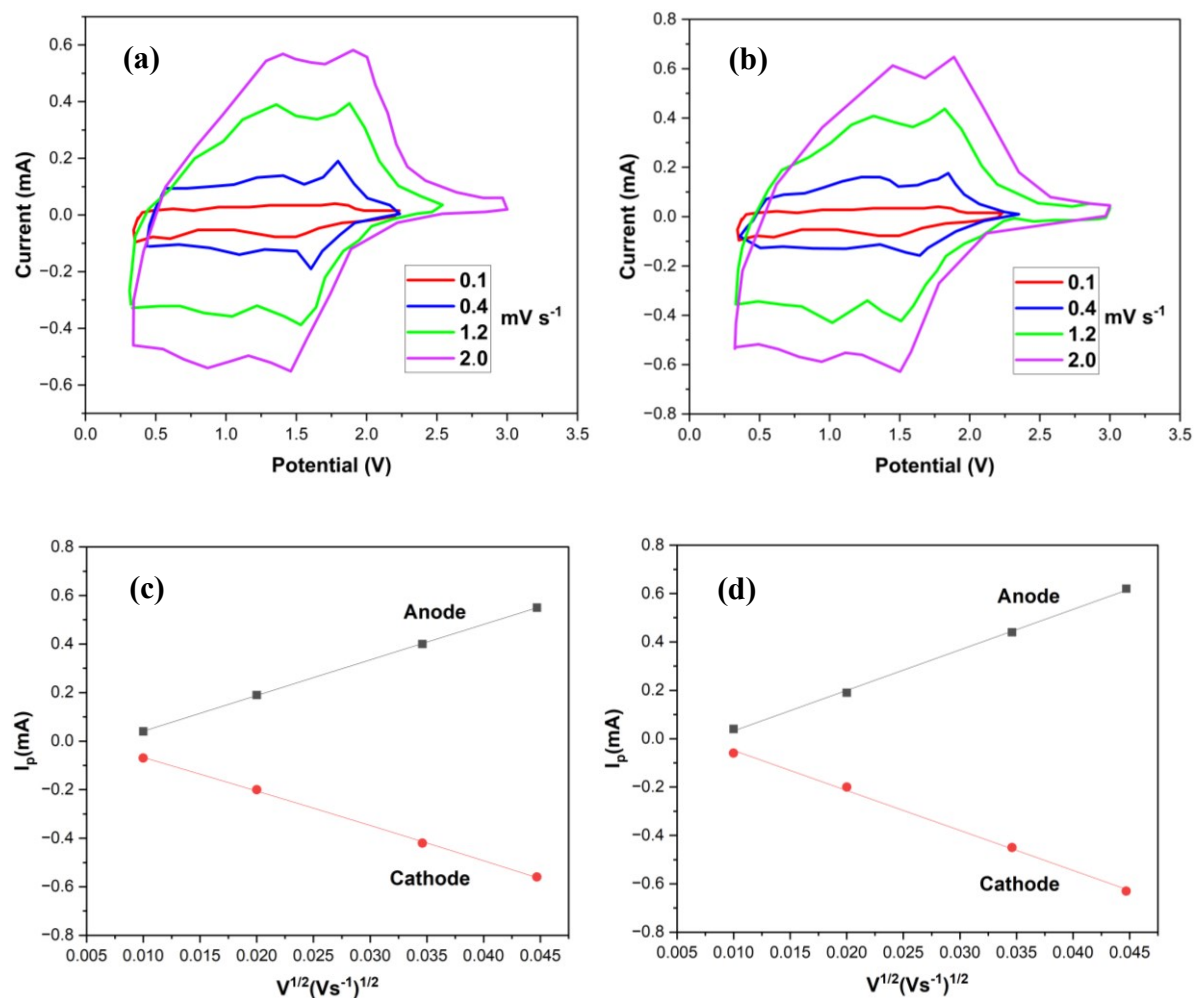


Figure 4-7: (a,b) CV curves of NWO and NWO-Ni-3 at different scan rates, (c,d) relationships between peak current and the square root of the scan rate of NWO and NWO-Ni-3

It is noteworthy that all the samples exhibited comparable anodic and cathodic slopes; this affirms that the electrochemical reactions were reversible [67]. The relationship between peak current ( $I_p$ ) and scan rate ( $V$ ) is linear, as shown in Figure 4-7(c-d) and Figure S4-9(c-d); this indicates that the lithium-ion diffusion coefficient ( $D_{Li}$ ) can be computed using the Randles-Sevcik equation [67], [75] as follows (symbols and definitions are provided in the supporting information):

$$I_p = 269000n^{3/2}AD^{1/2}Cv^{1/2} \quad (4-1)$$

The  $D_{Li}$  of NWO, NWO-Ni-1, NWO-Ni-3, and NWO-Ni-5 are estimated, and the results are presented in Table S4-3. The results show that the  $D_{Li}$  increases as the nickel content increases up to 3 wt.%. Nonetheless, a slight decrease in  $D_{Li}$  is observed for NWO-Ni-5 compared to NWO-Ni-3. This could be attributable to the larger unit cell volume of NWO-Ni-3, as shown in Table S4-1. The enlarged unit cell volume and lattice parameters have been reported to significantly enhance the lithium-ion diffusion coefficients [7], [194]. The results of  $D_{Li}$  diffusion coefficients reported for other niobate-based anode materials [3], [47], [49], [75], [176], [191]–[196] are summarized in Table S4-4 for comparison.

Electrochemical impedance spectroscopy (EIS) was performed to gain more insight into the electrochemical kinetics and electronic conductivity of the current nanowires. The Nyquist plots in Figure 4-8(a) have a semicircle arc in the high-frequency zone and a single straight line in the low-frequency region; these correspond to the charge transfer resistance and Warburg diffusion process, respectively [10], [180], [196]. The charge transfer resistances ( $R_{ct}$ ) obtained from the fitted model circuit depicted in the inset to Figure 4-8a shows that NWO-Ni-3 exhibits the smallest charge  $R_{ct}$  of 68.3  $\Omega$ , compared to NWO (190.7  $\Omega$ ), NWO-Ni-1 (134.6  $\Omega$ ), and NWO-Ni-5 (84.2  $\Omega$ ). The smaller  $R_{ct}$  is beneficial for improving the electronic conductivity and

electrochemical kinetics of anode materials, according to [180], [192], [197]. It was previously reported by Opra *et al.* [186] and Yan *et al.* [198] that nickel doping could induce *3d* energy levels within the band structure of its host material, thereby improving its electronic conductivity. Hence, nickel-doping is presumably the source of the noticeable improvement in the electronic conductivity in NWO-Ni-1, NWO-Ni-3, and NWO-Ni-5 electrodes observed in this work. The results from the EIS analysis agree with the degree of polarization obtained from the CV curves. Furthermore, the lithium-ion diffusion coefficient was calculated using relationships between  $Z'$  and  $\omega^{-1/2}$  in the low-frequency region [33], as shown in Figure 4-8(b). A steep slope in the low-frequency region of Nyquist plots is generally associated with fast diffusion coefficient. However, this is not always the case as it is a qualitative approach. Therefore, the lithium-ion diffusion coefficient was calculated using the equations (2) (symbols and definitions are in the supporting information) [197]. It is important to note that different versions of this equation have been used in the literature some of which are not correct as they use the factor of 2 in the denominator. Jafta *et al.* [197] in fact derived this equation and their analysis is found accurate unlike many other recent papers [67], [186], [191] who used a wrong equation.

$$D = \frac{2R^2T^2}{A^2n^4F^4C^2\sigma^2} \quad (4-2)$$

The results of the  $D_{Li}$  and fitted parameters are listed in Table S4-5. They support the  $D_{Li}$  results obtained from the CV curves, this shows that the steep slope in NWO (Figure 4-8b and b) did not result in better lithium-ion diffusion coefficient. These results confirm that nickel doping significantly improved the electronic conductivity, lithium-ion diffusion coefficient, and electrochemical kinetics of  $Nb_{18}W_{16}O_{93}$ . According to the previous works reported in [15], [186], [189], [199], a 0.25% to 4% increase in unit cell volume was reported to significantly enhance

the  $D_{Li}$  by several orders of magnitude. In this work, an increase of 1.14% in the unit cell volume for NWO-Ni-3 is observed which is within the range reported in [15], [186], [189], [199] for other materials. Hence and as discussed above, the significant improvement in lithium-ion mobility observed for the nickel-doped electrodes could be attributable to the nickel doping.

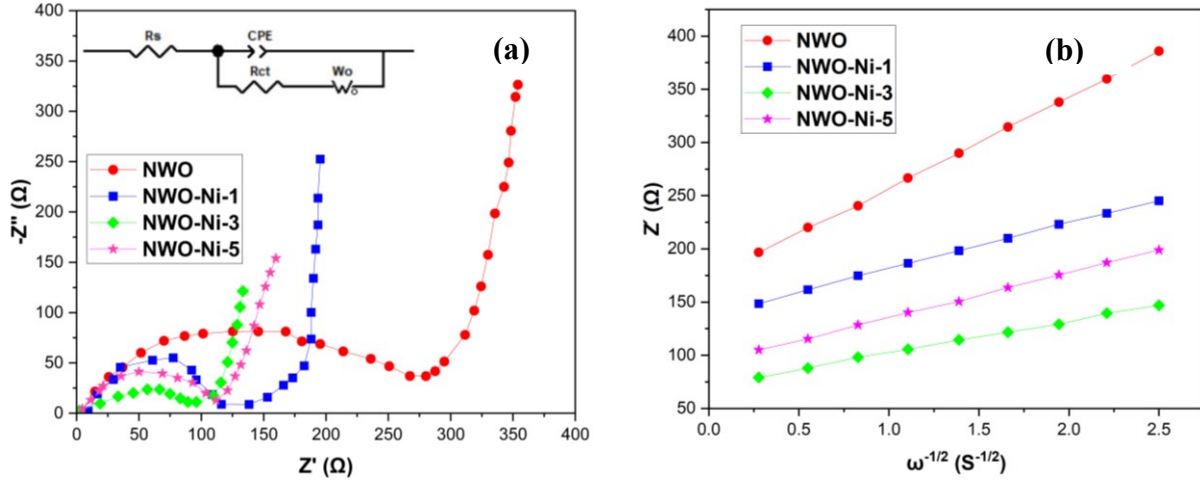


Figure 4-8: (a) Nyquist plots of NWO, NWO-Ni-1, NWO-Ni-3, and NWO-Ni-5; (b) the corresponding relationship between  $Z'$  and  $\omega^{-1/2}$  in the low-frequency region.

### 4.3. Conclusion

We have successfully fabricated  $Nb_{18}W_{16}O_{93}$  nanowires doped with 1, 3, and 5 wt.% nickel for the first time using the electrospinning technique. XRD analysis showed that the unit cell volume of  $Nb_{18}W_{16}O_{93}$  increased, confirming that  $Ni^{2+}$  ions were successfully incorporated into the crystal structure. The solubility limit of nickel in  $Nb_{18}W_{16}O_{93}$  was reached between 3 wt.% and 5 wt.%, resulting in the formation of a secondary phase when doping with 5 wt.% nickel. CV analysis showed that incorporating nickel into the structure of  $Nb_{18}W_{16}O_{93}$  nanowires reduced polarization and increased the lithium-ion diffusion coefficients. The galvanostatic charge/discharge test results showed that all the nickel-doped electrodes exhibited improved initial discharge/charge capacity, when compared to the pristine sample. The 3 wt.% nickel-

doped condition demonstrated a superior initial discharge/charge capacity of 274.1/237.4 compared to 239/202.1 mAh g<sup>-1</sup> obtained from the pristine condition at 0.2 C. When the electrode samples were cycled at a high current rate of 5 C, the nickel-doped samples retained a higher percentage of their initial capacities after 500 cycles; the corresponding capacity retention for pristine, 1 wt.%, 3 wt.%, and 5 wt.% nickel-doped samples are 81.4%, 84.6%, 90%, and 86.5%. Moreover, nickel doping significantly improved the rate performance of Nb<sub>18</sub>W<sub>16</sub>O<sub>93</sub> nanowires. The EIS results further demonstrate that the nickel-doped samples exhibit superior electronic conductivity and lithium-ion diffusion coefficients. The primary determinants of the remarkable improvement in electrochemical performance, lithium-ion diffusion coefficient, and electronic conductivity of the nickel-doped samples were attributed to ; (i) the generation of defects as a result of lattice distortion and the introduction of *3d* energy levels within the band structure of the Nb<sub>18</sub>W<sub>16</sub>O<sub>93</sub> nanowires by nickel, (ii) the expansion of the unit cell, and (iii) the enhanced crystal lattice stability of Nb<sub>18</sub>W<sub>16</sub>O<sub>93</sub> nanowires against the insertion and extraction of lithium ions. Therefore, this study demonstrates that nickel-doped Nb<sub>18</sub>W<sub>16</sub>O<sub>93</sub> nanowires have great potential as a promising anode material for lithium-ion batteries.

#### 4.4. Supporting Information

### Nickel-doped $\text{Nb}_{18}\text{W}_{16}\text{O}_{93}$ nanowires with improved electrochemical properties for lithium-ion batteries anode

#### Symbol definitions for equations (1)

$I_p$  = peak current

$n$  = electron molecule concentration in the redox reactions

$A$  = surface area of the electrode

$C$  = bulk concentration of lithium ions

$v$  = the scan rate

$D$  = diffusion coefficient of lithium ions

#### Symbol definitions for equations (2)

$R$  = gas constant

$T$  = absolute temperature

$\sigma$  = Warburg factor

$A$  = surface area of the electrode

$n$  = electron molecule concentration in the redox reactions

$F$  = Faraday constant

$C$  = concentration of lithium ions



Figure S4-1: Punched electrode disks.

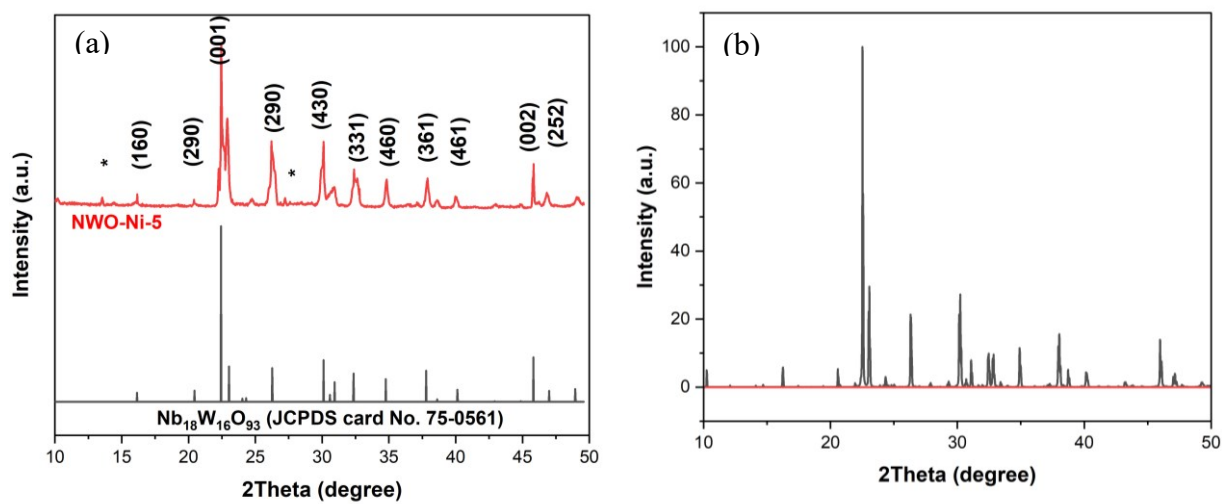
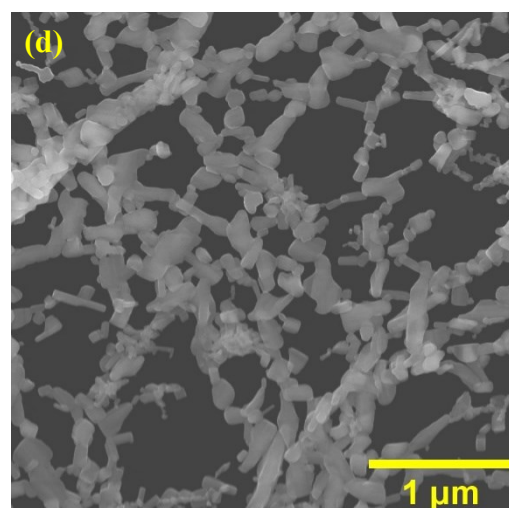
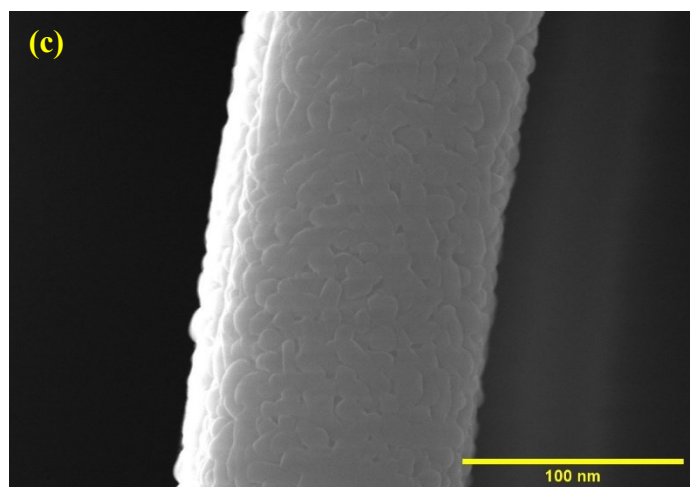
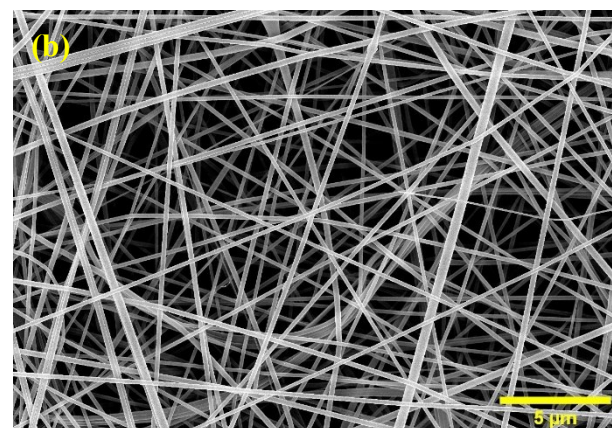
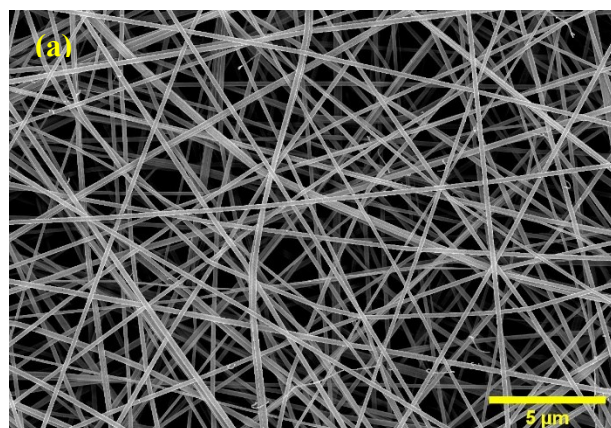


Figure S4-2: (a) XRD patterns of NWO-Ni-5, (b) Calculated XRD pattern of NWO

Table S4-1: Unit cell parameters of pristine and nickel-doped  $\text{Nb}_{18}\text{W}_{16}\text{O}_{93}$ .

Samples	$a$ (Å)	$b$ (Å)	$c$ (Å)	$V$ (Å <sup>3</sup> )
NWO	12.2171	36.5244	3.9442	1760
NWO-Ni-1	12.2254	36.5858	3.9467	1765
NWO-Ni-3	12.2482	36.7960	3.9487	1780
NWO-Ni-5	12.2450	36.8000	3.9446	1777



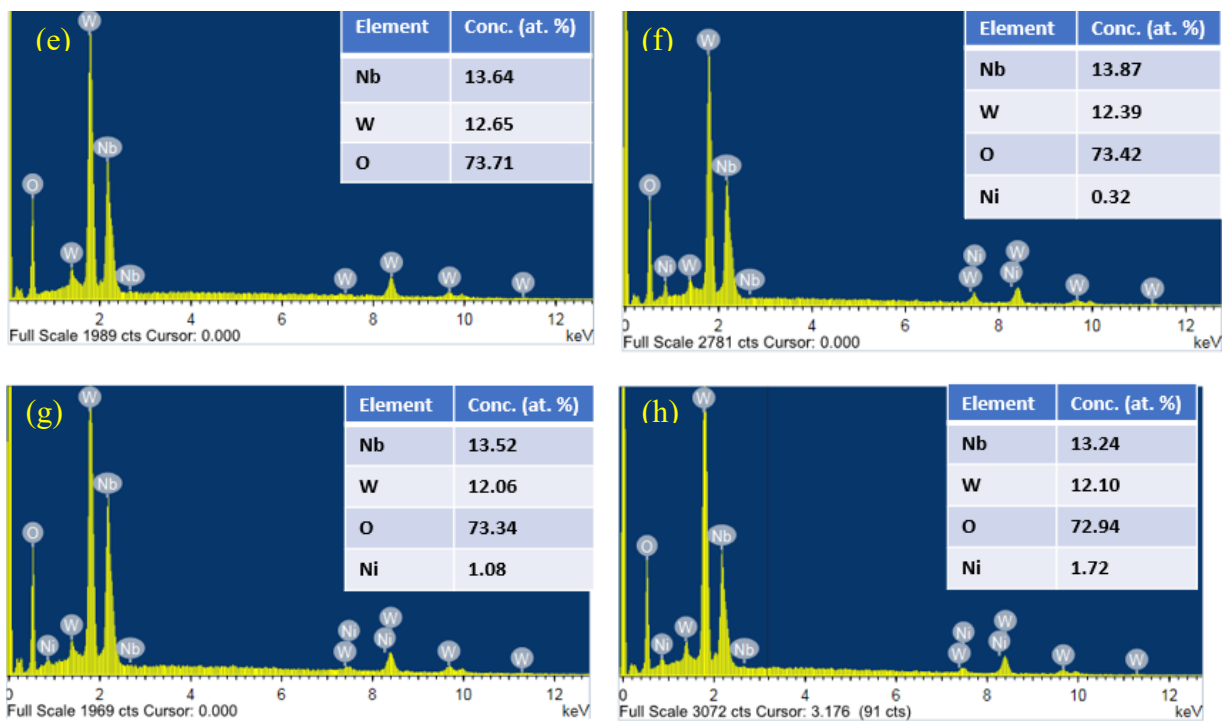


Figure S4-3: SEM images of (a) NWO, (b) NWO-Ni-5, STEM images of (c,d) NWO after annealing, EDS profile of (e) NWO, (f) NWO-Ni-1, (g) NWO-Ni-3, and (h) NWO-Ni-5

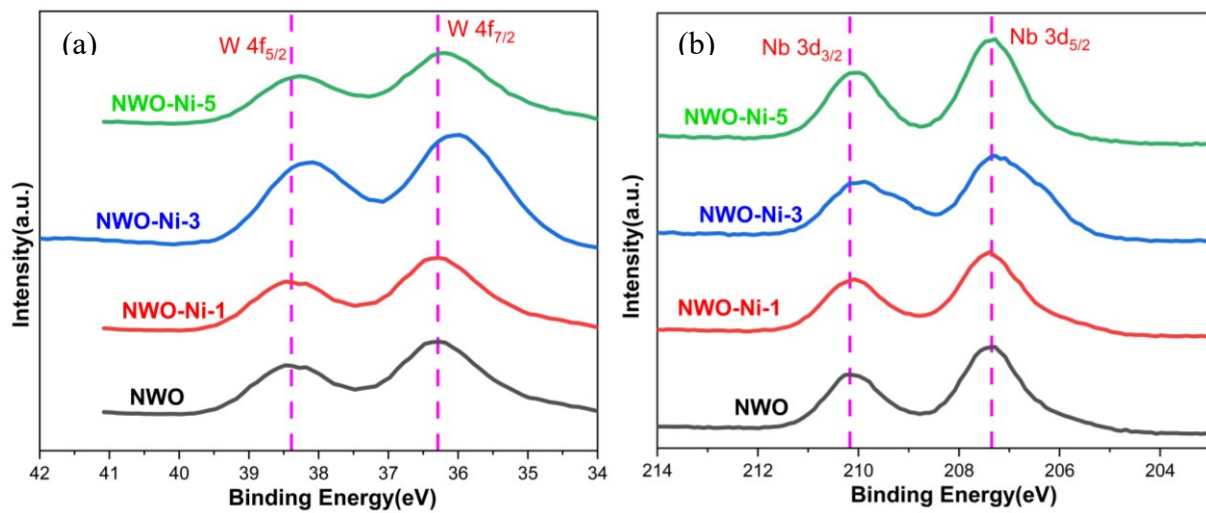


Figure S4-4: XPS spectra of NWO, NWO-Ni-1, NWO-Ni-3, and NWO-Ni-5 (a) W 4f; and (b) Nb 3d

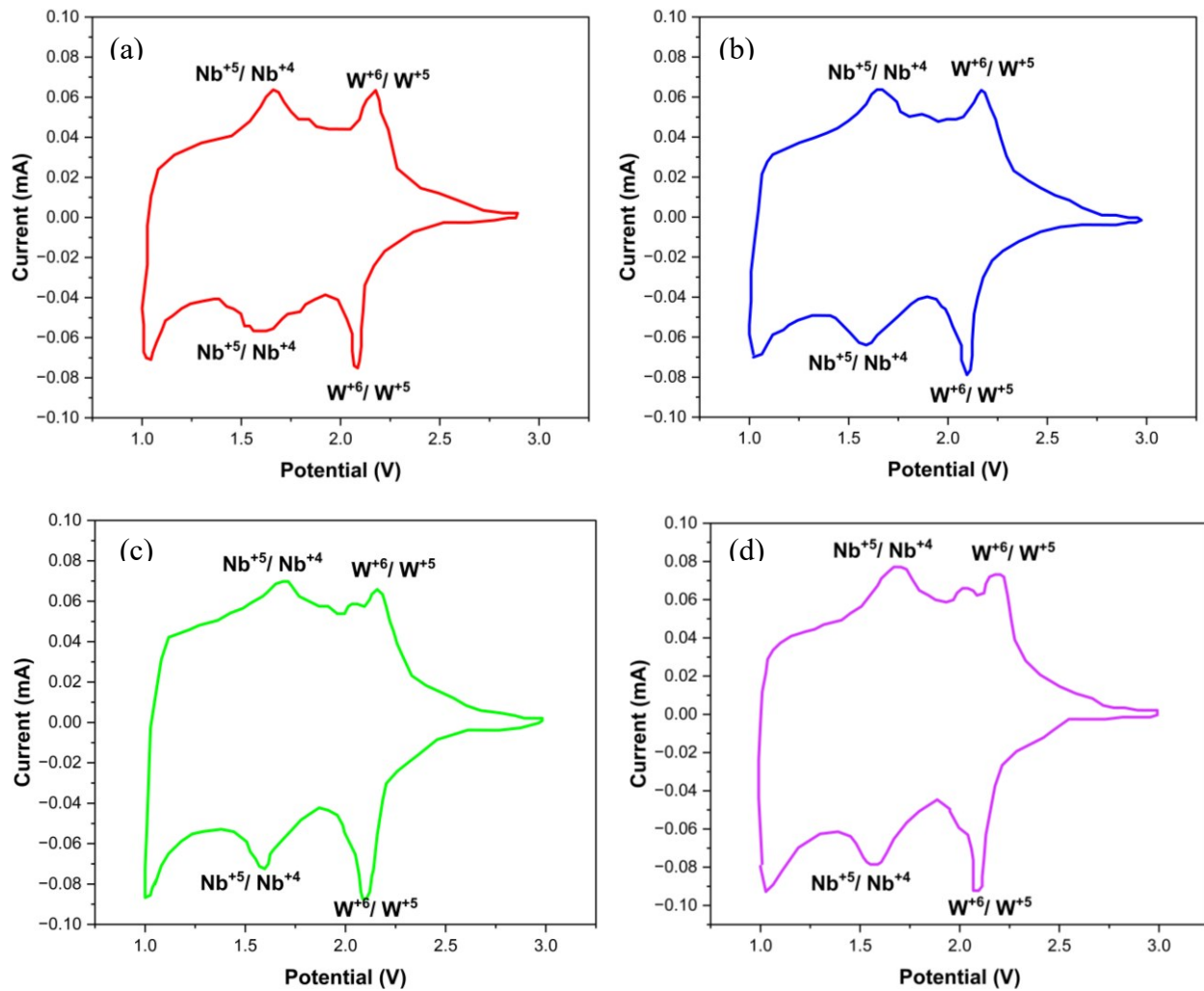


Figure S4-5: CV curve of (a) NWO, (b) NWO-Ni-1, (c) NWO-Ni-3, (d) NWO-Ni-5

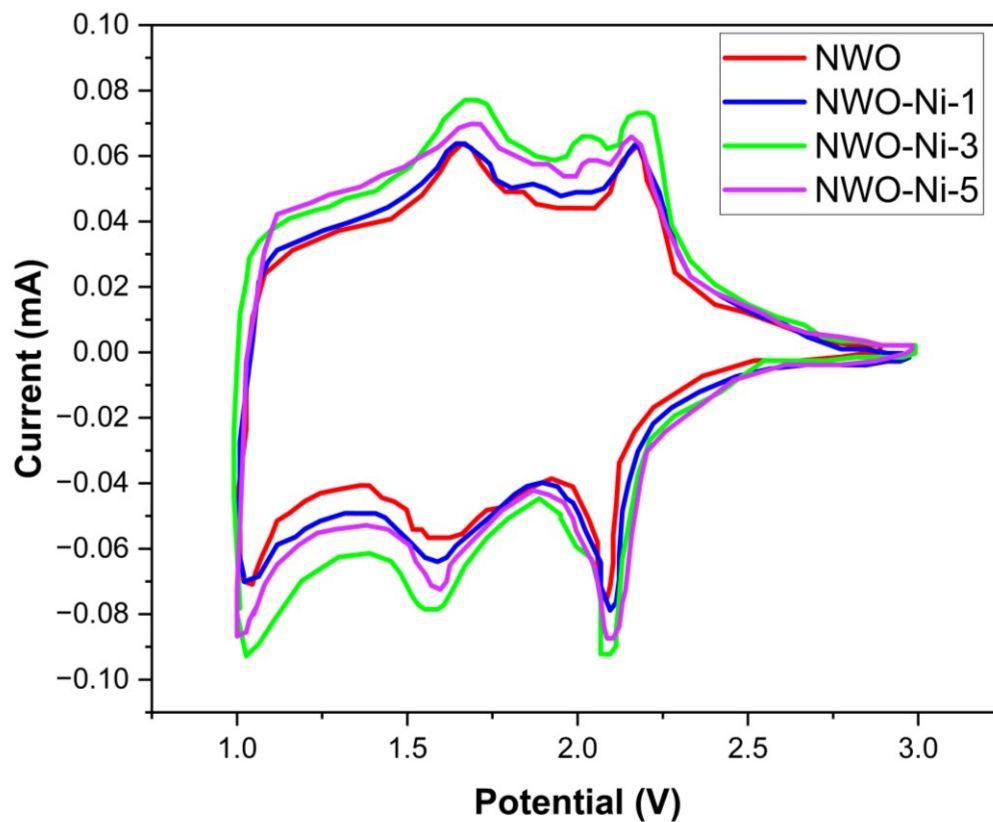


Figure S4-6: CV curve of NWO, NWO-Ni-1, NWO-Ni-3, and NWO-Ni-5

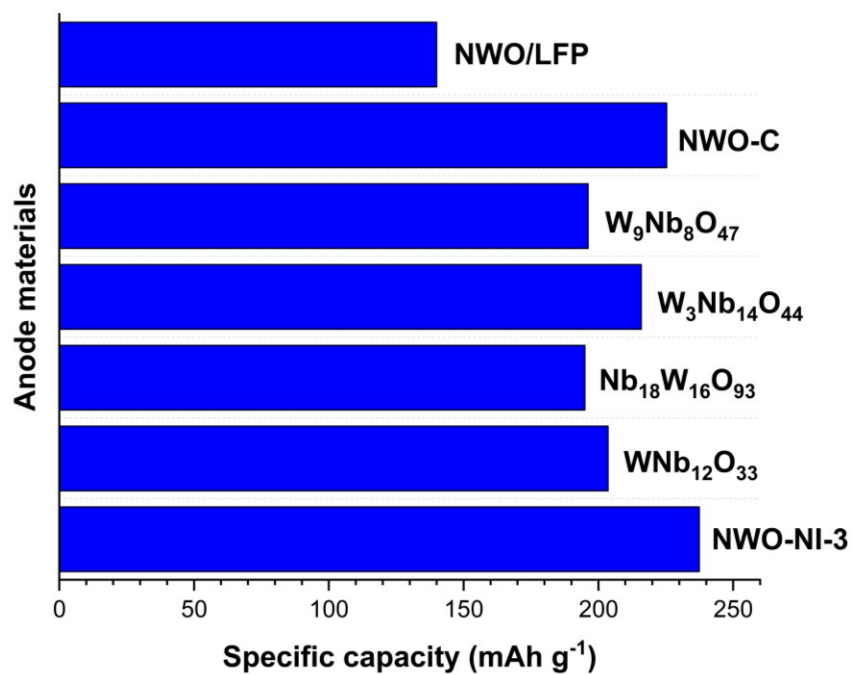


Figure S4-7: Comparison of initial specific capacity of NWO-Ni-3 with previous works

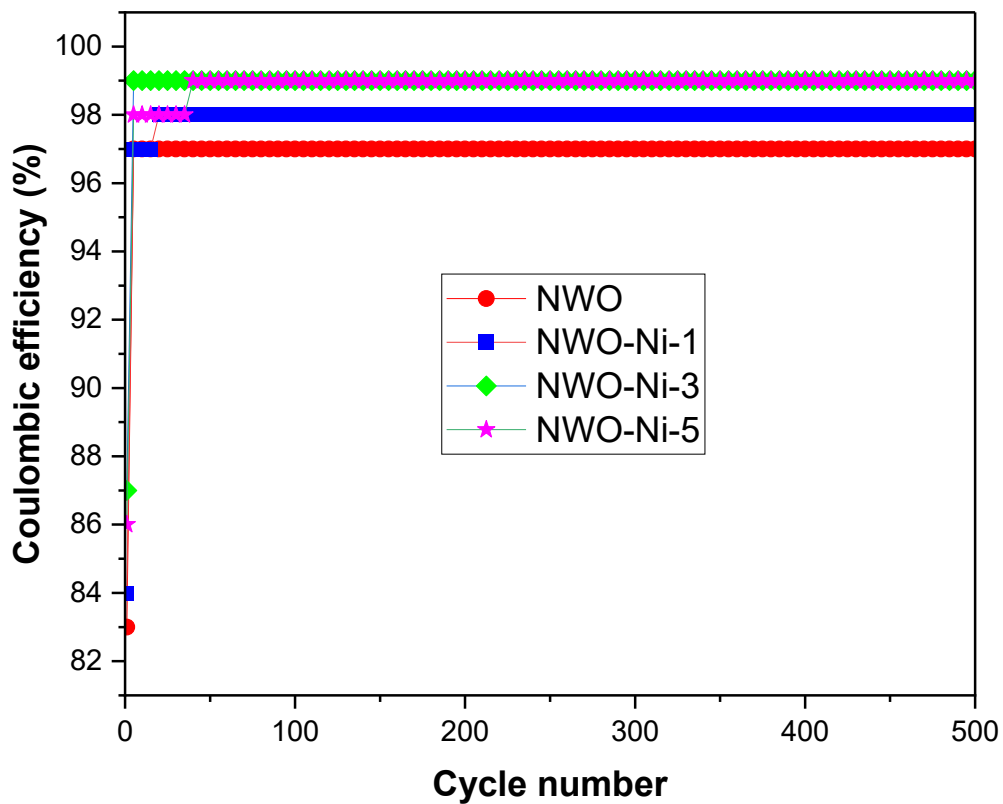


Figure S4-8: Coulombic efficiency of NWO, NWO-Ni-1, NWO-Ni-3, and NWO-Ni-5 at 5 C.

Table S4-2: Comparisons of cycling performance of NWO-Ni-3 with other niobate anode materials.

<b>Material</b>	<b>Capacity loss (%)</b>	<b>Capacity loss per cycle (%)</b>	<b>C-rate</b>	<b>Ref.</b>
NWO-Ni-3	6.9% over 500 cycles	0.0138	5 C	This work
NWO	13.5% over 500 cycles	0.0270	5 C	This work
NWO-C	31.8% over 300 cycles	0.1060	5 C	[10]
N-W <sub>9</sub> Nb <sub>8</sub> O <sub>47</sub>	9.3% over 200 cycles	0.0465	1 C	[176]
NWO/LFP	7.9% over 500 cycles	0.0158	5 C	[6]
TiNb <sub>2</sub> O <sub>7</sub>	14.5% over 500 cycles	0.0290	6 C	[67]
M-TiNb <sub>24</sub> O <sub>62</sub>	9.3% over 500 cycles	0.0400	10 C	[41]
CrNb <sub>14</sub> O <sub>29</sub> -R	8.9% over 400 cycles	0.0223	10 C	[7]
GaNb <sub>11</sub> O <sub>29</sub> -N	12.6 % over 1000 cycles	0.0126	10 C	[8]
FeNb <sub>11</sub> O <sub>29</sub>	14.2 % over 1000 cycles	0.0142	10 C	[12]
Cr <sub>0.5</sub> Nb <sub>24.5</sub> O <sub>62</sub> -N	7.2 % over 500 cycles	0.0144	10 C	[192]
NMO@N	36.2 % over 503 cycles	0.0720	0.5 C	[40]
AlNb <sub>11</sub> O <sub>29</sub> -N	6.8 % over 1000 cycles	0.0136	10 C	[193]
Graphite (NG)*	8.0% over 30 cycles	0.2700		[200]

\*Cycling performance of graphite was reported at current density of 0.2 mA cm<sup>-2</sup>

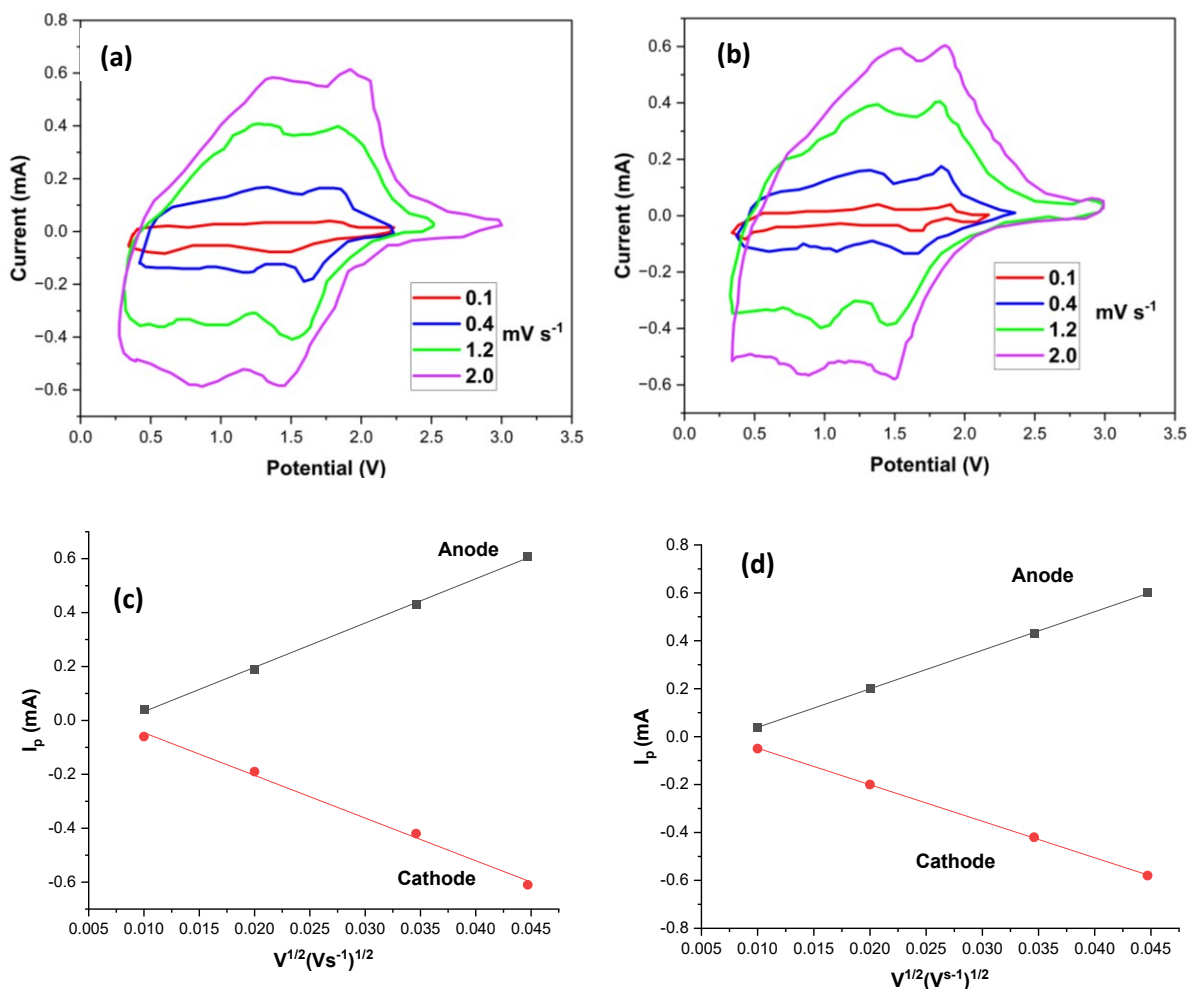


Figure S4-9: (a,b) CV curves of NWO-Ni-3 and NWO-Ni-5 at different scan rates, (c,d) relationships between peak current and the square root of the scan rate of NWO-Ni-3 and NWO-Ni-5.

Table S4-3: The diffusion coefficients of Li<sup>+</sup> obtained from the CV curves.

Sample	$D_{Li}$ (cm <sup>2</sup> s <sup>-1</sup> )	
	Cathodic peak	Anodic peak
NWO	$1.11 \times 10^{-13}$	$1.52 \times 10^{-13}$
NWO-Ni-1	$3.05 \times 10^{-13}$	$2.97 \times 10^{-13}$
NWO-Ni-3	$8.26 \times 10^{-13}$	$7.82 \times 10^{-13}$
NWO-Ni-5	$7.89 \times 10^{-13}$	$8.11 \times 10^{-13}$

Table S4-4: Comparisons of Li<sup>+</sup> diffusion coefficients in this work with other niobate-based anode materials.

<b>Samples</b>	<b>D<sub>Li+</sub> (cm<sup>2</sup> s<sup>-1</sup>)</b>	<b>Reference</b>
NWO-Ni-3	3.23 x 10 <sup>-12</sup>	This work
NW-Nb <sub>18</sub> W <sub>16</sub> O <sub>93</sub>	1.31 x 10 <sup>-13</sup>	[47]
2h Nb <sub>18</sub> W <sub>16</sub> O <sub>93</sub>	3.24 x 10 <sup>-12</sup>	[3]
W <sub>9</sub> Nb <sub>8</sub> O <sub>47</sub>	2.23 x 10 <sup>-13</sup>	[176]
W <sub>3</sub> Nb <sub>14</sub> O <sub>44</sub>	8.02 x 10 <sup>-14</sup>	[49]
24h Nb <sub>18</sub> W <sub>16</sub> O <sub>93</sub>	4.63 x 10 <sup>-14</sup>	[191]
Cr <sub>0.5</sub> Nb <sub>24.5</sub> O <sub>62</sub> -N	2.19 x 10 <sup>-13</sup>	[192]
AlNb <sub>11</sub> O <sub>29</sub>	1.12 x 10 <sup>-13</sup>	[193]
ZrNb <sub>14</sub> O <sub>37</sub>	4.63 x 10 <sup>-14</sup>	[75]
Ti <sub>2</sub> Nb <sub>10</sub> O <sub>29</sub>	8.97 x 10 <sup>-18</sup>	[195]
MoNb <sub>12</sub> O <sub>33</sub>	4.00 x 10 <sup>-14</sup>	[196]

Table S4-5: Lithium-ion diffusion coefficients obtained from the EIS.

<b>Samples</b>	<b>R<sub>s</sub> (Ω)</b>	<b>R<sub>ct</sub> (Ω)</b>	<b>σ (Ω s<sup>-0.5</sup>)</b>	<b>D<sub>Li</sub> (cm<sup>2</sup> s<sup>-1</sup>)</b>
<b>NWO</b>	1.86	190.70	77.51	5.40 x 10 <sup>-13</sup>
<b>NWO-Ni-1</b>	1.63	134.60	45.32	1.28 x 10 <sup>-12</sup>
<b>NWO-Ni-3</b>	1.48	68.30	30.86	3.23 x 10 <sup>-12</sup>
<b>NWO-Ni-5</b>	1.54	84.20	43.70	3.07 x 10 <sup>-12</sup>

#### 4.5. Overview of chapter 4

Chapter four presents the nickel-doped  $\text{Nb}_{18}\text{W}_{16}\text{O}_{93}$  nanowires with improved electrochemical properties for lithium-ion battery anodes. The results obtained in this study motivated us to explore the possibility of enhancing the electronic conductivity, lithium-ion mobility, and electrochemical kinetics of  $\text{MoNb}_{12}\text{O}_{33}$  using the hydrogenation process. The next chapter focuses on the fabrication and assessment of electrochemical performance of  $\text{MoNb}_{12}\text{O}_{33}$  nanowires.

## Chapter 5: Enhancing niobium-based oxides for high-performance lithium-ion batteries through hydrogenation.

Babajide Oluwagbenga Fatile, Martin Pugh, Mamoun Medraj  
Department of Mechanical, Industrial, and Aerospace Engineering, Concordia University,  
Montreal, Canada

This paper has been published in Journal of Solid State Electrochemistry, doi:  
<https://doi.org/10.1007/s10008-023-05644-1>

### Abstract

Niobium-based oxides have attracted widespread research enthusiasm in the field of energy storage systems, including lithium-ion batteries (LIBs). Most recently,  $\text{MoNb}_{12}\text{O}_{33}$  was reported as a promising material for LIBs due to its long-term cyclability, high theoretical and practical capacities, safe operating potential, and excellent structural stability. Nevertheless, the kinetics of electrochemical reactions in  $\text{MoNb}_{12}\text{O}_{33}$  is hindered by its intrinsically poor electronic conductivity and electron transfer properties. These tend to be significant flaws restricting its practical use in LIBs. In this study, we employed an electrospinning technique and subsequent hydrogenation treatment for fabricating NMO and NMO@H-Ar nanowires (@H-Ar denotes heat treatment under Hydrogen and Argon mixture). The hydrogenation treatment narrows the band gap, expands unit cell volume, and creates oxygen vacancies in NMO@H-Ar. These resulted in outstanding electrochemical kinetics in the NMO@H-Ar anode, including a high reversible specific capacity of  $327 \text{ mAh g}^{-1}$  at 0.1 C, high initial coulombic efficiency of 92.4 %, excellent long-term cycling stability with capacity retention of 94.4 % (capacity loss per cycle of 0.0056 %) after 1000 cycles at 10 C, and good rate performance of  $179.7 \text{ mAh g}^{-1}$  at 10 C. In addition, the data obtained from the electrochemical impedance and cyclic voltammetry tests confirm that the hydrogenation treatment significantly enhanced the electronic conductivity and lithium-ion diffusion coefficient. This study affirms that the hydrogenation treatment considerably improved

the electronic conductivity and electrochemical reactions kinetics of NMO@H-Ar nanowires, which is beneficial for developing new anode materials for LIBs.

Keywords: Electrochemical performance, oxygen vacancies, anode material, hydrogenation treatment, and lithium-ion battery

## 5.1. Introduction

Over the past decade, energy storage has garnered significant interest, as it is vital for meeting global energy demands and the quest for renewable energy sources [3], [6], [7]. Lithium-ion batteries (LIBs) are one of the most widely used energy storage devices owing to their high energy density, long life cycle, and high output voltage [201] [202]. A typical LIB comprises the cathode, anode, electrolyte, separator, and current collector [175]. Among these components, anodes have a significant impact on the electrochemical performance and safety of LIBs. Anode materials for LIBs can be classified into three groups based on their distinct reaction mechanisms [55], [203]: (i) the intercalation-type anode materials, such as graphite and titanium-based oxides, have high cycling stability and good reversibility, and they undergo slight volume change during electrochemical reactions [55], [204]; (ii) alloying-type anode materials which use alloying processes between lithium and other materials (such as Zn, Cd, Sn, and Si), these materials exhibit high theoretical capacity [205]. However, they suffer significant morphological and volume changes (about 300%) during electrochemical reactions [55], [204], [206]; (iii) the conversion-type anode materials such as sulfides and transition metal oxides which typically store large amount of lithium ions through reversible redox reactions [55]. Nonetheless, their electrochemical performance is limited by large potential hysteresis [206].

Graphite with a multilayer arrangement has been widely utilized as an anode for LIBs due to its low cost, high theoretical capacity ( $372 \text{ mAh g}^{-1}$ ), and low delithiation potential [8], [41], [207]. Nevertheless, the electrochemical performance of graphite is limited by its poor lithium-ion mobility and low  $\text{Li}^+$  intercalation potential ( $< 0.2 \text{ V}$ ), which could result in the formation of lithium dendrites causing short-circuiting, and other safety concerns [8], [10], [17], [208], [209]. To this end, there is need to develop an alternative anode material to replace graphite. Recently, various attempts were made to address the problem of significant volume changes associated with silicon-based anode material during electrochemical reactions. This include the controlled prelithiation of siloxene nanosheet [210] and the use of covalent organic framework to improve the performance of 2D siloxene anode [211]. Nonetheless, the problems of interface between electrolyte and siloxene surface as well as poor electronic conductivity still pose some challenges. Furthermore, 3D architected structure such as porous  $\text{MoS}_2$  foam was recently reported as potential anode material for LIB [212]. However, the lithium-ion diffusion coefficient and electrochemical stability of  $\text{MoS}_2$  are constrained by its brittle and stacked layered structure.

Over the last few years, titanium-based oxides such as  $\text{Li}_4\text{Ti}_5\text{O}_{12}$  (LTO) have been widely investigated as alternative anode materials due to their remarkable cycling stability and safe operating potential ( $1.5 \text{ V}$  for  $\text{Li}^+$  intercalation/de-intercalation), which prevent the formation of dendrites associate with the use of graphite as an anode material [213]–[215]. Nevertheless, the low theoretical capacity ( $175 \text{ mAh g}^{-1}$ ) is a major drawback that limits its use as a commercial anode for LIBs [175], [215], [216]. Currently, intercalation-type Nb-M-O compounds such as  $\text{Nb}_{18}\text{W}_{16}\text{O}_{93}$  [47], [209],  $\text{WNb}_{12}\text{O}_{33}$  [142],  $\text{Cr}_{0.5}\text{Nb}_{24.5}\text{O}_{62}$  [192],  $\text{CuNb}_2\text{O}_6$  [53], and  $\text{AlNb}_{11}\text{O}_{29}$  [193] are attracting attention as potential anode materials for LIBs. These compounds have been

reported to possess an open-shear  $\text{ReO}_3$  crystal structure which is beneficial for enhanced  $\text{Li}^+$  mobility during the cycling process and ensures high-rate performance [8], [40], [217]. The unique crystal architecture also guarantees small volume changes during  $\text{Li}^+$  intercalation/de-intercalation; this presents minimal structural stress on the anode materials, which results in high structural stability and good cyclability [40]. Besides, the working potential of these compounds is greater than 1 V; this prevents the formation of a solid electrolyte film, which ensures their safe operation as LIBs anode materials [50], [218]. Notably, the multiple redox chemistry in Nb-M-O compounds ( $\text{Nb}^{5+}/\text{Nb}^{4+}$  and  $\text{Nb}^{4+}/\text{Nb}^{3+}$ ) ensures high specific capacities. For instance, the theoretical specific capacity of  $\text{Ti}_2\text{Nb}_{10}\text{O}_{29}$ ,  $\text{GeNb}_{18}\text{O}_{47}$ , and  $\text{Mo}_3\text{Nb}_{14}\text{O}_{44}$  are 396, 386.4, and 398  $\text{mAh g}^{-1}$ , respectively [72], [218], [218]. Despite having large theoretical capacities and a relatively safe operating voltage, their intrinsic low electronic conductivity still limits their practical application as anode materials for LIBs [70], [75]. This will be addressed in our work.

Over the last few years, various researchers, including our group, have employed several approaches such as doping [12], [54], [67], nanostructures [40], [196], [218], surface modification [10], [176], hierarchical structures [219], and controlled annealing [51], [207], [220] to improve the electronic conductivity and electrochemical performance of Nb-M-O compounds. A recent study by our research group demonstrated that the specific capacity and lithium-ion diffusion coefficient of  $\text{Nb}_{18}\text{W}_{16}\text{O}_{93}$  increased from 239.0 to 274.1  $\text{mAh g}^{-1}$  and  $1.35 \times 10^{-13}$  to  $8.07 \times 10^{-13} \text{ cm}^2 \text{ s}^{-1}$ , respectively, by doping with 3 wt.% nickel [209]. Controlled annealing is another method that has been widely employed for improving the performance because it tends to generate more oxygen vacancies in the anode materials [41], [208], [220]. The presence of oxygen vacancies in anode materials could modify the electronic conductivity, lower the energy required for lithium-ion migration, and lower the stress during  $\text{Li}^+$  intercalation/de-

intercalation. All these are beneficial for improving electrochemical kinetics of anode materials [213], [220], [221]. For instance, Zhu *et al.* [41] fabricated  $\text{TiNb}_{24}\text{O}_{62}$  nanowires and boosted the electrochemical kinetics by annealing in a mixture of hydrogen and argon. They established that the annealing resulted in the creation of oxygen vacancies which tremendously improved the electronic conductivity and electrochemical kinetics of  $\text{TiNb}_{24}\text{O}_{62}$ . Zhang *et al.* [213] also annealed  $\text{Nb}_2\text{O}_5$  nanoparticles in a mixture of 50%  $\text{H}_2$  and 50% Ar at  $750^\circ\text{C}$ , the treatment substantially improved the electrochemical performance of the  $\text{Nb}_2\text{O}_5$  nanoparticles. This improvement was also attributed to the creation of oxygen vacancies in the material and this has motivated us to embark on this research.

Most recently, another niobium-based compound  $\text{MoNb}_{12}\text{O}_{33}$ , with a large theoretical capacity ( $401 \text{ mAh g}^{-1}$ ), was reported [196]. The compound exhibits a Wadsley-Roth crystal structure, characterized by the arrangement of  $\text{Mo}^{6+}$  ions exclusively at the tetrahedral sites. This configuration contributes to its high theoretical capacity, enhanced structural stability, and cyclability [196]. Furthermore, this open configuration offers vacant sites with open tunnels that can reversibly accommodate  $\text{Li}^+$  ions and facilitate rapid  $\text{Li}^+$  transportation without causing significant volume expansion. The unit-cell volume expansion of  $\text{MoNb}_{12}\text{O}_{33}$  is 6.79%, which is smaller than that of graphite (13.2%) [222] and close to that of  $\text{Nb}_{18}\text{W}_{16}\text{O}_{93}$  (4.6%) [47]. Zhu *et al.* [196] studied the electrochemical kinetics of  $\text{MoNb}_{12}\text{O}_{33}$  by preparing  $\text{MoNb}_{12}\text{O}_{33}$  microparticles (designated as M- $\text{MoNb}_{12}\text{O}_{33}$ ) and  $\text{MoNb}_{12}\text{O}_{33}$  porous microspheres (designated as P- $\text{MoNb}_{12}\text{O}_{33}$ ) using a solvothermal synthesis method. The results show that the P- $\text{MoNb}_{12}\text{O}_{33}$  exhibited a superior specific capacity and cycling stability compared to M- $\text{MoNb}_{12}\text{O}_{33}$ . Likewise, the P- $\text{MoNb}_{12}\text{O}_{33}$  displayed a lower charge transfer resistance ( $109 \Omega$ ) compared to M- $\text{MoNb}_{12}\text{O}_{33}$  ( $248 \Omega$ ), while the capacity retention for P- $\text{MoNb}_{12}\text{O}_{33}$  and M-

MoNb<sub>12</sub>O<sub>33</sub> after 1000<sup>th</sup> cycles are 95.7% and 89.2%, respectively. The remarkable electrochemical performance of P-MoNb<sub>12</sub>O<sub>33</sub> porous microspheres compared to the microparticles further inspired us to study the electrochemical kinetics of MoNb<sub>12</sub>O<sub>33</sub> nanowires. In addition, nanowires' architectural structure and morphology are more suitable for fabricating high-performance LiBs anode than the microspheres owing to their high surface area-to-volume ratio and limited self-aggregation [192], [223].

Herein, we demonstrated the possibility of enhancing the electronic conductivity, lithium-ion mobility, and electrochemical kinetics of MoNb<sub>12</sub>O<sub>33</sub> through the synergetic effects of using a nanostructure strategy and a hydrogenation process. This study offers a new understanding of the hydrogenation treatment effects on the overall electrochemical activities of MoNb<sub>12</sub>O<sub>33</sub>. In this study, the electrospinning method was used to successfully fabricate MoNb<sub>12</sub>O<sub>33</sub> nanowires, followed by controlled annealing in a mixture of 5% hydrogen and argon for one hour. The effect of the controlled annealing on morphology and electrochemical activities of MoNb<sub>12</sub>O<sub>33</sub> were investigated and compared with other anode materials from the literature.

## 5.2 Experimental

### 5.2.1 Fabrication of MoNb<sub>12</sub>O<sub>33</sub> nanowires

The MoNb<sub>12</sub>O<sub>33</sub> nanowires (NMO) were fabricated using the electrospinning technique followed by hydrogenation treatment. The precursor solution for electrospinning was prepared by dissolving 0.15 mmol MoO<sub>2</sub>(acac)<sub>2</sub> (99%, Sigma Aldrich) and 1.80 mmol NbCl<sub>5</sub> (99.9%, Sigma Aldrich) (98%, Sigma Aldrich) in a mixture of 15 mL ethanol (98%, Sigma Aldrich) and 5 mL distilled water. The mixture was stirred vigorously for 12 h, followed by the addition of 2.0 g poly(vinyl pyrrolidone) (MW 1,300,000 gmol<sup>-1</sup>, 100% purity, Sigma Aldrich). The resulting mixture was then continuously stirred for 12 h to obtain a homogenous viscous solution at which

time; the precursor solution was transferred into a 10 mL syringe with a needle. The electrospinning was carried out using a piece of clean aluminum foil placed about 18 cm from the tip of the needle as a collector. The electrospinning process was carried out at room temperature under a voltage of 20 kV and a solution flow rate of 0.8 ml h<sup>-1</sup>. The as-spun nanofibers were collected and calcined for 6 h at 900°C in a box furnace, and the resulting nanowires obtained were denoted as NMO. Meanwhile, NMO@H-Ar nanowires were obtained by adding a hydrogenation process to the procedure used for obtaining NMO. The NMO nanowires were calcined in a tubular furnace under a mixture of 5% Hydrogen/Argon gas at 720°C for 1 h at a flow rate of 50 sccm. Figure 5-1 depicts a schematic illustration of the nanowire fabrication process.

### **5.2.2. Material characterization**

The morphological characteristics of NMO@H-Ar and NMO were studied by Scanning Electron Microscope (Hitachi Regulus 8230) equipped with an energy dispersive X-ray spectrometer (EDX) detector for the elemental mapping analysis and Scanning Transmission Electron Microscopy (STEM) detector for microstructures. X-ray diffraction (XRD) (PANAnalytical X'pert Pro X-ray diffractometer) equipped with a CuK  $\alpha$  radiation source, ( $\lambda = 1.5406 \text{ \AA}$ ) was used for crystal structure identification. The elemental and valence states of Mo and Nb were obtained using the X-ray photoelectron spectroscopy (XPS) ESCALAB 250 XI X-ray photoelectron microprobe (Thermo Scientific K-Alpha). The electronic properties of the nanowires were studied using electron paramagnetic resonance (EPR) using a Bruker Elexsys E580 X-band EPR spectrometer (Billerica, MA, USA); and ultraviolet-visible spectroscopy (UV–Vis) was performed on a Perkin Elmer UV/VIS/NIR Spectrometer Lambda 750 (Boston, MA, USA) using Barium sulfate as a white reference.

### 5.2.3 Electrochemical test

The electrochemical characterization of NMO and NMO@H-Ar was carried out using coin-type cells (CR2032). Firstly, the working electrodes were fabricated using the prepared anode material (NMO and NMO@H-Ar), acetylene black, and a binder (polyvinylidene fluoride) at a weight ratio of 80:10:10 to obtain working electrodes with a mass loading of active material to about  $1.1 \text{ mg cm}^{-2}$ . The working electrode fabrication and coin cell assembling were carried out using the procedures described in our previous work [209]. A Corrtest potentiostat (Corrtest CS 2350 Bipotentiostat) and 8-channel battery analyzers (MTI corporation BST8-WA) were used to assess the galvanostatic discharge/charge characteristics of the coin cells at various current rates in the potential range of 0.8 to 3.0 V. Cyclic voltammetry (CV) measurements were acquired at a sweep rate of  $0.2 \text{ mV s}^{-1}$ , and the electrochemical impedance (EIS) was measured under an open-circuit voltage after the initial ten CV cycles. The electrochemical tests were all carried out at room temperature.

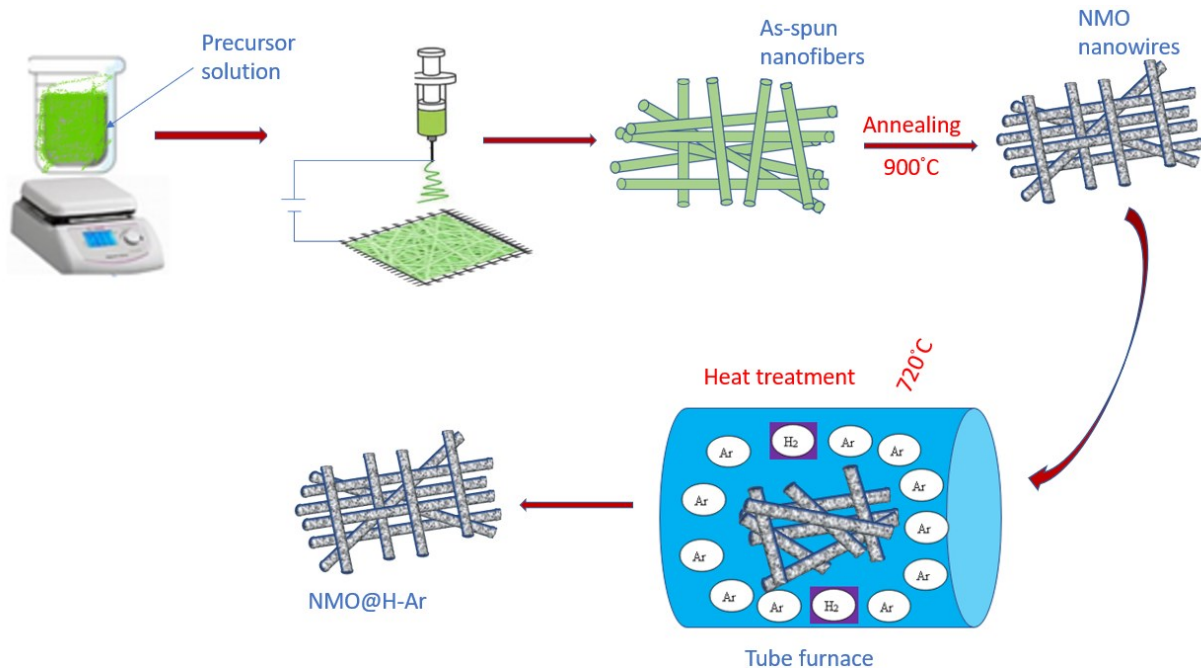


Figure 5-1: Schematic illustration of the electrospinning and hydrogenation process

### 5.3. Results and discussion

The morphology of as-spun nanofibers, NMO, and NMO@H-Ar is presented in Figure 5-2. Figure 5-2a shows that the as-spun nanofibers are relatively uniform with a smooth surface. After annealing, the surface of NMO becomes rough and porous with a structure of nanoparticle-in-nanowires (Figure 5-2b). The morphology of NMO@H-Ar obtained after the hydrogenation process (Figure 5-2c) is similar to that of NMO, with an average diameter of 90 – 120 nm. The EDS mapping analysis results in Figure 5-2d-h confirm the presence of Mo, Nb, and O; it also shows that the elements are evenly distributed in the nanowires. The XRD patterns of NMO and NMO@H-Ar are shown in Figure 5-3a. All the diffraction peaks observed are well indexed to the monoclinic crystal structure (space group:  $C2$ ) (JCPDS card No. 73-1322). The absence of secondary phases and identical diffraction peaks of NMO and NMO@H-Ar indicates that the hydrogenation process did not alter the crystal structure. Meanwhile, some of the diffraction peaks in NMO@H-Ar shifted slightly to a lower angle. The refined lattice parameters of NMO@H-Ar are  $a = 22.9413 \text{ \AA}$ ,  $b = 3.8230 \text{ \AA}$ ,  $c = 17.7306 \text{ \AA}$ ,  $\beta = 123.2^\circ$ , and unit cell volume of  $1295.2 \text{ \AA}^3$ . This is larger than that of NMO with  $a = 22.3712 \text{ \AA}$ ,  $b = 3.8106 \text{ \AA}$ ,  $c = 17.7425 \text{ \AA}$ ,  $\beta = 123.8^\circ$ , and unit cell volume of  $1256.9 \text{ \AA}^3$ . The increased unit cell volume observed in NMO@H-Ar could facilitate the interstitial diffusion of lithium ions, which could be advantageous for enhancing their electrochemical performance [11].

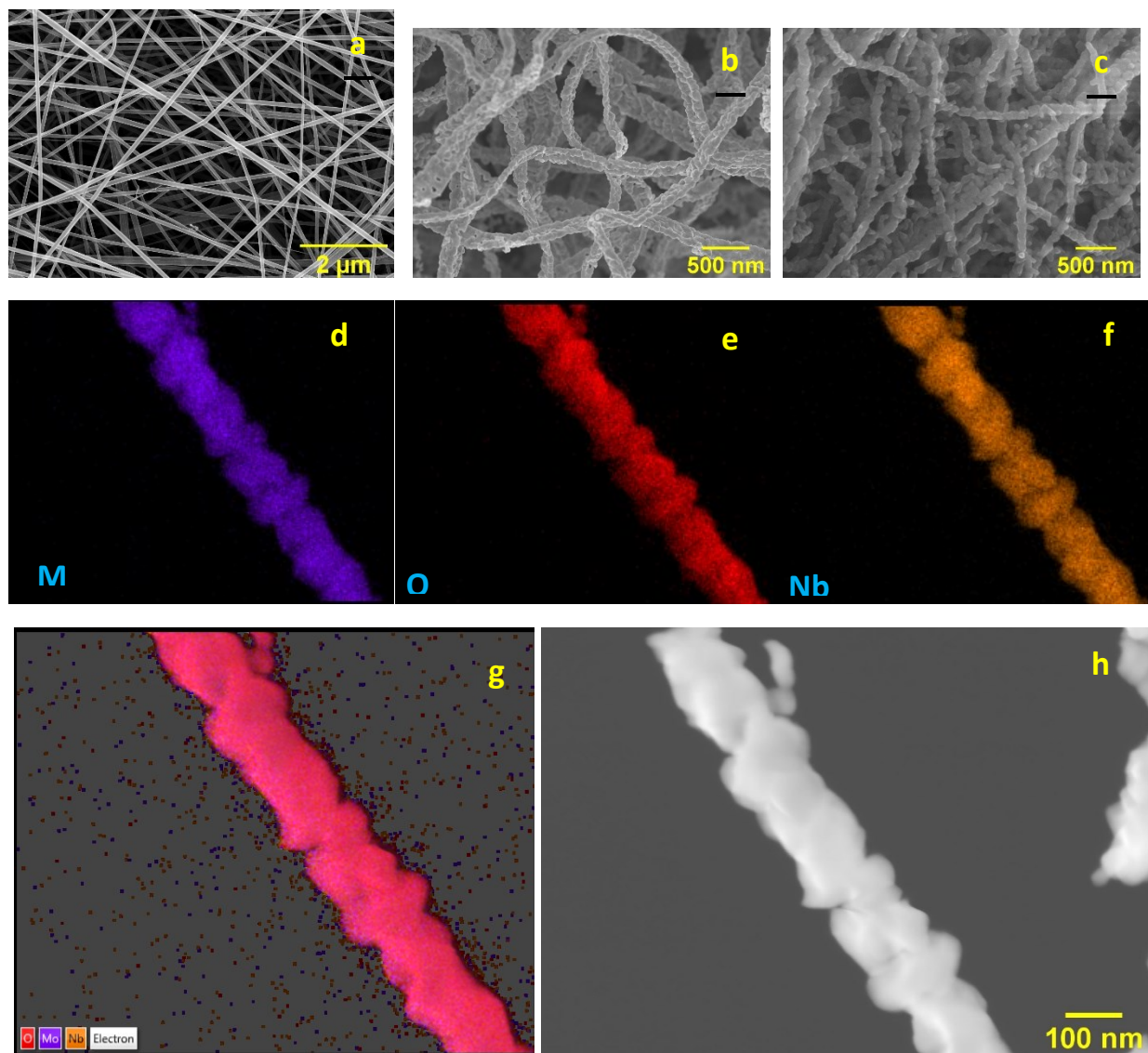


Figure 5-2: SEM images of (a) as-spun nanofibers; (b) NMO (c) NMO@H-Ar; (d-g) corresponding EDS elemental mapping images of Mo, O, and Nb elements in NMO; and (h) STEM image of NMO

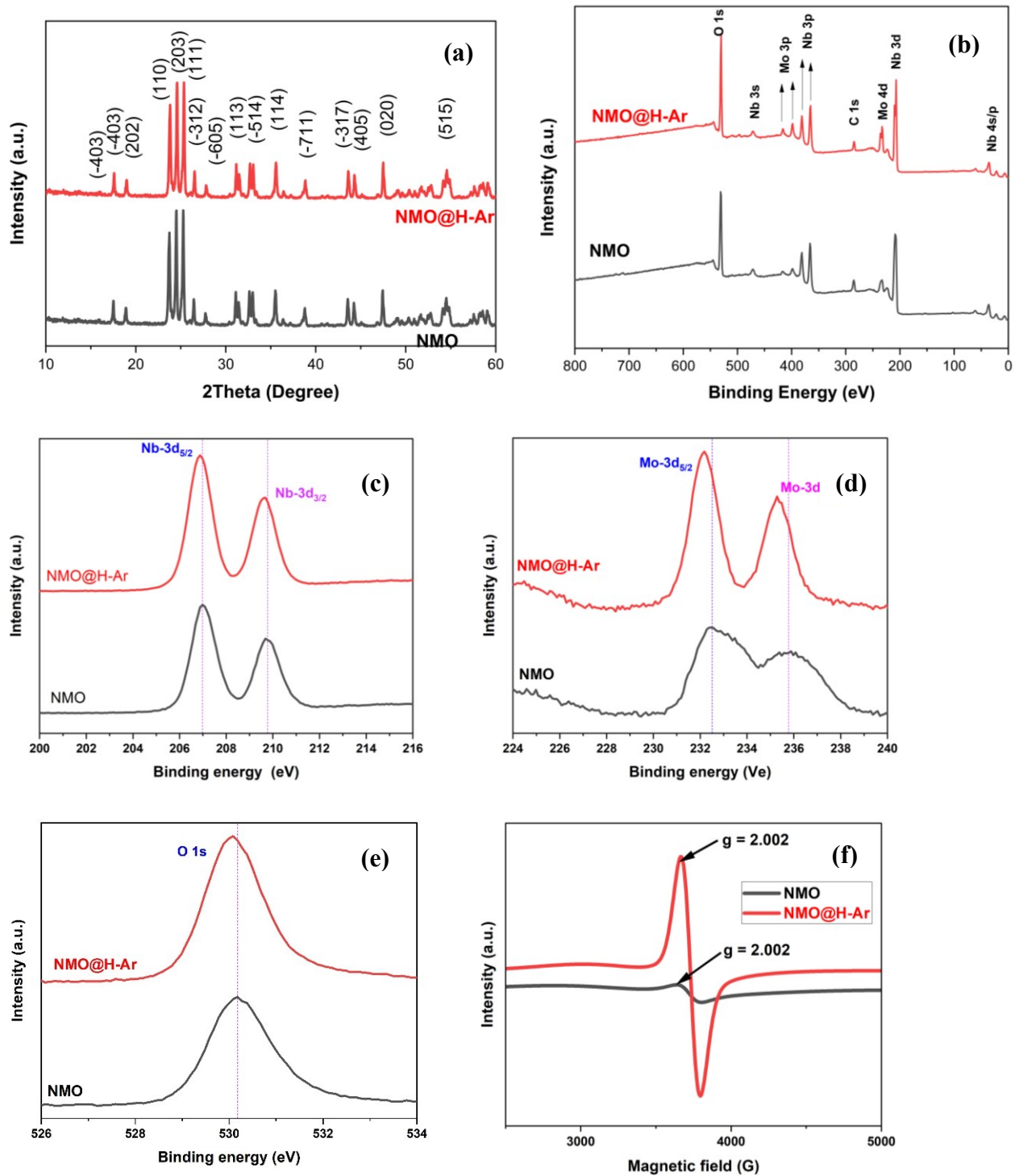


Figure 5-3: (a) XRD pattern of NMO and NMO@H-Ar; (b) XPS survey spectra of NMO and NMO@H-Ar; XPS spectra of (c) Nb 3d; (d) Mo 3d; (e) O 1s; (f) EPR spectra of NMO and NMO@H-Ar

The composition and chemical states of elements in NMO and NMO@H-Ar are determined by XPS analysis. The survey scan presented in Figure 5-3b confirms the presence of Nb, Mo, and O (the carbon signal originating from the reference) in NMO and NMO@H-Ar. The high-resolution image of Nb 3d spectra in Figure 5-3c shows the two distinct characteristic peaks at 206.9 eV and 209.8 eV, which correspond to Nb 3d<sub>5/2</sub> and Nb 3d<sub>3/2</sub>, respectively; this affirms the presence of Nb<sup>5+</sup> in NMO and NMO@H-Ar. The Mo 3d spectra in Figure 5-3d also show two peaks at 232.5 eV and 235.7, which correspond to the Mo 3d<sub>5/2</sub> and Mo 3d<sub>3/2</sub>, respectively; this also confirms the presence of Mo<sup>6+</sup>. On the other hand, the O 1s spectra (Figure 5-3e) of NMO and NMO@H-Ar showed a characteristic peak at 530.2 eV, representing the bonding of Mo-O and Nb-O [41].

It is worth noting that the binding energy of NMO@H-Ar is shifted to the lower value; indicating that oxygen vacancies are generated as a result of the hydrogenation process, which could enhance the electron cloud density of the NMO@H-Ar [41]. EPR analysis was employed to study the presence and status of oxygen vacancies in NMO and NMO@H-Ar because of its ability to identify unpaired electrons in materials both qualitatively and quantitatively. The EPR spectra in Figure 5-3f show that both NMO and NMO@H-Ar display an EPR signal at  $g = 2.0020$ , which could be attributed to single electron trapped oxygen vacancy (SETOV). Generally,  $g$  factor (position in the magnetic field where an EPR signal will occur) values between 2.0010 and 2.0040 are assigned to (SETOV), which indicates the presence of oxygen vacancies in the materials [70], [224], [225]. Notably, the resonance peak intensity of NMO@H-Ar, which corresponds to the paramagnetic species concentration, is higher than that of NMO. This confirms that NMO@H-Ar has more oxygen vacancies than NMO [213], [224], [226]. Despite the formation of an abundant number of oxygen vacancies in NMO@H-Ar, the phase

was not altered, as demonstrated by the XRD results in Figure 5-3a. Hence, it can be deduced that oxygen vacancies were only formed on the surface of NMO@H-Ar. Oxygen vacancies have been demonstrated to be an effective method for boosting the electrochemical kinetics and electronic conductivity of metal oxides [226], [227].

The electronic properties of NMO@H-Ar and NMO were further studied by UV–V is analysis in the wavelength range of 200 to 1000 nm. The analysis was carried out to ascertain the presence of surface oxygen vacancies. The absorbance spectra in Figure 5-4a show that NMO absorbed more energy at wavelengths below 400 nm compared to NMO@H-Ar; this is attributable to its large band gap [228]. The band gap energy ( $E_g$ ) of NMO@H-Ar and NMO was estimated using the tangent of the steepest slope in Figure 5-4b as described in the Tauc method [186] for indirect bandgap ( $\gamma = 2$ ) and Kubelka–Munk function [186] in equations (1) and (2), respectively.

$$(F(R_{\infty}) \cdot h\nu)^{1/\gamma} = B(h\nu - E_g) \quad (5-1)$$

$$F(R_{\infty}) = \frac{(1-R_{\infty})^2}{2R_{\infty}} \quad (5-2)$$

Where  $R_{\infty} = 10^{-A}$ ,  $A$  is the absorbance,  $\nu$  is photon frequency,  $B$  is a constant, and  $h$  is the Planck constant.

The results from Figure 5-4b show that the hydrogenation process reduced the bandgap of NMO from 3.12 eV to 2.89 eV (i.e for NMO@H-Ar). The reduction in bandgap could be attributed to the presence of abundant oxygen vacancies in NMO@H-Ar [186], [225], which further confirms the EPR and XPS results.

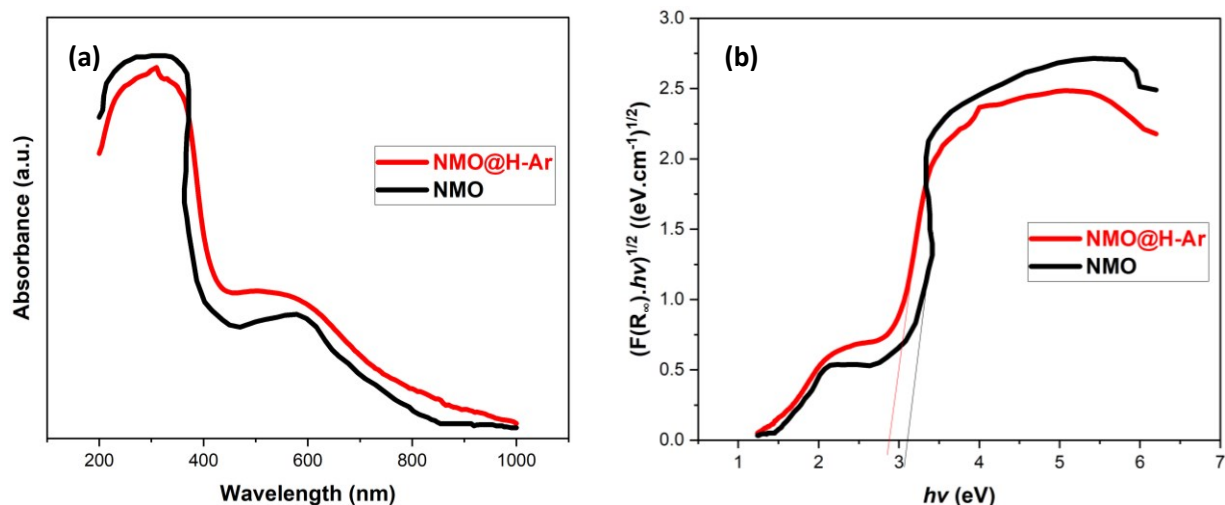


Figure 5-4: (a) UV–Vis absorption data and (b) band gap energy of NMO and NMO@H-Ar

The results of the cyclic voltammetry test obtained at a sweep rate of  $0.2 \text{ mV s}^{-1}$  in the potential range of 0.8 to 3.0 V are presented in Figures 5-5a and b. The CV curves show two redox peaks at 1.82/1.77 and 1.82/1.78 V for NMO and NMO@H-Ar, respectively. This could be assigned to the redox reactions from the  $\text{Mo}^{6+}/\text{Mo}^{5+}$ ,  $\text{Mo}^{5+}/\text{Mo}^{4+}$ , and  $\text{Nb}^{5+}/\text{Nb}^{4+}$  couples [52]. Another pair of peaks is observed at approximately 1.36/1.12 and 1.35/1.12 V for NMO and NMO@H-Ar, respectively. This is attributable to the  $\text{Nb}^{4+}/\text{Nb}^{3+}$  redox pair [52], [196]. The NMO@H-Ar electrode had a smaller potential difference between the cathodic and anodic peaks than the NMO electrode, indicating a slight polarization reduction [47], [176].

Furthermore, the peaks of NMO@H-Ar are higher than NMO, as shown in Figure S5-1. As a result, NMO@H-Ar had improved electrochemical activities owing to its abundant oxygen vacancies, as confirmed by the EPR and UV–Vis absorption results. The CV data also reveal that the average operating potential of NMO and NMO@H-Ar generated from the cathodic/anodic intermediate potential couple following previous studies [16], [196] is 1.80 V; this is comparable to those of other niobium-based anode materials previously reported [8], [16], [192], [229] and

shown in Figure S5-2. Notably, the high working potential of NMO and NMO@H-Ar could inhibit dendritic formation and electrolyte degradation. These findings demonstrate that NMO and NMO@H-Ar have promising suitable growth potential as anode materials for lithium-ion batteries.

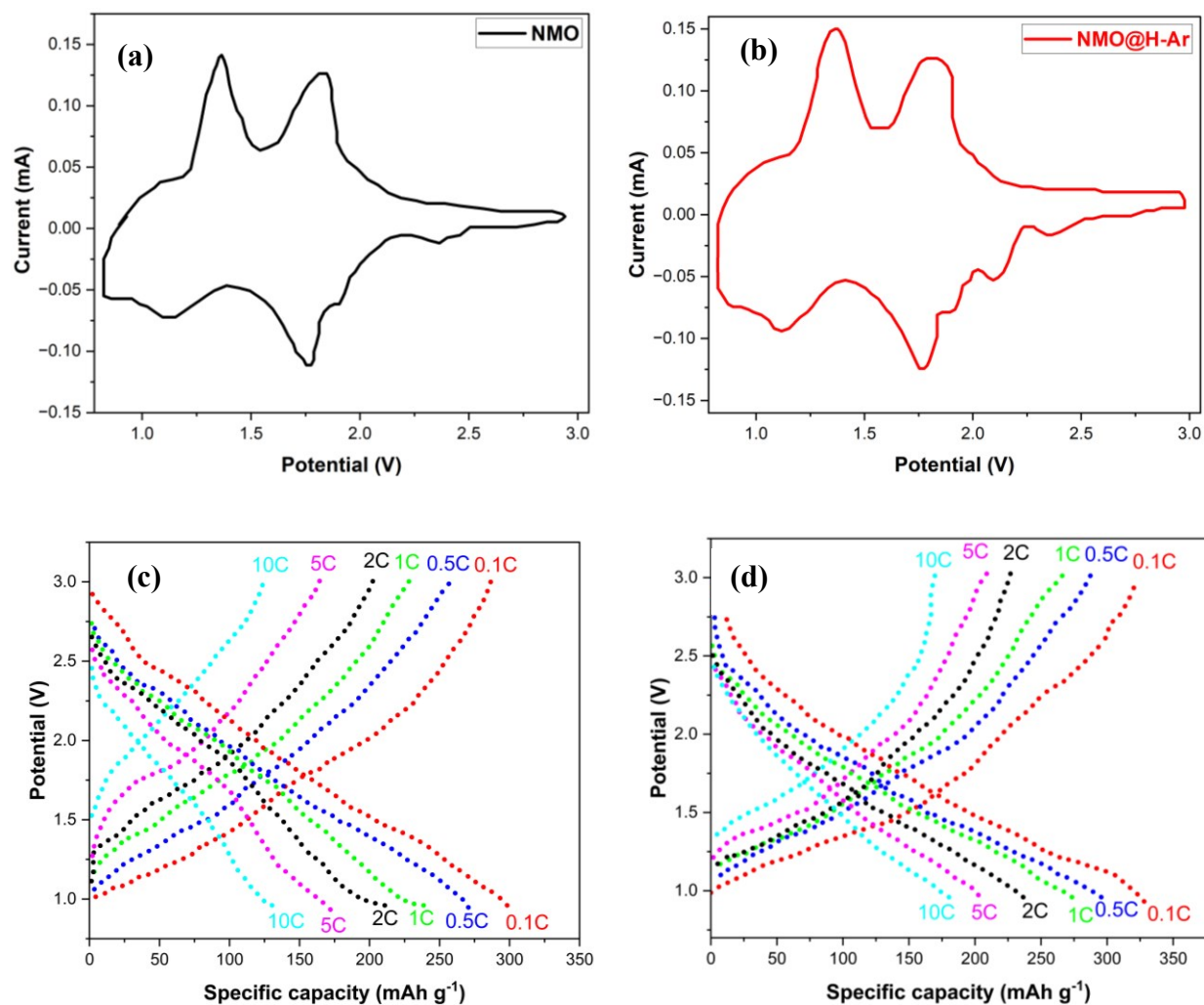


Figure 5-5: CV curve of (a) NMO; (b) NMO@H-Ar; charge/discharge profile for (c) NMO; and (d) NMO@H-Ar.

The electrochemical kinetics of NMO and NMO@H-Ar were also assessed by galvanostatic charge and discharge (GCD) test at the current rates of 0.1, 0.5, 1, 2, 5, and 10 C, as shown in Figures 5-5(c and d). The data obtained at the current rate of 0.1 C show that NMO exhibited a

high reversible specific capacity of 296 mAh g<sup>-1</sup> and coulombic efficiency of 86.3 % after the first cycle, whereas the NMO@H-Ar anode exhibited a greater reversible specific capacity of 327 mAh g<sup>-1</sup> and a higher coulombic efficiency of 92.4 %. The reversible specific capacity of the NMO@H-Ar electrode exceeded that of the majority of anode materials previously reported (Table S5-1) [16], [40], [50], [189], [192], [193], [196], [218]. As the current rate increases, the reversible specific capacity of the electrodes declines gradually. The NMO@H-Ar electrode still delivers a remarkable reversible specific capacity of 296, 274, 236, 201, and 178 mAh g<sup>-1</sup> at 0.5, 1, 2, 5, and 10 C, respectively, while the NMO electrode delivers 269, 238, 211, 173, and 131 mAh g<sup>-1</sup>, respectively. In addition, the redox peaks observed at 1.82/1.77 and 1.36/1.12 V for NMO, and 1.82/1.78 and 1.35/1.12 V for NMO@H-Ar in the CV curves are consistent with the results in the GCD curves, especially at the lower current rate.

Furthermore, the long-term cycling stability and corresponding coulombic efficiency of the electrodes are assessed by GCD at 10 C. The NMO and NMO@H-Ar electrodes exhibit an initial reversible capacity of 131 and 179 mAh g<sup>-1</sup>, respectively. The reversible specific capacity of the two electrodes gradually declines until it reaches 116.9 and 168.9 mAh g<sup>-1</sup>, respectively, after 1000 cycles, as shown in Figure 5-6a; this amounts to an average capacity decay of 0.0108 % and 0.0056 % per cycle for NMO@H-Ar and NMO respectively. The coulombic efficiency of NMO@H-Ar is almost 99% at the end of the 1000 cycles. Notably, the capacity retention rate in Figure S5-3 also shows that NMO@H-Ar retained 98.5 % of its initial reversible capacity after 200 cycles, compared to 95 % reported for NMO. This remarkable cycling stability of NMO@H-Ar is among the best results reported on niobium-based compounds as shown in Table S5-2 [8], [12], [15], [16], [67], [192], [193], [196], [230].

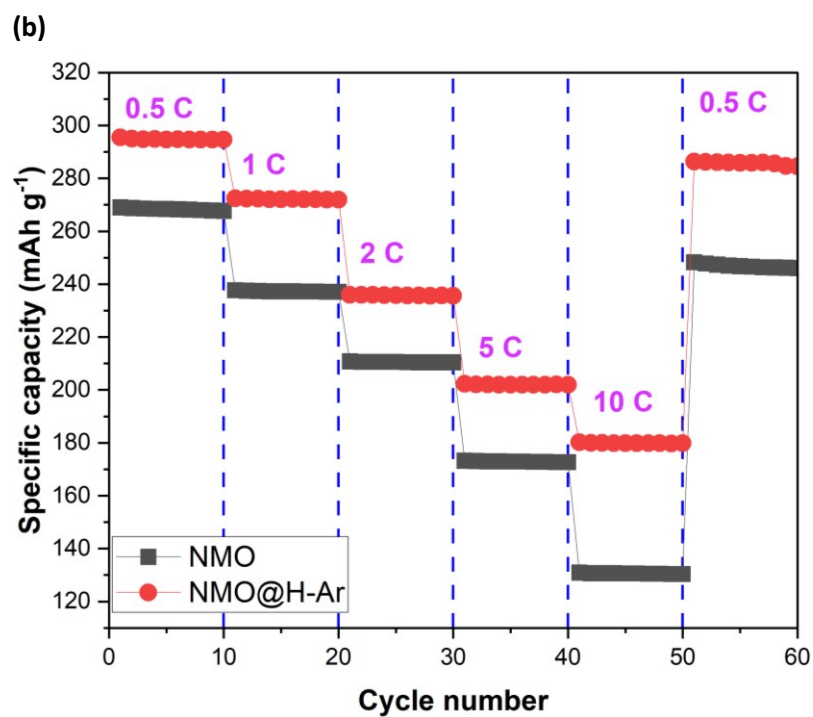
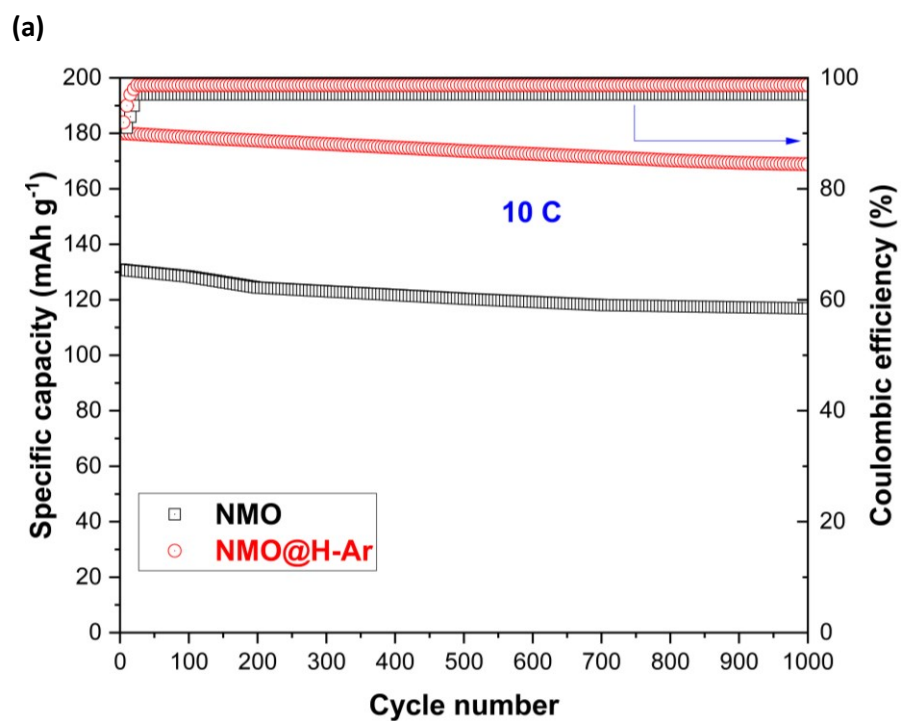


Figure 5-6: (a) Long-term cycling performance of NMO and NMO@H-Ar at 10 C; (b) rate capabilities of NMO and NMO@H-Ar

These findings imply that the oxygen vacancies created in NMO@H-Ar during the hydrogenation process resulted in outstanding cycling stability and excellent reversible specific capacity. The rate capabilities of NMO and NMO@H-Ar are also compared in Figure 5-6b by increasing the current rate from 0.5 to 1, 2, 5, and 10 C, and ultimately recovered when charged at 0.5 C. The results in Figure 5-6b show that the reversible specific capacity of the electrodes decreases steadily as the current density increases, and the NMO@H-Ar electrode exhibits a superior rate performance with a reversible capacity of 295.5, 272.0, 235.7, 202.1, and 179.7 mAh g<sup>-1</sup> at the current rates of 0.5, 1, 2, 5, and 10 C, while NMO electrode delivers 267.7, 210.4, 172.7, and 130.4 mAh g<sup>-1</sup>, respectively. When the current rate returns to 0.5 C, the NMO@H-Ar electrode still recovers a high reversible specific capacity of 284.6 mAh g<sup>-1</sup>, demonstrating superior rate performance over the NMO electrode that recovers 246.1 mAh g<sup>-1</sup>. The superior rate performance exhibited by the NMO@H-Ar electrode is consistent with the trend observed in long-term cycling results. This affirms that the hydrogenation process greatly improved the electrochemical performance of the NMO@H-Ar electrode.

To confirm the influence of oxygen vacancies on the lithium-ion diffusion coefficient of NMO and NMO@H-Ar electrode, the CV test was carried out at different scan rates (0.2, 0.5, 0.7, and 1.0 mV s<sup>-1</sup>), as shown in Figures 5-7a and b. The results in Figure S5-4 show a linear relationship between the peak current ( $I_p$ ) and the square root of the sweep rate ( $V^{1/2}$ ). Based on these results, the apparent lithium-ion diffusion coefficient ( $D$ ) of the NMO and NMO@H-Ar was calculated using the Randles-Sevcik equation [75] (symbols and definitions are in the supporting information).

$$I_p = 269 \times 10^3 n^{3/2} A D^{1/2} C v^{1/2} \quad (5-3)$$

The results in Table S5-3 show that the lithium-ion diffusion coefficient of NMO@H-Ar is about 6.0 times larger than that of NMO. The higher  $\text{Li}^+$  diffusivity observed in NMO@H-Ar could be ascribed to the unit cell volume expansion of 2.96 % that resulted from the hydrogenation process. It was previously reported that the lattice parameters and unit cell volume could have a significant impact on the  $\text{Li}^+$  diffusion coefficient [15], [194].

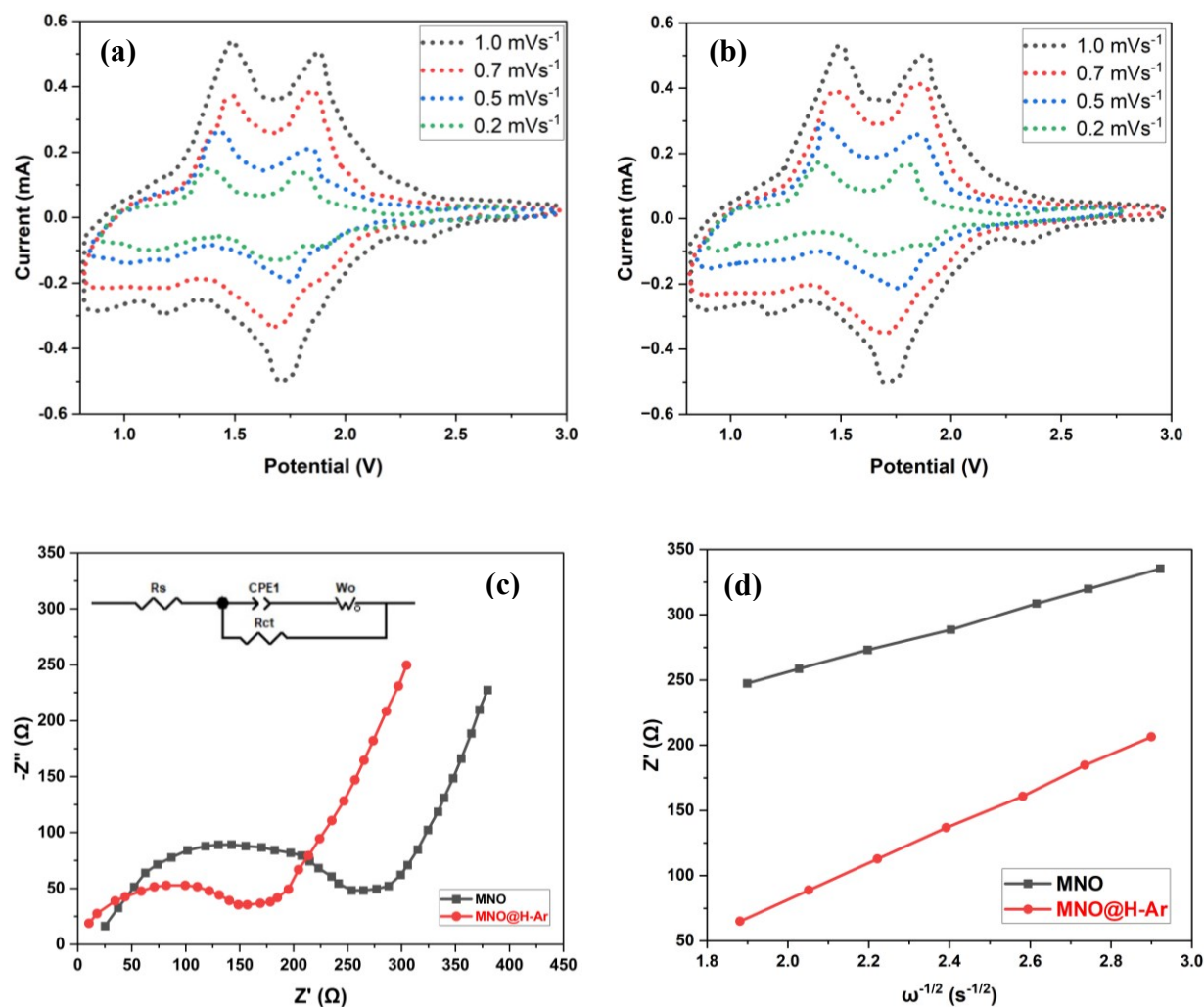


Figure 5-7: (a,b) CV curves of NMO and NMO@H-Ar at different scan rates; (c) Nyquist plots of NMO@H-Ar and NMO; (d) relationship between impedance and low-frequency region.

Furthermore, the lithium-ion diffusion coefficient and electronic conductivity of NMO and NMO@H-Ar electrodes were obtained from electrochemical impedance spectroscopy (EIS) analysis. The EIS results in Figures 5-7c and d show a semicircle in the medium to the high-frequency region and a diagonal line in the low-frequency region; these represent the charge transfer resistance ( $R_{ct}$ ) and Warburg diffusion process, respectively [196], [231]. According to the model circuit fitting and the fitting parameters shown in the inset of Figure 5-7c and Table S5-4 respectively, the NMO@H-Ar electrode has a significantly lower  $R_{ct}$  (52.7  $\Omega$ ) than the NMO electrode (165.2  $\Omega$ ); smaller  $R_{ct}$  values are advantageous for enhancing the lithium-ion mobility, electronic conductivity, and electrochemical performance of anode materials [50], [52], [70]. The large  $R_{ct}$  value obtained for NMO is also consistent with the wide band gap observed in the current UV-Vis absorption results. The wide band gap hinders the migration of electrons from the valence band to the conduction band in NMO, resulting in low electronic conductivity [180].

Lithium-ion mobility in the structure of a material is one of the critical factors determining its electrochemical performance as an anode material; this can be estimated using the EIS analysis. Based on the data obtained in the low-frequency region shown in Figure 5-7d, the lithium-ion diffusion coefficient of NMO and NMO@H-Ar was estimated using equations (5-4) (symbols and definitions are in the supporting information) [197].

$$D = \frac{2R^2T^2}{A^2n^4F^4C^2\sigma^2} \quad (5-4)$$

Consequently, the  $\text{Li}^+$  diffusion coefficient of NMO and NMO@H-Ar was estimated to be  $1.68 \times 10^{-14} \text{ cm}^2 \text{ s}^{-1}$  and  $7.18 \times 10^{-14} \text{ cm}^2 \text{ s}^{-1}$ , respectively. The values of the  $\text{Li}^+$  diffusion coefficient obtained from the EIS analysis are consistent with those calculated based on the CV

data. The results obtained from the EIS data are in agreement with the EPR and UV–Vis absorption results; this confirms that the electronic conductivity and lithium-ion diffusion coefficient of the NMO@H-Ar anode were greatly improved owing to the creation of oxygen vacancies in the material. These synergetic effects facilitated faster transportation of  $\text{Li}^+$  ions and electrons to the surface of NMO@H-Ar, resulting in the improved cycling stability and rate performance as a anode material [15].

#### **5.4. Conclusion**

In this study, NMO and NMO@H-Ar nanowires are successfully fabricated through an electrospinning technique followed by hydrogenation treatment under a mixture of 5% Hydrogen/Argon gas. The resulting nanowires were explored as anode materials for lithium-ion batteries. We found that the hydrogenation process did not alter the crystal structure, but expanded the unit cell volume and created abundant oxygen vacancies in the material. These resulted in a reduced band gap, enhanced lithium-ion mobility, and improved electronic conductivity. As a result of these improvements, the lithium-ion diffusion coefficient of NMO@H-Ar is enhanced by 4.2 times, as confirmed by EIS data. In addition, the overall electrochemical performances of NMO@H-Ar were significantly improved, including a superior initial reversible capacity of  $327 \text{ mAh g}^{-1}$  at 0.1 C compared to  $296 \text{ mAh g}^{-1}$  for NMO. In addition, NMO@H-Ar exhibits a remarkable cycling stability by retaining 94.4 % of its initial reversible capacity at a high current rate of 10 C, whereas NMO retained only 89.2 % under the same condition. These findings demonstrate the viability of hydrogenation treatment as a method of improving the intrinsic electronic conductivity, lithium-ion mobility, and overall electrochemical performance of a promising material for future anode for lithium-ion batteries.

## 5.5. Supporting Information

### Electrochemical performance of oxygen-vacant $\text{MoNb}_{12}\text{O}_{13}$ nanowires for lithium-ion battery anode

#### Symbol definitions for equations (3)

$I_p$  = peak current

$n$  = electron molecule concentration in the redox reactions

$A$  = surface area of the electrode

$C$  = bulk concentration of lithium ions

$v$  = the scan rate

$D$  = diffusion coefficient of lithium ions

#### Symbol definitions for equations (4)

$R$  = gas constant

$T$  = absolute temperature

$\sigma$  = Warburg factor

$A$  = surface area of the electrode

$n$  = electron molecule concentration in the redox reactions

$F$  = Faraday constant

$C$  = concentration of lithium ions

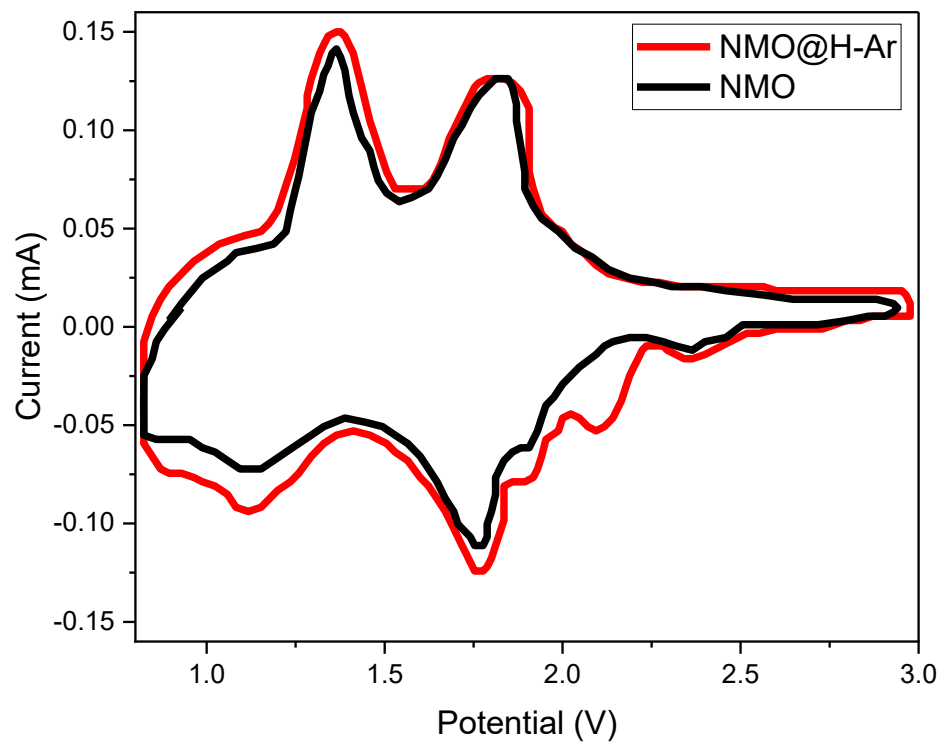


Figure S5-1: CV curve of NMO and NMO@H-Ar

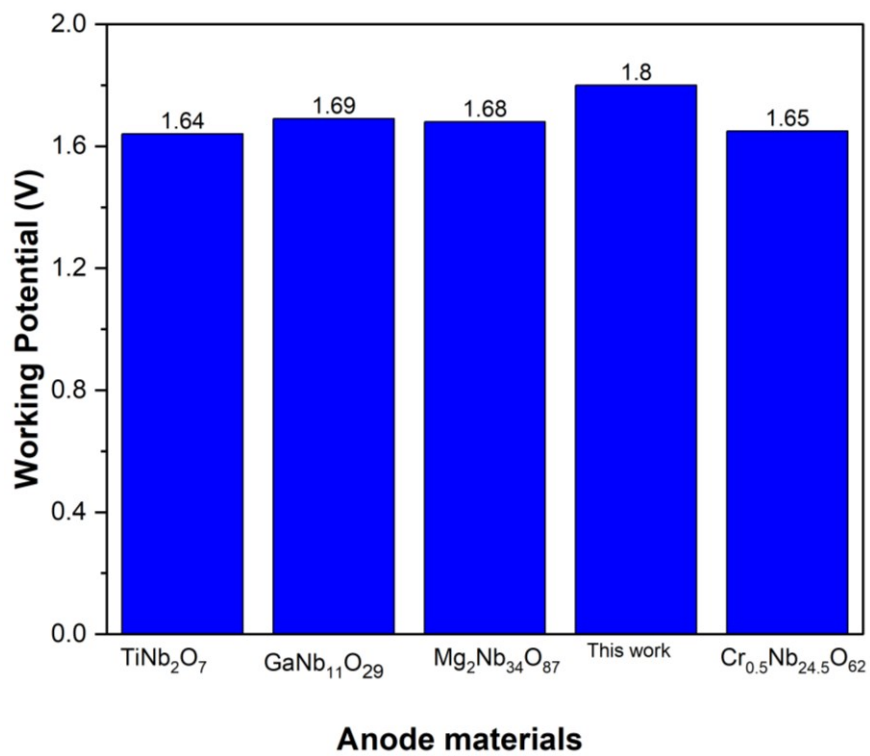


Figure S5-2: Average operating potential of Niobium-based anode materials

Table S5-1: Comparisons of reversible specific capacity of NMO and NMO@H-Ar with other niobate anode materials.

<b>materials</b>	<b>Specific capacity (mAh g<sup>-1</sup>)</b>	<b>Current rate (C)</b>	<b>References</b>
NMO@H-Ar	327	0.1 C	This work
NMO	296	0.1 C	This work
Cr <sub>0.5</sub> Nb <sub>24.5</sub> O <sub>62</sub> -N	344	0.1 C	[192]
Cr <sub>0.5</sub> Nb <sub>24.5</sub> O <sub>62</sub> -M	322	0.1 C	[192]
AlNb <sub>11</sub> O <sub>29</sub> -N	266	0.1 C	[193]
NMO@S	312	0.1 C	[40]
NMO@M	312	0.1 C	[40]
Mo <sub>3</sub> Nb <sub>14</sub> O <sub>44</sub> -M	323	0.1 C	[218]
Mo <sub>3</sub> Nb <sub>14</sub> O <sub>44</sub> -N	321	0.1 C	[218]
NMO@N	320	0.1 C	[50]
NMO@N	295	0.1 C	[50]
P-MoNb <sub>12</sub> O <sub>33</sub>	321	0.1 C	[196]
M-MoNb <sub>12</sub> O <sub>33</sub>	294	0.1 C	[196]
Mg <sub>2</sub> Nb <sub>34</sub> O <sub>87</sub> -P	338	0.1 C	[16]
Mg <sub>2</sub> Nb <sub>34</sub> O <sub>87</sub> -P	290	0.1 C	[16]
TiNb <sub>6</sub> O <sub>17</sub>	328	0.1 C	[229]
Graphite (NG)*	352		[200]

\* The reversible specific capacity of graphite was reported at current density of 0.2 mA cm<sup>-2</sup>

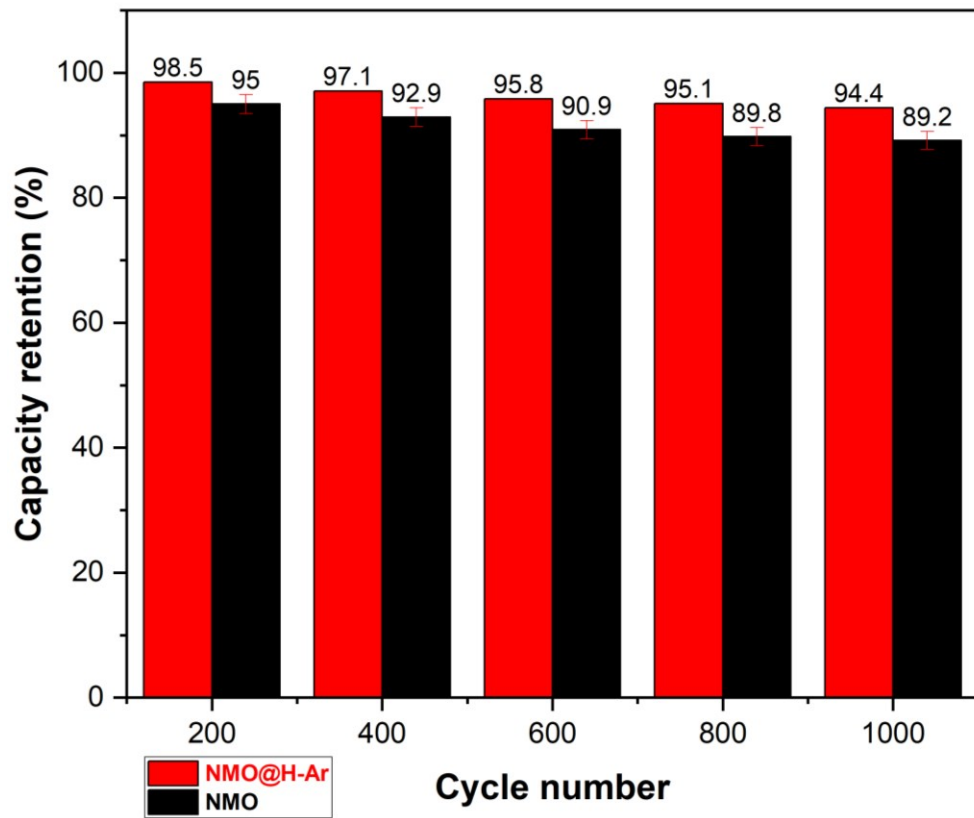


Figure S5-3: Capacity retention rate of NMO and NMO@H-Ar

Table S5-2: Comparisons of cycling performance of NMO and NMO@H-Ar with other niobate anode materials.

<b>Material</b>	<b>Capacity loss (%)</b>	<b>Capacity loss per cycle (%)</b>	<b>C-rate</b>	<b>Ref.</b>
NMO@H-Ar	5.6 % over 1000 cycles	0.0056	10 C	This work
NMO	10.8 % over 1000 cycles	0.0108	10 C	This work
GaNb <sub>11</sub> O <sub>29</sub> -N	12.6 % over 1000 cycles	0.0126	10 C	[8]
Cr <sub>0.5</sub> Nb <sub>24.5</sub> O <sub>62</sub> -N	7.2 % over 500 cycles	0.0144	10 C	[192]
AlNb <sub>11</sub> O <sub>29</sub> -N	6.8 % over 1000 cycles	0.0136	10 C	[193]
FeNb <sub>11</sub> O <sub>29</sub>	14.2 % over 1000 cycles	0.0142	10 C	[12]
TiNb <sub>2</sub> O <sub>7</sub>	14.5% over 500 cycles	0.0290	6 C	[67]
M-MoNb <sub>12</sub> O <sub>33</sub>	4.3 % over 500 cycles	0.0086	10 C	[196]
P-MoNb <sub>12</sub> O <sub>33</sub>	6.9 % over 500 cycles	0.0138	10 C	[196]
Mg <sub>2</sub> Nb <sub>34</sub> O <sub>87</sub> -P	6.5 % over 1000 cycles	0.0138	10 C	[16]
Mg <sub>2</sub> Nb <sub>34</sub> O <sub>87</sub> -M	6.5 % over 1000 cycles	0.0130	10 C	[16]
Cu <sub>0.02</sub> Ti <sub>0.94</sub> Nb <sub>2.04</sub> O <sub>7</sub>	2.7 % over 1000 cycles	0.0027	10 C	[15]
FeNb <sub>11</sub> O <sub>27.9</sub>	7.0 % Over 200 cycles	0.0350	10 C	[230]
FeNb <sub>11</sub> O <sub>29</sub>	11.2 % Over 200 cycles	0.0560	10 C	[230]
Graphite (NG)*	8.0% over 30 cycles	0.2700		[200]

\*Cycling performance of graphite was reported at current density of 0.2 mA cm<sup>-2</sup>

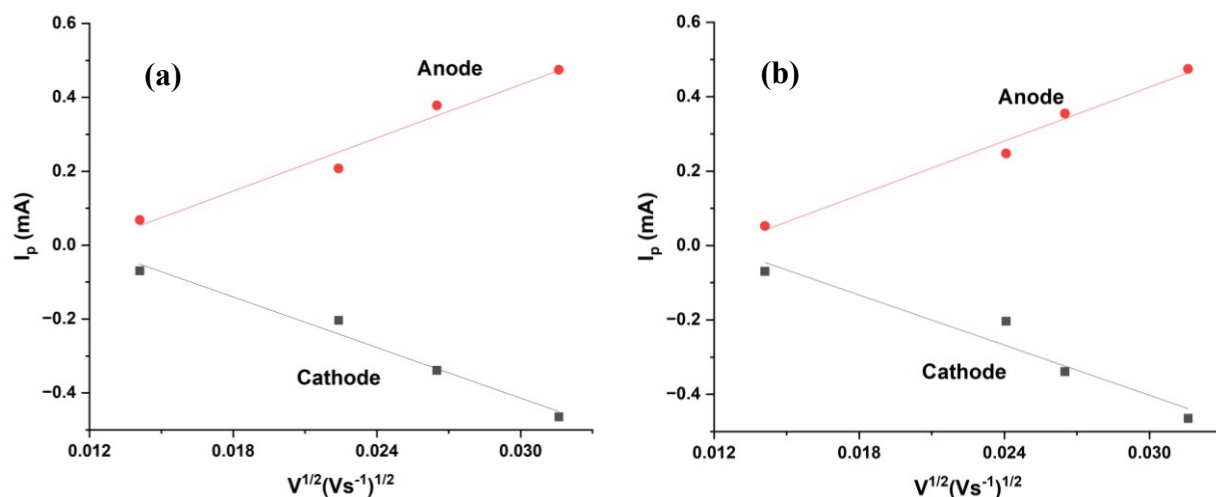


Figure S5-4: Relationships between peak current and the square root of the scan rate of (a) NMO and (b) NMO@H-Ar

Table S5-3: The Lithium-ion diffusion coefficients obtained from the CV curves.

Sample	$D$ ( $\text{cm}^2 \text{s}^{-1}$ )	
	Cathodic peak	Anodic peak
NMO	$1.14 \times 10^{-14}$	$1.27 \times 10^{-14}$
NMO@H-Ar	$8.74 \times 10^{-14}$	$7.59 \times 10^{-14}$

Table S5-4: Fitting parameters and diffusion coefficients obtained from EIS

Samples	$R_s$ ( $\Omega$ )	$R_{ct}$ ( $\Omega$ )	$D_{\text{Li}^+}$ ( $\text{cm}^2 \text{s}^{-1}$ )
NMO	5.4	165.2	$1.7 \times 10^{-14}$
NMO@H-Ar	3.9	52.7	$7.2 \times 10^{-14}$

## Chapter 6: Conclusions, Contributions, and Recommendations

The main findings of this thesis are highlighted in this chapter. The major contributions of this work in relation to other previous works and suggestions for future research are summarized.

### 6.1. Conclusions

The thesis focuses on the fabrication and performance enhancement of electrospun  $\text{Nb}_{18}\text{W}_{16}\text{O}_{93}$  and  $\text{MoNb}_{12}\text{O}_{33}$  nanowires for lithium-ion battery application. The results of investigations conducted by various authors affirmed that LIB anodes fabricated from nanowires demonstrated remarkable electrochemical properties owing to the unique architecture of nanowires. Previous studies established that the diameter of nanowires greatly influences the electrochemical performance of anode materials. For the first time, the influence of working parameters on electrospun  $\text{Nb}_{18}\text{W}_{16}\text{O}_{93}$  and  $\text{MoNb}_{12}\text{O}_{33}$  nanowires were successfully investigated. The work also explored doping and heat treatment as methods of enhancing the electrochemical performance of  $\text{Nb}_{18}\text{W}_{16}\text{O}_{93}$  and  $\text{MoNb}_{12}\text{O}_{33}$  nanowires for lithium-ion battery applications.

The influence of process parameters on the electrospinning of  $\text{Nb}_{18}\text{W}_{16}\text{O}_{93}$  oxide nanofibers was investigated and optimized using the response surface method. The predictive model developed using RSM, and CCD was found to be accurate and reliable for representing the diameter of the nanofibers. The reliability of the predictive model was assessed using ANOVA and linear correlation coefficient. The result of the ANOVA test performed on the model indicates that the applied voltage (V), spinning distance (D), polymer concentration (P), NaCl concentration (N), and other cross-factor interactions such as VD, DP, PF, PN, and  $P^2$  have a significant effect on the diameter of the nanofibers. The CCD method was utilized to optimize the process parameters. Under the optimum conditions of the applied voltage (24 kV), spinning

distance (20 cm), polymer concentration (8.5 wt.%), flow rate (1.7 ml hr<sup>-1</sup>), and NaCl concentration (0.8 wt.%), experimental nanofibers of 233 nm were obtained. This is very close to the 226 nm diameter predicted by the model. The influence of process parameters on the electrospinning of MoNb<sub>12</sub>O<sub>33</sub> nanofibers was also investigated using the same approach. The results obtained from the optimum process parameters, model verification, and ANOVA test were similar to Nb<sub>18</sub>W<sub>16</sub>O<sub>93</sub> nanofibers.

In the second part of the work, the effect of nickel doping content (1, 3, and 5 wt.%) on the morphology, structure, and electrochemical performance of Nb<sub>18</sub>W<sub>16</sub>O<sub>93</sub> was investigated. XRD analysis showed that the unit cell volume of 3 wt.% nickel-doped electrodes increased by 1.14%. This confirms that Ni<sup>2+</sup> ions were successfully incorporated into the crystal structure. The galvanostatic charge/discharge test results showed that all the nickel-doped electrodes exhibited improved initial discharge/charge capacity compared to the pristine sample. Furthermore, the 3 wt.% nickel-doped electrode exhibited a lower capacity loss of 6.9% at 5 C after 500 cycles compared to the capacity loss of 13.5% obtained for the undoped electrode. The EIS results further demonstrate that the nickel-doped samples exhibit superior electronic conductivity and lithium-ion diffusion coefficients. The remarkable electrochemical performance of nickel-doped Nb<sub>18</sub>W<sub>16</sub>O<sub>93</sub> electrodes was attributed to the generation of defects resulting from the lattice distortion and the introduction of *3d* energy levels within the band structure of the Nb<sub>18</sub>W<sub>16</sub>O<sub>93</sub> nanowires by nickel.

Finally, this study investigates the effect of heat treatment in the mixture of argon and hydrogen on the electrochemical performance of MoNb<sub>12</sub>O<sub>33</sub> nanowires. In the study, the electrospinning technique and subsequent hydrogenation treatment were employed for fabricating NMO and NMO@H-Ar nanowires. The hydrogenation process did not alter the

crystal structure but expanded the unit cell volume and created abundant oxygen vacancies in NMO@H-Ar. These resulted in a reduced band gap, enhanced lithium-ion mobility, and improved electronic conductivity. These resulted in high initial coulombic efficiency of 92.4 %, excellent long-term cycling stability with capacity retention of 94.4 % (capacity loss per cycle of 0.0056 %) after 1000 cycles at 10 C, and good rate performance of 179.7 mAh g<sup>-1</sup> at 10 C for NMO@H-Ar electrode. This confirms that the hydrogenation treatment greatly improved the electrochemical performance of MoNb<sub>12</sub>O<sub>33</sub>.

The results obtained from this study demonstrate that hydrogenation treatment and doping are efficient methods of improving the electrochemical kinetics and electronic conductivity of new anode materials for lithium-ion batteries. It is worth mentioning that the interconnected pores and surface area of nanowires also contributed to the improved electrochemical performance of the anode materials

## 6.2 Contributions

Due to the urgent need to develop high-performance and environmentally friendly lithium-ion batteries for energy storage, this study contributes to the ongoing efforts to fabricate an alternative anode material to replace graphite in the lithium-ion battery. In previous studies, Nb<sub>18</sub>W<sub>16</sub>O<sub>93</sub> and MoNb<sub>12</sub>O<sub>33</sub> nanowires were among the potential candidates identified to replace graphite as anode material for LIBs. However, their intrinsic low electronic conductivity still limits their practical application as anode materials for LIBs.

Electrospinning of ceramic nanowires is relatively new compared to that of polymer nanofibers, which have been well established. Thus, an in-depth understanding of the mechanisms controlling the morphology, diameter, and other properties of electrospun ceramic nanofibers is still vague, especially concerning Nb<sub>18</sub>W<sub>16</sub>O<sub>93</sub> and MoNb<sub>12</sub>O<sub>33</sub>. In the previous

studies,  $\text{Nb}_{18}\text{W}_{16}\text{O}_{93}$  and  $\text{MoNb}_{12}\text{O}_{33}$  nanowires were fabricated without determining the optimum conditions to obtain nanowires with reduced diameter. For the first time, this study investigated the influence of process parameters on the electrospinning of  $\text{Nb}_{18}\text{W}_{16}\text{O}_{93}$  and  $\text{MoNb}_{12}\text{O}_{33}$  nanofibers and generated model equations. The model equations generated from this study can be employed as a base for future studies on the reduction of ceramic nanofiber diameter within the range of the factors reported in the research.

Furthermore, previous studies on the electrochemical performance of  $\text{Nb}_{18}\text{W}_{16}\text{O}_{93}$  and  $\text{MoNb}_{12}\text{O}_{33}$  for LIB application established that the kinetics of electrochemical reactions in materials is hindered by their intrinsically poor electronic conductivity and electron transfer properties. This study successfully made the first attempt to improve the electronic conductivity and overall electrochemical performance of  $\text{Nb}_{18}\text{W}_{16}\text{O}_{93}$  and  $\text{MoNb}_{12}\text{O}_{33}$  through nickel doping and hydrogenation treatment.

Three journal articles were used in the body of the thesis (chapters 3, 4, and 5). In addition, three conference papers were presented during the study. They are listed as follows:

### **Journal papers**

- (1) **B. O. Fatile**, M. Pugh, and M. Medraj, "Optimization of the electrospun niobium–tungsten oxide nanofibers diameter using response surface methodology," *Nanomaterials*, vol. 11, 1644, 2021, doi:10.3390/nano11071644.
- (2) **B. O. Fatile**, M. Pugh, and M. Medraj, " Nickel-doped  $\text{Nb}_{18}\text{W}_{16}\text{O}_{93}$  nanowires with improved electrochemical properties for lithium-ion battery anodes," *Journal of Materials Chemistry and Physics*, vol. 307.

- (3) **B. O. Fatile**, M. Pugh, and M. Medraj, " Enhancing Niobium-Based Oxides for High-Performance Lithium Ion Batteries through Hydrogenation," *Journal of solid state electrochemistry*. <https://doi.org/10.1007/s10008-023-05644-1>.

### **Conference presentations**

- (1) **Fatile, B.O.**, Pugh, M., Medraj, M., "Electrospinning of niobium-tungsten oxide nanofibers," Canadian Society for Mechanical Engineering International Congress, 2020.
- (2) **Fatile, B.O.**, Pugh, M., Medraj, M., "Nickel-doped, niobium tungsten oxide nanowires as an anode material for lithium-ion batteries," 5th International Conference on Applied Surface Science, Spain, 2022.
- (3) **Fatile, B.O.**, Pugh, M., Medraj, M., "Electrochemical performance of yttrium-doped niobium molybdenum oxide nanowires for Li-ion batteries," Canadian Society for Mechanical Engineering International Congress, Edmonton, 2022.

### 6.3 Recommendations

The performance enhancement of  $\text{Nb}_{18}\text{W}_{16}\text{O}_{93}$  and  $\text{MoNb}_{12}\text{O}_{33}$  for Lithium-ion battery anode is complex due to the inherent poor electronic conductivity originating from their structural architecture. This study has successfully employed an electrospinning technique for fabricating  $\text{Nb}_{18}\text{W}_{16}\text{O}_{93}$  and  $\text{MoNb}_{12}\text{O}_{33}$  nanowires with reduced diameter and enhanced their electrochemical activities through doping and hydrogenation treatment. However, enhancing their reversible specific capacity and cycling performance is necessary. For this reason, there is still a need for more studies. The suggestions for future studies are as follows:

- This work has studied the influence of working parameters on the electrospinning of  $\text{Nb}_{18}\text{W}_{16}\text{O}_{93}$  and  $\text{MoNb}_{12}\text{O}_{33}$  and proposed models for determining the optimum conditions to fabricate ceramic nanofibers by considering only five factors. However, there are other factors (type of polymer, polymer molecular weight, collector's surface properties, and temperature) that can greatly influence the diameter and morphology of electrospun ceramic nanofibers. Therefore, an accurate model can be developed by considering other factors using a machine-learning approach.
- In this work, nickel doping was employed to enhance the electrochemical performance of  $\text{Nb}_{18}\text{W}_{16}\text{O}_{93}$  nanowires for LIB application. More studies are required to explore the possibility of using other elements such as rare earth metals. These metals possess complex electronic structures with partially filled 4 *f* or 5 *d* orbitals, this can strongly influence the electronic properties of the host materials thereby improving the electrochemical performance.
- The electrochemical performance of  $\text{MoNb}_{12}\text{O}_{33}$  has also been enhanced using the hydrogenation treatment without determining the conditions at which optimum

electrochemical properties can be achieved. For this reason, further studies can be carried out by considering different factors including annealing time and temperature to achieve optimum electrochemical properties using a design of experiment. The use of experimental design will provide a systematic approach in understanding the factors that significantly influence the electrochemical activities of the material.

- This present work focused solely on experimental studies. However, better results could be achieved using the combination of experimental and simulation. The use of software such as COMSOL Multiphysics will be beneficial in simulating the electrochemical dynamics of  $\text{Nb}_{18}\text{W}_{16}\text{O}_{93}$  and  $\text{MoNb}_{12}\text{O}_{33}$ .
- The lithium-ion diffusion coefficient was determined in this work using the Randles-Sevcik equation and EIS method. The use of galvanostatic intermittent titration technique (GIIT) for future research will be advantageous in studying the pseudocapacitance behavior of the anode materials.

## References

- [1] L. Yan, X. Rui, G. Chen, W. Xu, G. Zou, and H. Luo, "Recent advances in nanostructured Nb-based oxides for electrochemical energy storage," *Nanoscale*, vol. 8, no. 16, pp. 8443–8465, 2016, doi: 10.1039/C6NR01340F.
- [2] S. Sen and S. Ganguly, "Opportunities, barriers and issues with renewable energy development – A discussion," *Renew. Sustain. Energy Rev.*, vol. 69, pp. 1170–1181, Mar. 2017, doi: 10.1016/j.rser.2016.09.137.
- [3] R. Xia, C. Sun, Y. Wang, D. M. Cunha, H. Peng, K. Zhao, M. Huijben, and E. Johan, "Enhanced lithiation dynamics in nanostructured Nb<sub>18</sub>W<sub>16</sub>O<sub>93</sub> anodes," *J. Power Sources*, vol. 482, 228898, 2021, doi: 10.1016/j.jpowsour.2020.228898.
- [4] M. V. Reddy, A. Mauger, C. M. Julien, A. Paoletta, and K. Zaghib, "Brief history of early lithium-battery development," *Materials*, vol. 13, no. 8, p. 1884, 2020.
- [5] J. M. Tarascon and M. Armand, "Issues and challenges facing rechargeable lithium batteries," *Nature*, vol. 414, no. November, pp. 359–367, 2001, doi: 10.1142/9789814317665\_0024.
- [6] Y. Kim, Q. Jacquet, K. J. Griffith, J. Lee, S. Dey, B. L. Rinkel and C. P. Grey, "High rate lithium ion battery with niobium tungsten oxide anode high rate lithium ion battery with niobium tungsten oxide anode," *J. of The Electrochemical Society*, vol. 168, no. 1, 010525, 2021, doi: 10.1149/1945-7111/abd919.
- [7] Q. Fu, X. Liu, J. Hou, Y. Pu, C. Lin, L. Yang, X. Zhu, L. Hu, S. Lin, L. Luo, and Y. Chen, "Highly conductive CrNb<sub>11</sub>O<sub>29</sub> nanorods for use in high-energy, safe, fast-charging and stable lithium-ion batteries," *J. Power Sources*, vol. 397, pp. 231–239, 2018, doi: 10.1016/j.jpowsour.2018.07.020.

- [8] X. Lou, Q. Fu, J. Xu, X. Liu, C. Lin, J. Han, Y. Luo, Y. Chen, X. Fan, and J. Li, "GaNb<sub>11</sub>O<sub>29</sub> nanoweb as high-performance anode materials for lithium-ion batteries," *ACS Appl. Nano Mater.*, vol. 1, no. 1, pp. 183–190, 2018, doi: 10.1021/acsanm.7b00091.
- [9] X. Wu, K. Song, X. Zhang, N. Hu, L. Li, and W. Li, "Safety Issues in Lithium Ion Batteries : Materials and Cell Design," vol. 7, no. July, pp. 1–17, 2019, doi: 10.3389/fenrg.2019.00065.
- [10] W. Liu, M. Xu, and M. Zhu, "Design of a niobium tungsten oxide/C micro-structured electrode for fast charging lithium-ion batteries," *Inorg. Chem. Front.*, vol. 8, no. 17, pp. 3998–4005, 2021, doi: 10.1039/D1QI00587A.
- [11] Y.-S. Lee and K.-S. Ryu, "Study of the lithium diffusion properties and high rate performance of TiNb<sub>6</sub>O<sub>17</sub> as an anode in lithium secondary battery," *Sci. Rep.*, vol. 7, no. 1, p. 16617, Nov. 2017, doi: 10.1038/s41598-017-16711-9.
- [12] J. Huang, Q. Chen, S. Chen, L. Luo, J. Li, C. Lin, and Y. Chen, "Al<sup>3+</sup> - doped FeNb<sub>11</sub>O<sub>29</sub> anode materials with enhanced lithium - storage performance," *Advanced Composites and Hybrid Materials*, vol. 4, no 3, pp. 733–742, 2021, doi.org/10.1007/s42114-021-00291-4.
- [13] M. Bini, I. Quinzeni, and D. Spada, "The doping of FeNb<sub>11</sub>O<sub>29</sub> as a way to improve its electrochemical performances," *Chemistry Select*, vol. 4, no. 19, pp. 5656–5661, 2019, doi: 10.1002/slct.201901182.
- [14] C. H. Lu, P. Kulkarni, S. Balaji, and P. S. Kumar, "Exploration of electrochemical and lithium transport properties of BaNb<sub>3.6</sub>O<sub>10</sub> as an anode material for lithium-ion batteries," *J. Alloys Compd.*, vol. 830, 154306, 2020, doi: 10.1016/j.jallcom.2020.154306.
- [15] C. Yang, C. Lin, S. Lin, Y. Chen, and J. Li, "Cu<sub>0.02</sub>Ti<sub>0.94</sub>Nb<sub>2.04</sub>O<sub>7</sub>: An advanced anode

- material for lithium-ion batteries of electric vehicles," *J. Power Sources*, vol. 328, pp. 336–344, 2016, doi: 10.1016/j.jpowsour.2016.08.027.
- [16] X. Zhu, Q. Fu, L. Tang, C. Lin, J. Xu, G. Liang, R. Li, L. Lou, and Y. Chen, "Mg<sub>2</sub>Nb<sub>34</sub>O<sub>87</sub> porous microspheres for use in high-energy, safe, fast-charging, and stable lithium-ion batteries," *ACS Appl. Mater. Interfaces*, vol. 10, no. 28, pp. 23711–23720, 2018, doi: 10.1021/acsami.8b03997.
- [17] Q. Fu, R. Li, X. Zhu, G. Liang, and L. Luo, "Design, synthesis and lithium-ion storage capability of Al<sub>0.5</sub>Nb<sub>24.5</sub>O<sub>62</sub>," *J. Mater. Chem. A*, vol. 7, pp. 19862–19871, 2019, doi: 10.1039/C9TA04644E.
- [18] E. Kamali-Heidari, A. Kamyabi-Gol, M. Heydarzadeh sohi, and A. Ataie, "Electrode materials for lithium ion batteries: A review," *J. Ultrafine Grained Nanostructured Mater.*, vol. 51, no. 1, pp. 1-12, 2018, doi: 10.22059/jufgnsm.2018.01.01.
- [19] Y. Liang, H. Dong, D. Aurbach, and Y. Yao, "Current status and future directions of multivalent metal-ion batteries," *Nat. Energy*, vol. 5, no. 9, pp. 646–656, 2020, doi: 10.1038/s41560-020-0655-0.
- [20] S. S. Zhang, "A review on the separators of liquid electrolyte Li-ion batteries," *J. Power Sources*, vol. 164, no. 1, pp. 351–364, 2007, doi: 10.1016/j.jpowsour.2006.10.065.
- [21] X. Jiang X. Jiang, C. Yanjun, M. Xiaokai, C. Weiguo, L. Changcheng, H. Que, N. Nithesh, M. Vignesh, H. Mina, and G. Zhanhu., "The impact of electrode with carbon materials on safety performance of lithium-ion batteries: A review," *Carbon*, vol. 191, pp. 448–470, 2022, doi: 10.1016/j.carbon.2022.02.011.

- [22] Y. Mekonnen, A. Sundararajan, and A. I. Sarwat, “A review of cathode and anode materials for lithium-ion batteries,” in *SoutheastCon 2016*, Norfolk, VA, USA: IEEE, 2016, pp. 1–6. doi: 10.1109/SECON.2016.7506639.
- [23] M. S. Whittingham, “Lithium batteries and cathode materials,” *Chem. Rev.*, vol. 104, no. 10, pp. 4271–4302, 2004, doi: 10.1021/cr020731c.
- [24] J. W. Fergus, “Recent developments in cathode materials for lithium ion batteries,” *J. Power Sources*, vol. 195, no. 4, pp. 939–954, 2010, doi: 10.1016/j.jpowsour.2009.08.089.
- [25] J. Du, L. Qingmeng, C. Jiali, J. Lei, Z. Qianqian, H. Ning, Z. Wei, and T. Bohejin, “Review of metal oxides as anode materials for lithium-ion batteries,” *Dalton Trans.*, vol. 51, no. 25, pp. 9584–9590, 2022, doi: 10.1039/D2DT01415G.
- [26] H. Yoo, J.-I. Lee, H. Kim, J.-P. Lee, J. Cho, and S. Park, “Helical Silicon/Silicon Oxide Core–Shell Anodes Grown onto the Surface of Bulk Silicon,” *Nano Lett.*, vol. 11, no. 10, pp. 4324–4328, Oct. 2011, doi: 10.1021/nl202417c.
- [27] J. Lu, Z. Chen, F. Pan, Y. Cui, and K. Amine, “High-Performance Anode Materials for Rechargeable Lithium-Ion Batteries,” *Electrochem. Energy Rev.*, vol. 1, no. 1, pp. 35–53, 2018, doi: 10.1007/s41918-018-0001-4.
- [28] F. Ma, A. Yuan, and J. Xu, “Nanoparticulate  $Mn_3O_4$  /VGCF composite conversion-anode material with extraordinarily high capacity and excellent rate capability for lithium ion batteries,” *ACS Appl. Mater. Interfaces*, vol. 6, no. 20, pp. 18129–18138, 2014, doi: 10.1021/am505022u.
- [29] G. Wang, M. Zhang, Z. Deng, X. Zhang, L. Huo, and S. Gao, “Poplar branch bio-template synthesis of mesoporous hollow  $Co_3O_4$  hierarchical architecture as an anode for long-life

- lithium ion batteries,” *Ceram. Int.*, vol. 46, no. 18, pp. 29033–29040, 2020, doi: 10.1016/j.ceramint.2020.08.074.
- [30] P. Subalakshmi and A. Sivashanmugam, “CuO nano hexagons, an efficient energy storage material for Li- ion battery application,” *J. Alloys Compd.*, vol. 690, pp. 523–531, 2017, doi: 10.1016/j.jallcom.2016.08.157.
- [31] M. S. Akhtar P. T. Bui, Z. Y. Li, O. B. Yang, B. J. Paul, S. Kim, J. Kim, and A.K Rai, “Impact of porous Mn<sub>3</sub>O<sub>4</sub> nanostructures on the performance of rechargeable lithium ion battery: Excellent capacity and cyclability,” *Solid State Ion.*, vol. 336, pp. 31–38, 2019, doi: 10.1016/j.ssi.2019.03.010.
- [32] C.-L. Liu, Y. Wang, C. Zhang, X.-S. Li, and W.-S. Dong, “In situ synthesis of  $\alpha$ -MoO<sub>3</sub>/graphene composites as anode materials for lithium ion battery,” *Mater. Chem. Phys.*, vol. 143, no. 3, pp. 1111–1118, 2014, doi: 10.1016/j.matchemphys.2013.11.011.
- [33] Y. Dong, Y. Feng, J. Deng, P. He, and J. Ma, “Electrospun Sb<sub>2</sub>Se<sub>3</sub>@C nanofibers with excellent lithium storage properties,” *Chin. Chem. Lett.*, vol. 31, no. 3, pp. 909–914, 2020, doi: 10.1016/j.ccllet.2019.11.039.
- [34] X. Li, P. Yan, X. Xiao, J. H. Woo, C. Wang, J. Liu, and J. H. Zhang, “Design of porous Si/C–graphite electrodes with long cycle stability and controlled swelling,” *Energy Environ. Sci.*, vol. 10, no. 6, pp. 1427–1434, 2017, doi: 10.1039/C7EE00838D.
- [35] M. Deng, S. Li, W. Hong, Y. Jiang, W. Xu, H. Shuai, G. Zou, Y. Hu, H. Hou, W. Wang, and X. Ji, “Octahedral Sb<sub>2</sub>O<sub>3</sub> as high-performance anode for lithium and sodium storage,” *Mater. Chem. Phys.*, vol. 223, pp. 46–52, 2019, doi: 10.1016/j.matchemphys.2018.10.043.

- [36] J. Liang, X. Li, Z. Hou, W. Zhang, Y. Zhu, and Y. Qian, "A deep reduction and partial oxidation strategy for fabrication of mesoporous Si anode for lithium ion batteries," *ACS Nano*, vol. 10, no. 2, pp. 2295–2304, 2016, doi: 10.1021/acsnano.5b06995.
- [37] L. Yin, S. Chai, F. Wang, J. Huang, J. Li, C. Liu, and X. Kong, "Ultrafine SnO<sub>2</sub> nanoparticles as a high performance anode material for lithium ion battery," *Ceram. Int.*, vol. 42, no. 8, pp. 9433–9437, 2016, doi: 10.1016/j.ceramint.2016.02.173.
- [38] C. Liu, Y. Zhao, R. Yi, Y. Sun, Y. Li, L. Yang, I. Mitrovic, S. Taylor, P. Chalker, and C. Zhao, "Alloyed Cu/Si core-shell nanoflowers on the three-dimensional graphene foam as an anode for lithium-ion batteries," *Electrochimica Acta*, vol. 306, pp. 45–53, 2019, doi: 10.1016/j.electacta.2019.03.071.
- [39] Y. Wang, M. Wu, and W. F. Zhang, "Preparation and electrochemical characterization of TiO<sub>2</sub> nanowires as an electrode material for lithium-ion batteries," *Electrochimica Acta*, vol. 53, no. 27, pp. 7863–7868, 2008, doi: 10.1016/j.electacta.2008.05.068.
- [40] X. Ma, P. Chen, M. Qian, D. Wu, J. Du, X. Chen, R. Dai, M. Sha, Z. Zi, and J. Dai, "Rod-like Nb<sub>14</sub>Mo<sub>3</sub>O<sub>44</sub> nanoparticles fabricated by a facile solvothermal method as novel anode for lithium-ion batteries," *J. Alloys Compd.*, vol. 864, pp. 158379, 2021, doi: 10.1016/j.jallcom.2020.158379.
- [41] Q. Zhu, J. Jiang, Z. Li, Y. Xu, H. Dou, and X. Zhang, "Electrospinning oxygen-vacant TiNb<sub>24</sub>O<sub>62</sub> nanowires simultaneously boosts electrons and ions transmission capacities toward superior lithium storage," *Electrochimica Acta*, vol. 388, p. 138656, 2021, doi: 10.1016/j.electacta.2021.138656.

- [42] S. Li, Q. Xu, E. Uchaker, X. Cao, and G. Cao, "Comparison of amorphous, pseudohexagonal and orthorhombic Nb<sub>2</sub>O<sub>5</sub> for high-rate lithium ion insertion," *CrystEngComm*, vol. 18, no. 14, pp. 2532–2540, 2016, doi: 10.1039/C5CE02069G.
- [43] J. B. Felder, W. Wong-Ng, R. A. Qabbani, R. S. Roth, B. H. Toby, and J. Y. Chan, "Structural investigation of the 'tripled-tetragonal-tungsten-bronze' phases Sr<sub>2</sub>M<sub>10</sub>O<sub>27</sub> (M = Nb, Ta)," *Polyhedron*, vol. 170, pp. 359–363, Sep. 2019, doi: 10.1016/j.poly.2019.06.003.
- [44] R. Ab Kadir, R. A. Rani, M.M. Alsaif, J. Z. Ou, W. Wlodarski, A. P. O'Mullane, K. Kalantar-Zadeh, "Optical gas sensing properties of nanoporous Nb<sub>2</sub>O<sub>5</sub> Films," *ACS Appl. Mater. Interfaces*, vol. 7, no. 8, pp. 4751–4758, 2015, doi: 10.1021/am508463g.
- [45] S. Qi, R. Zuo, Y. Liu, and Y. Wang, "Synthesis and photocatalytic activity of electrospun niobium oxide nanofibers," *Mater. Res. Bull.*, vol. 48, no. 3, pp. 1213–1217, 2013, doi: 10.1016/j.materresbull.2012.11.074.
- [46] C. Wu, Z. Shao, W. Zhai, X. Zhang, C. Zhang, C. Zhu, Y. Yu, and W. Liu, "Niobium tungsten oxides for electrochromic devices with long-term stability," *ACS Nano*, vol. 16, no. 2, pp. 2621–2628, 2022, doi: 10.1021/acsnano.1c09234.
- [47] W. Ye, H. Yu, X. Cheng, H. Zhu, R. Zheng, T. Liu, N. Long, M. Shui, and J. Shu, "Highly efficient lithium container based on non-Wadsley-Roth structure Nb<sub>18</sub>W<sub>16</sub>O<sub>93</sub> nanowires for electrochemical energy storage," *Electrochem. Acta*, vol. 292, pp. 331–338, 2018., doi: 10.1016/j.electacta.2018.09.169.
- [48] C. P. Koçer, K. J. Griffith, C. P. Grey, and A. J. Morris, "Cation disorder and lithium insertion mechanism of wadsley–roth crystallographic shear phases from first principles," *J. Am. Chem. Soc.*, vol. 141, no. 38, pp. 15121–15134, 2019, doi: 10.1021/jacs.9b06316.
- [49] L. Yan, J. Shu, C. Li, X. Cheng, H. Zhu, H. Yu, C. Zhang, Y. Zheng, Y. Xie,

- and Z. Guo, "W<sub>3</sub>Nb<sub>14</sub>O<sub>44</sub> nanowires: ultrastable lithium storage anode materials for advanced rechargeable batteries," *Energy Storage Mater.*, vol. 16, pp. 535-544, 2019., doi: 10.1016/j.ensm.2018.09.008.
- [50] X. Ma, C. Yu, X. Cao, J. Hu, N. Cheng, H. Chen, P. Chen, Y. Guo, J. Chen, Z. Zi, and J. Dai, "Novel Nb<sub>26</sub>Mo<sub>4</sub>O<sub>77</sub> rod-like nanoparticles anode with enhanced electrochemical performances for lithium-ion batteries," *J. Alloys Compd.*, vol. 890, 161853, 2022, doi: 10.1016/j.jallcom.2021.161853.
- [51] X. Fang, C. Rong, L. Zhou, C. Yin, L. He, H. Cui, F. Lu, and X. Kuang, "Enhanced lithium storage in micrometer-scale tungsten bronze Mo<sub>3</sub>Nb<sub>2</sub>O<sub>14</sub> by molybdenum reduction and oxygen deficiency," *Adv. Mater. Interfaces*, vol. 8, no. 24, 2101016, 2021, doi: 10.1002/admi.202101016.
- [52] Z. Deng, S. Shi, P. Mou, C. Du, G. Wan, and G. Wang, "A lamellar MoNb<sub>12</sub>O<sub>33</sub> as the high-rate anode material for lithium-ion batteries," *J. Electron. Mater.*, vol. 51, no. 8, pp. 4125–4132, 2022, doi: 10.1007/s11664-022-09706-4.
- [53] S.-Y. Lee, A. S. Lim, Y. M. Kwon, K. Y. Cho, and S. Yoon, "Copper, zinc, and manganese niobates (CuNb<sub>2</sub>O<sub>6</sub>, ZnNb<sub>2</sub>O<sub>6</sub>, and MnNb<sub>2</sub>O<sub>6</sub>): structural characteristics, Li<sup>+</sup> storage properties, and working mechanisms," *Inorg. Chem. Front.*, vol. 7, no. 17, pp. 3176–3183, 2020, doi: 10.1039/D0QI00475H.
- [54] X. Cai, H. Yan, Z. Yang, W. Li, H. Yu, L. Yan, L. Zhang, M. Shui, Y. Cui, and J. Shu, "Copper niobate nanowires boosted by a N, S co-doped carbon coating for superior lithium storage," *Dalt. Trans.*, vol. 50, no. 32, pp. 11030–11038, 2021, doi: 10.1039/d1dt01834e.

- [55] Y. Lu, L. Yu, and X. W. D. Lou, “Nanostructured conversion-type anode materials for advanced lithium-ion batteries,” *Chem*, vol. 4, no. 5, pp. 972–996, 2018.
- [56] D. Liu and G. Cao, “Engineering nanostructured electrodes and fabrication of film electrodes for efficient lithium ion intercalation,” *Energy Environ. Sci.*, vol. 3, no. 9, p. 1218, 2010, doi: 10.1039/b922656g.
- [57] Y. Yang and J. Zhao, “wadsley–roth crystallographic shear structure niobium-based oxides: promising anode materials for high-safety lithium-ion batteries,” *Adv. Sci.*, vol. 8, no. 12, p. 2004855, 2021, doi: 10.1002/advs.202004855.
- [58] J. Zhao, D. Wei, X. Zhang, S. Zhang, C. Zhang, and X. Yang, “Biomass-derived hierarchical N, P codoped porous 3D-carbon framework@TiO<sub>2</sub> hybrids as advanced anode for lithium ion batteries,” *J. Colloid Interface Sci.*, vol. 606, pp. 577–587, 2022, doi: 10.1016/j.jcis.2021.08.005.
- [59] Y. Wang, Y. Li, Z. Qiu, X. Wu, P. Zhou, T. Zhou, J. Zhao, Z. Miao, J. Zhou, and S. Zhou “Fe<sub>3</sub>O<sub>4</sub> @Ti<sub>3</sub>C<sub>2</sub> MXene hybrids with ultrahigh volumetric capacity as an anode material for lithium-ion batteries,” *J. Mater. Chem. A*, vol. 6, no. 24, pp. 11189–11197, 2018, doi: 10.1039/C8TA00122G.
- [60] L. Xu, Y. Hu, H. Zhang, H. Jiang, and C. Li, “Confined synthesis of FeS<sub>2</sub> nanoparticles encapsulated in carbon nanotube hybrids for ultrastable lithium-ion batteries,” *ACS Sustain. Chem. Eng.*, vol. 4, no. 8, pp. 4251–4255, 2016, doi: 10.1021/acssuschemeng.6b00741.
- [61] J. Zhou, Y. You, X. Lian, Q. Shi, Y. Liu, X. Yang, A. Bachmatiuk, L. Liu, J. Sun, R. Yang, and J. H. Choi, “Toward stable lithium-ion batteries: Accelerating the transfer and alloying reactions of Sn-based anodes via coordination atom regulation and carbon hybridization,” *J. Power Sources*, vol. 519, p. 230778, 2022, doi: 10.1016/j.jpowsour.2021.230778.

- [62] L. Zhou, K. Zhang, Z. Hu, Z. Tao, L. Mai, Y. M. Kang, S. L. Chou and J. Chen, "Recent developments on and prospects for electrode materials with hierarchical structures for lithium-ion batteries," *Adv. Energy Mater.*, vol. 8, no. 6, pp. 1–23, 2018, doi: 10.1002/aenm.201701415.
- [63] J. Xiao, J. Zheng, X. Li, Y. Shao, and J.-G. Zhang, "Hierarchically structured materials for lithium batteries," *Nanotechnology*, vol. 24, no. 42, p. 424004, Oct. 2013, doi: 10.1088/0957-4484/24/42/424004.
- [64] H. Wang *et al.*, "Structural and electrochemical characteristics of hierarchical Li<sub>4</sub>Ti<sub>5</sub>O<sub>12</sub> as high-rate anode material for lithium-ion batteries," *Electrochimica Acta*, vol. 368, p. 137470, Feb. 2021, doi: 10.1016/j.electacta.2020.137470.
- [65] H. Jia, X. Li, J. Song, X. Zhang, L. Luo, Y. He, B. Li, Y. Cai, S. Hu, X. Xiao, and C. Wang, "Hierarchical porous silicon structures with extraordinary mechanical strength as high-performance lithium-ion battery anodes," *Nat. Commun.*, vol. 11, no. 1, pp. 1–9, 2020, doi: 10.1038/s41467-020-15217-9.
- [66] X. Han, Q. Meng, X. Wan, B. Sun, Y. Zhang, B. Shen, J. Gao, Y. Ma, P. Zuo, S. Lou, and G. Yin, "Intercalation pseudocapacitive electrochemistry of Nb-based oxides for fast charging of lithium-ion batteries," *Nano Energy*, vol. 81, no. November 2020, p. 105635, 2021, doi: 10.1016/j.nanoen.2020.105635.
- [67] Y. Hsiao, C. Chang-jian, H. Chu, H. Chiang, C. Chen, and J. Huang, "Applied Surface Science Doping with W<sup>6+</sup> ions enhances the performance of TiNb<sub>2</sub>O<sub>7</sub> as an anode material for lithium-ion batteries," *Applied Surface Sci.*, vol. 573, 151517, 2022, doi: 10.1016/j.apsusc.2021.151517.
- [68] A. Sadeghzadeh-Attar and M. R. Bafandeh, "The effect of annealing temperature on the

- structure and optical properties of well-aligned 1D SnO<sub>2</sub> nanowires synthesized using template-assisted deposition," *Cryst. Eng. Comm.*, vol. 20, no. 4, pp. 460–469, 2018, doi: 10.1039/c7ce01815k.
- [69] J. Zhang, H. Jiang, Y. Zeng, Y. Zhang, and H. Guo, "Oxygen-defective Co<sub>3</sub>O<sub>4</sub> for pseudo-capacitive lithium storage," *J. Power Sources*, vol. 439, 227026, 2019, doi: 10.1016/j.jpowsour.2019.227026.
- [70] Y. Zhang, M. Zhang, Y. Liu, H. Zhu, L. Wang, Y. Liu, M. Xue, B. Li, and X. Tao, "Oxygen vacancy regulated TiNb<sub>2</sub>O<sub>7</sub> compound with enhanced electrochemical performance used as anode material in Li-ion batteries," *Electrochim. Acta*, vol. 330, 135299, 2020, doi: 10.1016/j.electacta.2019.135299.
- [71] P. Heitjans and S. Indris, "Diffusion and ionic conduction in nanocrystalline ceramics," *J. Phys. Condens. Matter*, vol. 15, no. 30, pp. 1257–1289, 2003, doi: 10.1088/0953-8984/15/30/202.
- [72] F. Ran, X. Cheng, H. Yu, R. Zheng, T. Liu, X. Li, N. Ren, M. Shui, and J. Shu, "Nano-structured GeNb<sub>18</sub>O<sub>47</sub> as novel anode host with superior lithium storage performance," *Electrochim. Acta*, vol. 282, pp. 634–641, 2018, doi: 10.1016/j.electacta.2018.06.109.
- [73] W. Wang, M. Zhang, R. Mi, Y. Liu, and J. Chen, "Facile synthesis of porous Co<sub>3</sub>O<sub>4</sub> nanosheets containing abundant oxygen vacancies for boosted lithium-ion storage," *J. Alloys Compd.*, vol. 888, 161615, 2021, doi: 10.1016/j.jallcom.2021.161615.
- [74] X. Cheng, S. Qian, H. Yu, H. Zhu, Y. Xie, R. Zheng, T. Liu, M. Shui, and J. Shu, "BaNb<sub>3.6</sub>O<sub>10</sub> nanowires with superior electrochemical performance towards ultrafast and highly stable lithium storage," *Energy Storage Mater.*, vol. 16, pp. 400–410, 2019, doi: 10.1016/j.ensm.2018.06.018.

- [75] Y. Li, R. Zheng, H. Yu, X. Cheng, T. Liu, N. Peng, J. Zhang, M. Shui, and J. Shu, "Observation of  $ZrNb_{14}O_{37}$  nanowires as a lithium container via in situ and ex situ techniques for high-performance lithium-ion batteries," *ACS Appl. Mater. Interfaces*, vol. 11, no. 25, pp. 22429–22438, 2019, doi: 10.1021/acsami.9b05841.
- [76] Y. D. Xia, P. D. Yang, Y. G. Sun, Y. Y. Wu, B. Mayers, B. Gates, Y. D. Yin, F. Kim, and Y. Q. Yan, "One-Dimensional Nanostructures: Synthesis, Characterization, and Applications," *Adv. Mater.*, vol. 15, no. 5, pp. 353–389, 2003, doi: 10.1002/adma.200390087.
- [77] A. I. Hochbaum and P. Yang, "Semiconductor Nanowires for energy conversion," *Chem. Rev.*, vol. 110, no. 1, pp. 527–546, 2010, doi: 10.1021/cr900075v.
- [78] C. N. R. Rao, F. L. Deepak, G. Gundiah, and A. Govindaraj, "Inorganic nanowires," *Prog. Solid State Chem.*, vol. 31, no. 1–2, pp. 5–147, 2003, doi: 10.1016/j.progsolidstchem.2003.08.001.
- [79] J. Sarkar, G. G. Khan, and A. Basumallick, "Nanowires: properties, applications and synthesis via porous anodic aluminium oxide template," *Bull. Mater. Sci.*, vol. 30, no. 3, pp. 271–290, 2007, doi: 10.1007/s12034-007-0047-0.
- [80] H. Esfahani, R. Jose, and S. Ramakrishna, "Electrospun ceramic nanofiber mats today: synthesis, properties, and applications," *Materials*, vol. 10, no. 11, p. 1238, 2017, doi: 10.3390/ma10111238.
- [81] T. F. Yi, S. Y. Yang, and Y. Xie, "Recent advances of  $Li_4Ti_5O_{12}$  as a promising next generation anode material for high power lithium-ion batteries," *J. Mater. Chem. A*, vol. 3, no. 11, pp. 5750–5777, 2015, doi: 10.1039/C4TA06882C.

- [82] J. Weber, R. Singhal, S. Zekri, and A. Kumar, "One-dimensional nanostructures: fabrication, characterisation and applications," *Int. Mater. Rev.*, vol. 53, no. 4, pp. 235–255, 2008, doi: 10.1179/174328008X348183.
- [83] J. Bhagwan, N. Kumar, and Y. Sharma, Fabrication, characterization, and optimization of  $Mn_xO_y$  nanofibers for improved supercapacitive properties. *Elsevier Inc.*, 451-481, 2019.
- [84] M. S. Dresselhaus, Y. Lin, O. Rabin, M. R. Black, J. Kong, and G. Dresselhaus, "Nanowires," *In Springer handbook of nanotechnology*, 2010, pp. 119–167. doi: 10.1007/978-3-642-02525-9\_4.
- [85] S. Z. Qiao, J. Liu, G. Qing, and M. Lu, "Chapter 21 - Synthetic Chemistry of Nanomaterials," in *Modern Inorganic Synthetic Chemistry*, R. Xu, W. Pang, and Q. Huo, Eds., Amsterdam: Elsevier, 2011, pp. 479–506. doi: 10.1016/B978-0-444-53599-3.10021-6.
- [86] Q. Wei, F. Xiong, S. Tan, L. Huang, E. H. Lan, B. Dunn and L. Mai, "Porous one-dimensional nanomaterials : Design , fabrication and applications in electrochemical energy storage," *Adv. mater.*, vol. 29, no 20, 1602300, 2017, doi: 10.1002/adma.201602300.
- [87] X. M. Liu and Y. C. Zhou, "Electrochemical deposition and characterization of  $Cu_2O$  nanowires," *Appl. Phys. A*, vol. 81, no. 4, pp. 685–689, 2005, doi: 10.1007/s00339-005-3243-z.
- [88] Q. G. Fu, H. J. Li, X. H. Shi, K. Z. Li, J. Wei, and Z. B. Hu, "Synthesis of silicon carbide nanowires by CVD without using a metallic catalyst," *Mater. Chem. Phys.*, vol. 100, no. 1, pp. 108–111, 2006, doi: 10.1016/j.matchemphys.2005.12.014.
- [89] F. Khosrow-pour, M. Aghazadeh, B. Sabour, and S. Dalvand, "Large-scale synthesis of uniform lanthanum oxide nanowires via template-free deposition followed by heat-

- treatment,” *Ceram. Int.*, vol. 39, no. 8, pp. 9491–9498, 2013, doi: 10.1016/j.ceramint.2013.05.067.
- [90] Z. Miao, D. Xu, J. Ouyang, G. Guo, and X. Zhao, "Electrochemically induced sol – gel preparation of single-crystalline TiO<sub>2</sub> nanowires," *Nano Letters*, vol. 2, no. 7, pp. 717-720 2002.
- [91] R. S. Wagner and W. C. Ellis, “Vapor-liquid-solid mechanism of single crystal growth,” *Appl. Phys. Lett.*, vol. 4, no. 5, pp. 89–90, 1964, doi: 10.1063/1.1753975.
- [92] P. X. Gao and Z. L. Wang, "Substrate atomic-termination-induced anisotropic growth of ZnO nanowires/nanorods by the VLS process," *J. Phys. Chem. B*, vol. 108, no. 23, pp. 7534–7537, 2004, doi: 10.1021/jp049657n.
- [93] D. Calestani, M. Zha, G. Salviati, L. Lazzarini, L. Zanotti, E. Comini and G. Sberveglieri "Nucleation and growth of SnO<sub>2</sub> nanowires," *J. Cryst. Growth*, vol. 275, no. 1–2, pp. 2083–2087, 2005, doi: 10.1016/j.jcrysgro.2004.11.269.
- [94] M. Wei, D. Zhi, and J. L. MacManus-Driscoll, “Self-catalysed growth of zinc oxide nanowires,” *Nanotechnology*, vol. 16, no. 8, pp. 1364–1368, 2005, doi: 10.1088/0957-4484/16/8/064.
- [95] S. T. Lee, N. Wang, Y. F. Zhang, and Y. H. Tang, “Oxide-assisted semiconductor nanowire growth,” *MRS Bull.*, vol. 24, no. 8, pp. 36–42, 1999, doi: 10.1557/S088376940005288X.
- [96] G.-C. Yi, *Semiconductor nanostructures for optoelectronic devices: processing, characterization and applications*. Springer Science & Business Media, 2012.
- [97] V. Gottschalch, G. Wagner, J. Bauer, H. Paetzelt, and M. Shirnow, “VLS growth of GaN nanowires on various substrates,” *J. Cryst. Growth*, vol. 310, no. 23, pp. 5123–5128, 2008, doi: 10.1016/j.jcrysgro.2008.08.013.

- [98] J. Men, Y. Liu, R. Luo, W. Li, L. Cheng, and L. Zhang, "Growth of SiC nanowires by low pressure chemical vapor infiltration using different catalysts," *J. Eur. Ceram. Soc.*, vol. 36, no. 15, pp. 3615–3625, 2016, doi: 10.1016/j.jeurceramsoc.2016.04.004.
- [99] N. M. Hieu, N. H. Hai, and M. A. Tuan, "Understanding the growth mechanisms of tin oxide nanowires by chemical vapor deposition," *J. Nanosci. Nanotechnol.*, vol. 21, no. 4, pp. 2538–2544, 2021, doi: 10.1166/jnn.2021.19092.
- [100] Y. Wu and P. Yang, "Direct observation of vapor-liquid-solid nanowire growth," *J. Am. Chem. Soc.*, vol. 123, no. 13, pp. 3165–3166, 2001, doi: 10.1021/ja0059084.
- [101] S. J. Park, Y. Y. Choi, J. G. Kim, and D. J. Choi, "Growth and mechanism of one-dimensional Al<sub>2</sub>O<sub>3</sub> nanostructures grown by chemical vapor deposition from an Al powder source," *J. Cryst. Growth*, vol. 361, no. 1, pp. 189–194, 2012, doi: 10.1016/j.jcrysgr.2012.09.038.
- [102] T. J. Trentler, K. M. Hickman, S. C. Goel, A. M. Viano, P. C. Gibbons, and W. E. Buhro, "Solution-liquid-solid growth of crystalline III-V semiconductors: An analogy to vapor-liquid-solid growth," *Science*, vol. 270, no. 5243, pp. 1791–1794, 1995, doi: 10.1126/science.270.5243.1791.
- [103] K. L. Hull, J. W. Grebinski, T. H. Kosel, and M. Kuno, "Induced branching in confined PbSe nanowires," *Chem. Mater.*, vol. 17, no. 17, pp. 4416–4425, 2005, doi: 10.1021/cm050952+.
- [104] Z. Li, O. Kurtulus, N. Fu, Z. Wang, A. Kornowski, U. Pietsch and A. Mews, "Controlled synthesis of CdSe nanowires by solution-liquid-solid method," *Adv. Funct. Mater.*, vol. 19, no. 22, pp. 3650–3661, 2009, doi: 10.1002/adfm.200900569.

- [105] P. Yang, Y. Wu, and R. Fan, "Inorganic semiconductor nanowires," *Int. J. Nanosci.*, vol. 01, no. 01, pp. 1–39, 2002, doi: 10.1142/S0219581X02000061.
- [106] T. Thongtem, A. Phuruangrat, and S. Thongtem, "Solvothermal synthesis of CdS nanowires templated by polyethylene glycol," *Ceram. Int.*, vol. 35, no. 7, pp. 2817–2822, 2009, doi: 10.1016/j.ceramint.2009.03.024.
- [107] W. H. Zhang and W. D. Zhang, "One-pot solvothermal strategy for the synthesis of ultrathin ZnS nanowires," *Mater. Lett.*, vol. 98, pp. 5–7, 2013, doi: 10.1016/j.matlet.2013.01.128.
- [108] B. M. Wen, C. Y. Liu, and Y. Liu, "Solvothermal synthesis of ultralong single-crystalline TiO<sub>2</sub> nanowires," *New J. Chem.*, vol. 29, no. 7, pp. 969–971, 2005, doi: 10.1039/b502604k.
- [109] Q. Gu, K. Zhu, N. Zhang, Q. Sun, P. Liu, J. Liu, J. Wang, and Z. Li, "Modified solvothermal strategy for straightforward synthesis of cubic NaNbO<sub>3</sub> nanowires with enhanced photocatalytic H<sub>2</sub> evolution," *J. Phys. Chem. C*, vol. 119, no. 46, pp. 25956–25964, 2015, doi: 10.1021/acs.jpcc.5b08018.
- [110] H. G. Choi, Y. H. Jung, and D. K. Kim, "Solvothermal synthesis of tungsten oxide nanorod/nanowire/nanosheet," *J. Am. Ceram. Soc.*, vol. 88, no. 6, pp. 1684–1686, 2005, doi: 10.1111/j.1551-2916.2005.00341.x.
- [111] M. Malekshahi Byranvand, A. Nemati Kharat, L. Fatholahi, and Z. M. Beiranvand, "A review on synthesis of nano-TiO<sub>2</sub> via different methods," *J. Nanostructures*, vol. 3, no. 1, pp. 1–9, 2013, doi: 10.7508/jns.2013.01.001.
- [112] J. Zhao, Q. He, B. Yao, Q. Zhang, T. Zhang, Q. Wang, and X. Han "Hydrothermal synthesis of Y<sub>3</sub>NbO<sub>7</sub> nanowires for the photocatalytic degradation of omeprazole sodium,"

- Ceram. Int.*, vol. 41, no. 6, pp. 7669–7676, 2015, doi: 10.1016/j.ceramint.2015.02.095.
- [113] X. Jiang, M. Lin, N. Tu, C. Chen, S. Zhou, and H. Zhan, "Simple hydrothermal synthesis and sintering of  $\text{Na}_{0.5}\text{Bi}_{0.5}\text{TiO}_3$  nanowires," *J. Alloys Compd.*, vol. 509, no. 38, pp. 9346–9350, 2011, doi: 10.1016/j.jallcom.2011.07.034.
- [114] J. Mu, J. Wang, J. Hao, P. Cao, S. Zhao, W. Zeng, B. Miao, and S. Xu, "Hydrothermal synthesis and electrochemical properties of  $\text{V}_2\text{O}_5$  nanomaterials with different dimensions," *Ceram. Int.*, vol. 41, no. 10, pp. 12626–12632, 2015, doi: 10.1016/j.ceramint.2015.06.091.
- [115] L. Li, H. Yang, H. Zhao, J. Yu, J. Ma, L. An, and X. Wang, X., "Hydrothermal synthesis and gas sensing properties of single-crystalline ultralong ZnO nanowires," *Appl. Phys. A Mater. Sci. Process.*, vol. 98, no. 3, pp. 635–641, 2010, doi: 10.1007/s00339-009-5457-y.
- [116] J. Yang, J. Zhang, C. Liang, M. Wang, P. Zhao, M. Liu, J. Liu, and R. Che, "Ultrathin  $\text{BaTiO}_3$  nanowires with high aspect ratio: A simple one-step hydrothermal synthesis and their strong microwave absorption," *ACS Appl. Mater. Interfaces*, vol. 5, no. 15, pp. 7146–7151, 2013, doi: 10.1021/am4014506.
- [117] N. A. Alshehri, A. R. Lewis, C. Pleydell-Pearce, and T. G. Maffei, "Investigation of the growth parameters of hydrothermal ZnO nanowires for scale up applications," *J. Saudi Chem. Soc.*, vol. 22, no. 5, pp. 538–545, 2018, doi: 10.1016/j.jscs.2017.09.004.
- [118] J. L. Gomez and O. Tigli, "Zinc oxide nanostructures: from growth to application," *J. Mater. Sci.*, vol. 48, no. 2, pp. 612–624, 2013, doi: 10.1007/s10853-012-6938-5.
- [119] B. Xiang, P. Wang, X. Zhang, S. A. Dayeh, D. P. Aplin, C. Soci, D. Yu, and D. Wang, "Rational synthesis of p-type zinc oxide nanowire arrays using simple chemical vapor deposition," *Nano Lett.*, vol. 7, no. 2, pp. 323–328, 2007, doi: 10.1021/nl062410c.

- [120] Y. Li, Z. Fan, J. G. Lu, and R. P. H. Chang, "Synthesis of magnesium borate ( $\text{Mg}_2\text{B}_2\text{O}_5$ ) nanowires by chemical vapor deposition method," *Chem. Mater.*, vol. 16, no. 13, pp. 2512–2514, 2004, doi: 10.1021/cm0496366.
- [121] H. Liu, Z. Huang, X. Zhang, M. Fang, Y. G. Liu, X. Wu, and X. Min, "Large scale synthesis of  $\alpha\text{-Si}_3\text{N}_4$  nanowires through a kinetically favored chemical vapour deposition process," *Phys. E Low-Dimensional Syst. Nanostructures*, vol. 95, pp. 132–138, 2018, doi: 10.1016/j.physe.2017.09.013.
- [122] S. V. Fridrikh, J. H. Yu, M. P. Brenner, and G. C. Rutledge, "Controlling the fiber diameter during electrospinning," *Phys. Rev. Lett.*, vol. 90, no. 14, p. 144502, Apr. 2003, doi: 10.1103/PhysRevLett.90.144502.
- [123] A. Haider, S. Haider, and I.-K. Kang, "A comprehensive review summarizing the effect of electrospinning parameters and potential applications of nanofibers in biomedical and biotechnology," *Arab. J. Chem.*, vol. 11, no. 8, pp. 1165–1188, 2018, doi: 10.1016/j.arabjc.2015.11.015.
- [124] M. M. Hohman, M. Shin, G. Rutledge, and M. P. Brenner, "Electrospinning and electrically forced jets. II. Applications," *Phys. Fluids*, vol. 13, no. 8, pp. 2221–2236, 2001, doi: 10.1063/1.1384013.
- [125] L. T. Cherney, "ELECTROHYDRODYNAMICS of electrified liquid menisci and emitted jets," *J. Aerosol Sci.*, vol. 30, no. 7, pp. 851–862, 1999, doi: 10.1016/S0021-8502(98)00756-3.
- [126] H. Wu, W. Pan, D. Lin, and H. Li, "Electrospinning of ceramic nanofibers: Fabrication, assembly and applications," *J. Adv. Ceram.*, vol. 1, no. 1, pp. 2–23, 2012, doi: 10.1007/s40145-012-0002-4.

- [127] D. Li, J. T. McCann, Y. Xia, and M. Marquez, "Electrospinning: A simple and versatile technique for producing ceramic nanofibers and nanotubes," *J. Am. Ceram. Soc.*, vol. 89, no. 6, pp. 1861–1869, 2006, doi: 10.1111/j.1551-2916.2006.00989.x.
- [128] D. Malwal and P. Gopinath, "Fabrication and applications of ceramic nanofibers in water remediation: A review," *Crit. Rev. Environ. Sci. Technol.*, vol. 46, no. 5, pp. 500–534, 2016, doi: 10.1080/10643389.2015.1109913.
- [129] M. V. Someswararao, R. S. Dubey, P. S. V. Subbarao, and S. Singh, "Electrospinning process parameters dependent investigation of TiO<sub>2</sub> nanofibers," *Results Phys.*, vol. 11, pp. 223–231, 2018, doi: 10.1016/j.rinp.2018.08.054.
- [130] P. K. Panda, "Ceramic nanofibers by electrospinning technique—A review," *Trans. Indian Ceram. Soc.*, vol. 66, no. 2, pp. 65–76, Apr. 2007, doi: 10.1080/0371750X.2007.11012252.
- [131] N. Sarlak, M. A. F. Nejad, S. Shakhesi, and K. Shabani, "Effects of electrospinning parameters on titanium dioxide nanofibers diameter and morphology: An investigation by Box–Wilson central composite design (CCD)," *Chem. Eng. J.*, vol. 210, pp. 410–416, 2012, doi: 10.1016/j.cej.2012.08.087.
- [132] P. K. Panda and S. Ramakrishna, "Electrospinning of alumina nanofibers using different precursors," *J. Mater. Sci.*, vol. 42, no. 6, pp. 2189–2193, 2007, doi: 10.1007/s10853-007-1581-2.
- [133] D. Lin, W. Pan, and H. Wu, "Morphological control of centimeter long aluminum-doped zinc oxide nanofibers prepared by electrospinning," *J. Am. Ceram. Soc.*, vol. 90, no. 1, pp. 71–76, 2007, doi: 10.1111/j.1551-2916.2006.01366.x.

- [134] A. D'Agostino, A. Taglietti, R. Desando, M. Bini, M. Patrini, G. Dacarro, L. Cucca, P. Pallavicini, and P. Grisoli, "Influence of solution properties and process parameters on the formation and morphology of YSZ and NiO ceramic nanofibers by electrospinning," *Nanomaterials*, vol. 7, no. 1, 2017, doi: 10.3390/nano7010016.
- [135] A. Evcin and D. A. Kaya, "Effect of production parameters on the structure and morphology of aluminum titanate nanofibers produced using electrospinning technique," *Sci. Res. Essays*, vol. 5, no. 23, pp. 3682–3686, 2010.
- [136] N. A. M. Barakat, B. Kim, and H. Y. Kim, "Production of smooth and pure nickel metal nanofibers by the electrospinning technique: Nanofibers possess splendid magnetic properties," *J. Phys. Chem. C*, vol. 113, no. 2, pp. 531–536, 2009, doi: 10.1021/jp805692r.
- [137] C. Lin, M. O. Lai, L. Lu, H. Zhou, and Y. Xin, "Structure and high rate performance of Ni<sup>2+</sup> doped Li<sub>4</sub>Ti<sub>5</sub>O<sub>12</sub> for lithium ion battery," *J. Power Sources*, vol. 244, pp. 272–279, 2013, doi: 10.1016/j.jpowsour.2013.01.056.
- [138] S. K. Lim, S. K. Lee, S. H. Hwang, and H. Kim, "Photocatalytic deposition of silver nanoparticles onto organic/inorganic composite nanofibers," *Macromol. Mater. Eng.*, vol. 291, no. 10, pp. 1265–1270, 2006, doi: 10.1002/mame.200600264.
- [139] N. Bhardwaj and S. C. Kundu, "Electrospinning: A fascinating fiber fabrication technique," *Biotechnol. Adv.*, vol. 28, no. 3, pp. 325–347, 2010, doi: 10.1016/j.biotechadv.2010.01.004.
- [140] T. Subbiah, G. S. Bhat, R. W. Tock, S. Parameswaran, and S. S. Ramkumar, "Electrospinning of nanofibers," *J. Appl. Polym. Sci.*, vol. 96, no. 2, pp. 557–569, 2005, doi: 10.1002/app.21481.

- [141] D. Li and Y. Xia, "Electrospinning of nanofibers: reinventing the wheel?," *Adv. Mater.*, vol. 16, no. 14, pp. 1151–1170, 2004, doi: 10.1002/adma.200400719.
- [142] L. Yan, H. Lan, H. Yu, S. Qian, X. Cheng, N. Long, R. Zhang, M. Shui, and J. Shu, "Electrospun  $\text{WNb}_{12}\text{O}_{33}$  nanowires: superior lithium storage capability and their working mechanism," *J. of Materials Chem. A*, vol. 5, no. 19, pp. 8972–8980, 2017, doi: 10.1039/C7TA01784g.
- [143] J. Akimoto, K. Kataoka, N. Kojima, S. Hayashi, Y. Gotoh, T. Sotokawa, and Y. Kumashiro, "A novel soft-chemical synthetic route using  $\text{Na}_2\text{Ti}_6\text{O}_{13}$  as a starting compound and electrochemical properties of  $\text{H}_2\text{Ti}_{12}\text{O}_{25}$ ," *J. Power Sources*, vol. 244, pp. 679–683, 2013, doi: 10.1016/j.jpowsour.2012.12.035.
- [144] Y. Zhao, S. Pang, C. Zhang, Q. Zhang, L. Gu, X. Zhou, G. Li, and G. Cui, "Nitridated mesoporous  $\text{Li}_4\text{Ti}_5\text{O}_{12}$  spheres for high-rate lithium-ion batteries anode material," *J. Solid State Electrochem.*, vol. 17, no. 5, pp. 1479–1485, 2013, doi: 10.1007/s10008-013-2026-2.
- [145] C. Villevieille, M. Van Thournout, J. Scoyer, C. Tessier, J. Olivier-Fourcade, J. C. Jumas, and L. Monconduit "Carbon modified  $\text{Li}_2\text{Ti}_3\text{O}_7$  ramsdellite electrode for Li-ion batteries," *Electrochimica Acta*, vol. 55, no. 23, pp. 7080–7084, 2010, doi: 10.1016/j.electacta.2010.06.052.
- [146] D. Saritha, V. Pralong, U. V. Varadaraju, and B. Raveau, "Electrochemical Li insertion studies on  $\text{WNb}_{12}\text{O}_{33}$ —A shear  $\text{ReO}_3$  type structure," *J. Solid State Chem.*, vol. 183, no. 5, pp. 988–993, 2010, doi: 10.1016/j.jssc.2010.03.003.
- [147] L. Li, Q. Ma, S. Wang, S. Song, B. Li, R. Guo, X. Cheng, and Q. Cheng, "Photocatalytic performance and degradation mechanism of aspirin by  $\text{TiO}_2$  through response surface methodology," *Catalysts*, vol. 8, no. 3, 2018., doi: 10.3390/catal8030118.

- [148] C. F. Bustillo-Lecompte and M. Mehrvar, "Treatment of an actual slaughterhouse wastewater by integration of biological and advanced oxidation processes: Modeling, optimization, and cost-effectiveness analysis," *J. Environ. Manage.*, vol. 182, pp. 651–666, 2016, doi: 10.1016/j.jenvman.2016.07.044.
- [149] A. Rabbi, K. Nasouri, H. Bahrambeygi, A. M. Shoushtari, and M. R. Babaei, "RSM and ANN approaches for modeling and optimizing of electrospun polyurethane nanofibers morphology," *Fibers Polym.*, vol. 13, no. 8, pp. 1007–1014, 2012, doi: 10.1007/s12221-012-1007-x.
- [150] H. Homayoni, S. A. H. Ravandi, and M. Valizadeh, "Electrospinning of chitosan nanofibers: Processing optimization," *Carbohydr. Polym.*, vol. 77, no. 3, pp. 656–661, 2009, doi: 10.1016/j.carbpol.2009.02.008.
- [151] Y. P. Lin and M. Mehrvar, "Photocatalytic treatment of an actual confectionery wastewater using Ag/TiO<sub>2</sub>/Fe<sub>2</sub>O<sub>3</sub>: Optimization of photocatalytic reactions using surface response methodology," *Catalysts*, vol. 8, no. 10, pp. 1–17, 2018, doi: 10.3390/catal8100409.
- [152] R. J. Del Vecchio, *Understanding design of experiments: A primer for technologists*; Hanser/Gardner Publications Inc., Cincinnati, OH, USA, 1997.
- [153] S. L. Ferreira, R. E. Bruns, E. G. da Silva, W. N. dos Santos, C. M. Quintella, J. M. David, J. B. de Andrade, M. C. Breitzkreitz, I. C. Jardim, and B. B. Neto, "Statistical designs and response surface techniques for the optimization of chromatographic systems," *J. Chromatogr. A*, vol. 1158, no. 1–2, pp. 2–14, Jul. 2007, doi: 10.1016/j.chroma.2007.03.051.

- [154] F. Topuz, T. Holtzl, and G. Szekely, “Scavenging organic micropollutants from water with nanofibrous hypercrosslinked cyclodextrin membranes derived from green resources,” *Chem. Eng. J.*, vol. 419, p. 129443, 2021, doi: 10.1016/j.cej.2021.129443.
- [155] F. Topuz, M. A. Abdulhamid, T. Holtzl, and G. Szekely, “Nanofiber engineering of microporous polyimides through electrospinning: Influence of electrospinning parameters and salt addition,” *Mater. Des.*, vol. 198, p. 109280, Jan. 2021, doi: 10.1016/j.matdes.2020.109280.
- [156] Utkarsh, H. Hegab, M. Tariq, N. A. Syed, G. Rizvi, and R. Pop-Iliev, “Towards analysis and optimization of electrospun PVP (polyvinylpyrrolidone) nanofibers,” *Adv. Polym. Technol.*, vol. 2020, pp. 1–9, May 2020, doi: 10.1155/2020/4090747.
- [157] H. E. Abdelhakim, A. Coupe, C. Tuleu, M. Edirisinghe, and D. Q. M. Craig, “Electrospinning optimization of Eudragit EPO with and without chlorpheniramine maleate using a design of experiment approach,” *Mol. Pharm.*, vol. 16, no. 6, pp. 2557–2568, 2019, doi: 10.1021/acs.molpharmaceut.9b00159.
- [158] B. Cao, L. A. Adutwum, A. O. Oliynyk, E. J. Lubner, B. C. Olsen, A. Mar, and J. M. Buriak “How To Optimize Materials and Devices *via* Design of experiments and machine learning: demonstration using organic photovoltaics,” *ACS Nano*, vol. 12, no. 8, pp. 7434–7444, 2018, doi: 10.1021/acsnano.8b04726.
- [159] R. Hardian, Z. Liang, X. Zhang, and G. Szekely, “Artificial intelligence: the silver bullet for sustainable materials development,” *Green Chem.*, vol. 22, no. 21, pp. 7521–7528, 2020, doi: 10.1039/D0GC02956D.
- [160] M. D. Abràmoff, P. J. Magalhães, and S. J. Ram, “Image processing with ImageJ,” *Biophotonics Int.*, vol. 11, no. 7, pp. 36–42, 2004.

- [161] S. Ray and J. A. Lalman, "Using the Box–Benkhen design (BBD) to minimize the diameter of electrospun titanium dioxide nanofibers," *Chem. Eng. J.*, vol. 169, no. 1–3, pp. 116–125, 2011, doi: 10.1016/j.cej.2011.02.061.
- [162] A. Khalil, R. Hashaikeh, and M. Jouiad, "Synthesis and morphology analysis of electrospun copper nanowires," *J. Mater. Sci.*, vol. 49, no. 8, pp. 3052–3065, 2014, doi: 10.1007/s10853-013-8005-2.
- [163] J. M. Deitzel, J. Kleinmeyer, D. Harris, and N. C. Beck Tan, "The effect of processing variables on the morphology of electrospun nanofibers and textiles," *Polymer*, vol. 42, no. 1, pp. 261–272, 2001, doi: 10.1016/S0032-3861(00)00250-0.
- [164] K. P. Matabola and R. M. Moutloali, "The influence of electrospinning parameters on the morphology and diameter of poly(vinylidene fluoride) nanofibers- effect of sodium chloride," *J. Mater. Sci.*, vol. 48, no. 16, pp. 5475–5482, 2013, doi: 10.1007/s10853-013-7341-6.
- [165] A. K. Haghi and M. Akbari, "Trends in electrospinning of natural nanofibers," *Phys. Status Solidi A*, vol. 204, no. 6, pp. 1830–1834, 2007, doi: 10.1002/pssa.200675301.
- [166] V. Beachley and X. Wen, "Effect of electrospinning parameters on the nanofiber diameter and length," *Mater. Sci. Eng. C*, vol. 29, no. 3, pp. 663–668, 2009, doi: 10.1016/j.msec.2008.10.037.
- [167] M. Elkasaby, H. A. Hegab, A. Mohany, and G. M. Rizvi, "Modeling and optimization of electrospinning of polyvinyl alcohol (PVA)," *Adv. Polym. Technol.*, vol. 37, no. 6, pp. 2114–2122, 2018.

- [168] R. Schmuck, R. Wagner, G. Hörpel, T. Placke, and M. Winter, “Performance and cost of materials for lithium-based rechargeable automotive batteries,” *Nat. Energy*, vol. 3, no. 4, pp. 267–278, 2018, doi: 10.1038/s41560-018-0107-2.
- [169] Q. Deng, Y. Fu, C. Zhu, and Y. Yu, “Niobium-Based Oxides Toward Advanced Electrochemical Energy Storage: Recent Advances and Challenges,” *Small*, vol. 15, no. 32, p. 1804884, 2019, doi: 10.1002/sml.201804884.
- [170] J. Asenbauer, T. Eisenmann, M. Kuenzel, A. Kazzazi, Z. Chen, and D. Bresser, “The success story of graphite as a lithium-ion anode material – fundamentals, remaining challenges, and recent developments including silicon (oxide) composites,” *Sustain. Energy Fuels*, vol. 4, no. 11, pp. 5387–5416, 2020, doi: 10.1039/D0SE00175A.
- [171] J.-T. Han and J. B. Goodenough, “3-V Full Cell Performance of Anode Framework  $\text{TiNb}_2\text{O}_7$  /Spinel  $\text{LiNi}_{0.5}\text{Mn}_{1.5}\text{O}_4$ ,” *Chem. Mater.*, vol. 23, no. 15, pp. 3404–3407, 2011, doi: 10.1021/cm201515g.
- [172] B. Guo, X. Wang, P. F. Fulvio, M. Chi, and S. M. Mahurin, “Soft-templated mesoporous carbon-carbon nanotube composites for high-performance lithium-ion batteries,” *Advanced mater.*, vol. 23, no. 40, pp. 4661–4666, 2011, doi: 10.1002/adma.201102032.
- [173] V. Etacheri, R. Marom, R. Elazari, G. Salitra, and D. Aurbach, “Challenges in the development of advanced Li-ion batteries: a review,” *Energy Environ. Sci.*, vol. 4, no. 9, p. 3243, 2011, doi: 10.1039/c1ee01598b.
- [174] N. Y. Yao, H. K. Liu, X. Liang, Y. Sun, X. Y. Feng, C. H. Chen, and H. F. Xiang, “ $\text{Li}_4\text{Ti}_5\text{O}_{12}$  nanosheets embedded in three-dimensional amorphous carbon for superior-rate battery applications,” *J. Alloys Compd.*, vol. 771, pp. 755–761, 2019, doi: 10.1016/j.jallcom.2018.08.001.

- [175] J. Zhang, C. Zhou, V. Naenen, L.-W. Jang, J.-P. Locquet, and J. W. Seo, "Facile synthesis of dual-phase lithium titanate nanowires as anode materials for lithium-ion battery," *J. Alloys Compd.*, vol. 875, p. 160038, 2021, doi: 10.1016/j.jallcom.2021.160038.
- [176] L. Yan, H. Lan, H. Yu, S. Qian, X. Cheng, N. Long, R. Zhang, M. Shui, and J. Shu, "Electrospun  $\text{WNb}_{12}\text{O}_{33}$  nanowires: superior lithium storage capability and their working mechanism," *J. of Materials Chem. A*, vol. 5, no. 19, pp. 8972–8980, 2017, doi: 10.1039/C7TA01784g.
- [177] K. J. Griffith, K. M. Wiaderek, G. Cibin, L. E. Marbella, and C. P. Grey, "Niobium tungsten oxides for high-rate lithium-ion energy storage," *Nature*, vol. 559, no. 7715, pp. 556–563, Jul. 2018, doi: 10.1038/s41586-018-0347-0.
- [178] C. Lin, S. Deng, H. Shen, G. Wang, Y. Li, L. Yu, S. Lin, J. Li, and L. Lu, " $\text{Li}_5\text{Cr}_9\text{Ti}_4\text{O}_{24}$ : a new anode material for lithium-ion batteries," *J. of Alloys and Compounds*, vol. 650, pp. 616–621, 2015, doi: 10.1016/j.jallcom.2015.08.070.
- [179] D. Kang, J. Li, and Y. Zhang, "Effect of Ni Doping Content on Phase Transition and Electrochemical Performance of  $\text{TiO}_2$  Nanofibers Prepared by Electrospinning Applied for Lithium-Ion Battery Anodes," *Materials*, vol. 13, no. 6, p. 1302, 2020, doi: 10.3390/ma13061302.
- [180] R. Li, Y. Qin, X. Liu, L. Yang, C. Lin, and R. Xia, "Conductive  $\text{Nb}_{25}\text{O}_{62}$  and  $\text{Nb}_{12}\text{O}_{29}$  anode materials for use in high-performance lithium-ion storage," *Electrochim. Acta*, vol. 266, pp. 202–211, 2018, doi: 10.1016/j.electacta.2018.02.034.

- [181] D. Cao, Z. Yao, J. Liu, J. Zhang, and C. Li, “H-Nb<sub>2</sub>O<sub>5</sub> wired by tetragonal tungsten bronze related domains as high-rate anode for Li-ion batteries,” *Energy Storage Mater.*, vol. 11, pp. 152–160, 2018, doi: 10.1016/j.ensm.2017.10.005.
- [182] C. Shi, K. Xiang, Y. Zhu, X. Chen, W. Zhou, and H. Chen, “Nb<sub>2</sub>O<sub>5</sub> nanospheres / surface-modified graphene composites as superior anode materials in lithium-ion batteries,” *Ceram. Int.*, vol. 43, no. 8, pp. 6232–6238, 2017, doi: 10.1016/j.ceramint.2017.02.021.
- [183] X. Wen, C. Ma, C. Du, J. Liu, X. Zhang, D. Qu, and Z. Tang, “Enhanced electrochemical properties of vanadium-doped titanium niobate as a new anode material for lithium-ion batteries,” *Electrochim. Acta.*, vol. 186, pp. 58–63, 2015, doi: 10.1016/j.electacta.2015.10.158.
- [184] Y. Huang, S. Cao, X. Xie, C. Wu, S. Jamil, Q. Zhao, B. Chang, Y. Wang, and X. Wang, “Improving the structure and cycling stability of Ni-rich layered cathodes by dual modification of yttrium doping and surface coating,” *ACS Applied Mater. & Interfaces*, vol. 12, no. 17, pp.19483-19494, 2020, doi: 10.1021/acsami.0c01558.
- [185] I. A. Stenina, R. R. Shaydullin, A. V. Desyatov, T. L. Kulova, and A. B. Yaroslavtsev, “Effect of carbon and N-doped carbon nanomaterials on the electrochemical performance of lithium titanate-based composites,” *Electrochim. Acta*, vol. 364, 137330, 2020, doi: 10.1016/j.electacta.2020.137330.
- [186] D. P. Opra, S. V. Gnednikov, S. L. Sinebryukhov, A. V. Gerasimenko, A. M. Ziatdinov, A. A. Sokolov, A. B. Podgorbunsky, A. Y. Ustinov, V. G. Kuryavyi, V. Y. Mayorov, and I. A. Tkachenko, “Enhancing lithium and sodium storage properties of TiO<sub>2</sub>(B) nanobelts by doping with nickel and zinc,” *Nanomaterials*, vol. 11, no. 7, 1703, 2021, doi: 10.3390/nano11071703.

- [187] C. Yang, X. Liu, Z. Yang, L. Gu, and Y. Yu, "Improvement of lithium storage performance of molybdenum trioxide by a synergistic effect of surface coating and oxygen vacancies," *Adv. Mater. Interfaces*, vol. 3, no. 22, p. 1600730, 2016, doi: 10.1002/admi.201600730.
- [188] S. Li, X. Cao, C.N. Schmidt, Q. Xu, E. Uchaker, Y. Pei, and G. Cao, "TiNb<sub>2</sub>O<sub>7</sub>/graphene composites as high-rate anode materials for lithium/sodium ion batteries," *J. of Materials Chemistry A*, vol. 4, no. 11, pp. 4242–4251, 2016, doi: 10.1039/C5TA10510B.
- [189] C. Lin, G. Wang, S. Lin, J. Li, and L. Lu, "TiNb<sub>6</sub>O<sub>17</sub>: a new electrode material for lithium-ion batteries," *Chem Comm.*, vol. 51, no. 43, pp. 8970–8973, 2015, doi: 10.1039/C5CC01494H.
- [190] C. Lin, S. Yu, S. Wu, S. Lin, Z. Z. Zhu, J. Li, and L. Lu, "Ru<sub>0.01</sub>Ti<sub>0.99</sub>Nb<sub>2</sub>O<sub>7</sub> as an intercalation-type anode material with a large capacity and high rate performance for lithium-ion batteries," *J. Mater. Chem. A*, vol. 3, pp. 8627–8635, 2015, doi: 10.1039/C5TA01073J.
- [191] X. Ma, X. Cao, Y. Ye, F. Qiao, M. Qian, and Y. Wei, "Study on low-temperature performances of Nb<sub>16</sub>W<sub>5</sub>O<sub>55</sub> anode for lithium-ion batteries," *Solid State Ionics*, vol. 353, p. 115376, 2020, doi: 10.1016/j.ssi.2020.115376.
- [192] C. Yang, S. Yu, C. Lin, F. Lv, S. Wu, Y. Yang, W. Wang, Z. Z. Zhu, J. Li, N. Wang, and S. Guo, "Cr<sub>0.5</sub>Nb<sub>24.5</sub>O<sub>62</sub> nanowires with high electronic conductivity for high-rate and long-life lithium-ion storage," *ACS Nano*, vol. 11, no. 4, pp. 4217–4224, 2017, doi: 10.1021/acsnano.7b01163.

- [193] X. Lou, R. Li, X. Zhu, L. Luo, Y. Chen, C. Lin, H. Li, and X.S. Zhao, “New anode material for lithium-ion batteries: aluminum niobate ( $\text{AlNb}_{11}\text{O}_{29}$ ),” *ACS Appl. Mater. Interfaces*, vol. 11, no. 6, pp. 1–8, 2019, doi: 10.1021/acsami.8b20246.
- [194] L. Hou, X. Qin, X. Gao, T. Guo, X. Li, and J. Li, “Zr-doped  $\text{Li}_4\text{Ti}_5\text{O}_{12}$  anode materials with high specific capacity for lithium-ion batteries,” *J. Alloys Compd.*, vol. 774, pp. 38–45, 2019, doi: 10.1016/j.jallcom.2018.09.364.
- [195] S. Deng, Z. Luo, Y. Liu, X. Lou, C. Lin, C. Yang, H. Zhao, P. Zheng, Z. Sun, J. Li, and N. Wang, “ $\text{Ti}_2\text{Nb}_{10}\text{O}_{29-x}$  mesoporous microspheres as promising anode materials for high-performance lithium-ion batteries,” *J. Power Sources*, vol. 362, pp. 250–257, 2017, doi: 10.1016/j.jpowsour.2017.07.039.
- [196] X. Zhu, J. Xu, Y. Luo, Q. Fu, G. Liang, and L. Luo, “ $\text{MoNb}_{12}\text{O}_{33}$  as a new anode material for high-capacity, safe, rapid and durable  $\text{Li}^+$  storage: structural characteristics, electrochemical properties and working mechanisms,” *J. Mater. Chem. A Mater. energy Sustain.*, vol. 7, no. 416, pp. 6522–6532, 2019, doi: 10.1039/C9TA00309F.
- [197] C. J Jafta, K. I Ozoemena, M. K. Mathe, and W. D. Roos, “Synthesis, characterisation and electrochemical intercalation kinetics of nanostructured aluminium-doped Li  $[\text{Li}_{0.2}\text{Mn}_{0.54}\text{Ni}_{0.13}\text{Co}_{0.13}] \text{O}_2$  cathode material for lithium ion battery,” *Electrochimica Acta*, vol. 85, pp. 411–422, 2012, doi: 10.1016/j.electacta.2012.08.074.
- [198] L. Yan, S. Qian, H. Yu, P. Li, H. Lan, N. Long, R. Zhang, M. Shui, and J. Shu, “Carbon-enhanced electrochemical performance for spinel  $\text{Li}_5\text{Cr}_7\text{Ti}_6\text{O}_{25}$  as a lithium host material,” *ACS Sustain. Chem. Eng.*, vol. 5, no. 1, pp. 957–964, 2017, doi: 10.1021/ACSSUSCHEMENG.6B02280.

- [199] K. Kang, and G. Ceder, “Factors that affect Li mobility in layered lithium transition metal oxides,” *Phys. Rev. B - Condens. Matter Mater. Phys.*, vol. 74, no. 9, pp. 1–7, 2006, doi: 10.1103/PhysRevB.74.094105.
- [200] L.-Z. Bai, D.-L. Zhao, T.-M. Zhang, W.-G. Xie, J.-M. Zhang, and Z.-M. Shen, “A comparative study of electrochemical performance of graphene sheets, expanded graphite and natural graphite as anode materials for lithium-ion batteries,” *Electrochimica Acta*, vol. 107, pp. 555–561, 2013, doi: 10.1016/j.electacta.2013.06.032.
- [201] N. Nitta, F. Wu, J. T. Lee, and G. Yushin, “Li-ion battery materials: present and future,” *Mater. Today*, vol. 18, no. 5, pp. 252–264, 2015, doi: 10.1016/j.mattod.2014.10.040.
- [202] J. B. Kim, S. G. Lee, S.-Y. Choi, J. Kim, and S. O. Kim, “Doping behavior of Br in  $\text{Li}_4\text{Ti}_5\text{O}_{12}$  anode materials and their electrochemical performance for Li-ion batteries,” *Ceram. Int.*, vol. 45, no. 14, pp. 17574–17579, 2019, doi: 10.1016/j.ceramint.2019.05.322.
- [203] K. Wang, C. Zhang, H. Fu, C. Liu, Z. Li, W. Ma, X. Lu, and G. Cao, “Enhanced electrochemical properties of  $\text{Li}_3\text{VO}_4$  with controlled oxygen vacancies as Li-ion battery anode,” *Chem. - Eur. J.*, vol. 23, no. 22, pp. 5368–5374, 2017, doi: 10.1002/chem.201700150.
- [204] D. McNulty, D. N. Buckley, and C. O’Dwyer, “Synthesis and electrochemical properties of vanadium oxide materials and structures as Li-ion battery positive electrodes,” *J. Power Sources*, vol. 267, pp. 831–873, 2014, doi: 10.1016/j.jpowsour.2014.05.115.
- [205] C.-M. Park, J.-H. Kim, H. Kim, and H.-J. Sohn, “Li-alloy based anode materials for Li secondary batteries,” *Chem. Soc. Rev.*, vol. 39, no. 8, pp. 3115–3141, 2010, doi: 10.1039/b919877f.

- [206] D. Bresser, S. Passerini, and B. Scrosati, "Leveraging valuable synergies by combining alloying and conversion for lithium-ion anodes," *Energy Environ. Sci.*, vol. 9, no. 11, pp. 3348–3367, 2016, doi: 10.1039/C6EE02346K.
- [207] T. Takashima, T. Tojo, R. Inada, and Y. Sakurai, "Characterization of mixed titanium–niobium oxide  $\text{Ti}_2\text{Nb}_{10}\text{O}_{29}$  annealed in vacuum as anode material for lithium-ion battery," *J. Power Sources*, vol. 276, pp. 113–119, 2015, doi: 10.1016/j.jpowsour.2014.11.109.
- [208] C. Lin, S. Yu, H. Shao, S. Wu, G. Wang, L. Yu, Y. Li, Z. Zhu, J. Li, and S. Lin, "Defective  $\text{Ti}_2\text{Nb}_{10}\text{O}_{27.1}$ : An advanced anode material for lithium-ion batteries," *Sci. Rep.*, vol. 5, 17836, 2015, doi: 10.1038/srep17836.
- [209] B. O. Fatile, M. Pugh, and M. Medraj, "Nickel-Doped  $\text{Nb}_{18}\text{W}_{16}\text{O}_{93}$  nanowires with Improved electrochemical properties for lithium-ion battery anodes," *Available SSRN 4329593*.
- [210] H. Shen, Y. An, Q. Man, J. Wang, C. Liu, B. Xi, S. Xiong, J. Feng, and Y. Qian, "Controlled prelithiation of siloxene nanosheet anodes enables high performance 5 V-class lithium-ion batteries," *Chem. Eng. J.*, vol. 454, p. 140136, 2023, doi: 10.1016/j.cej.2022.140136.
- [211] Y. Zhan, Y. Wu, Y. An, C. Wei, L. Tan, B. Xi, S. Xiong, and J. Feng, "Ultrastable and High-Rate 2D Siloxene Anode Enabled by Covalent Organic Framework Engineering for Advanced Lithium-Ion Batteries," *Small Methods*, vol. 6, no. 6, p. 2200306, 2022, doi: 10.1002/smtd.202200306.
- [212] X. Wei, C. C. Lin, C. Wu, N. Qaiser, Y. Cai, A. Y. Lu, K. Qi, J. H. Fu, Y. H. Chiang, Z. Yang and L. Ding, "Three-dimensional hierarchically porous  $\text{MoS}_2$  foam as high-rate and

- stable lithium-ion battery anode," *Nat. Commun.*, vol. 13, no. 1, p. 6006, 2022, doi: 10.1038/s41467-022-33790-z.
- [213] J. Zhang, L. Zhang, J. Zhang, Z. Zhang, and Z. Wu, "Effect of surface/bulk oxygen vacancies on the structure and electrochemical performance of TiO<sub>2</sub> nanoparticles," *J. Alloys Compd.*, vol. 642, pp. 28–33, 2015, doi: 10.1016/j.jallcom.2015.04.096.
- [214] A. A. Voskanyan, M. Abramchuk, and A. Navrotsky, "Entropy stabilization of TiO<sub>2</sub>-Nb<sub>2</sub>O<sub>5</sub> wadsley-roth shear phases and their prospects for lithium-ion battery anode materials," *Chem. Mater.*, vol. 32, no. 12, pp. 5301–5308, 2020, doi: 10.1021/acs.chemmater.0c01553.
- [215] B. Zhao, X. Deng, R. Ran, M. Liu, and Z. Shao, "Facile Synthesis of a 3D Nanoarchitected Li<sub>4</sub>Ti<sub>5</sub>O<sub>12</sub> electrode for ultrafast energy storage," *Adv. Energy Mater.*, vol. 6, no. 4, p. 1500924, 2016, doi: 10.1002/aenm.201500924.
- [216] K. J. Griffith, A. Senyshyn, and C. P. Grey, "Structural stability from crystallographic shear in TiO<sub>2</sub>-Nb<sub>2</sub>O<sub>5</sub> phases: cation ordering and lithiation behavior of TiNb<sub>24</sub>O<sub>62</sub>," *Inorg. Chem.*, vol. 56, no. 7, pp. 4002–4010, 2017, doi: 10.1021/acs.inorgchem.6b03154.
- [217] C. P. Koçer, K. J. Griffith, C. P. Grey, and A. J. Morris, "Lithium Diffusion in Niobium Tungsten Oxide Shear Structures," *Chem. Mater.*, vol. 32, no. 9, pp. 3980–3989, 2020, doi: 10.1021/acs.chemmater.0c00483.
- [218] R. Li, G. Liang, X. Zhu, Q. Fu, Y. Chen, L. Luo, and C. Lin, "Mo<sub>3</sub>Nb<sub>14</sub>O<sub>44</sub>: A new Li<sup>+</sup> container for high-performance electrochemical energy storage," *Energy Environ. Mater.*, vol. 4, no. 1, pp. 65–71, 2021, doi: 10.1002/eem2.12098.
- [219] W. Zhu, S. A. El-Khodary, S. Li, B. Zou, R. Kang, G. LiD. H. Ng, X. Liu, J. Qiu, Y. Zhao, and Y. Huang, "Roselle-like Zn<sub>2</sub>Ti<sub>3</sub>O<sub>8</sub>/rGO nanocomposite as anode for lithium-ion

- capacitor," *Chem. Eng. J.*, vol. 385, 123881, 2020, doi: 10.1016/j.cej.2019.123881.
- [220] P. Zeng, Y. Zhao, Y. Lin, X. Wang, J. Li, W. Wang, and Z. Fang, "Enhancement of electrochemical performance by the oxygen vacancies in hematite as anode material for lithium-ion batteries," *Nanoscale Res. Lett.*, vol. 12, no. 13, pp. 1–9, 2017, doi: 10.1186/s11671-016-1783-0.
- [221] H. Song, P. B. Wignall, D. Chu, J. Tong, Y. Sun, H. Song, W. He, and L. Tian, "Stabilization of oxygen-deficient structure for conducting  $\text{Li}_4\text{Ti}_5\text{O}_{12-\delta}$  by molybdenum doping in a reducing atmosphere," *Sci. Rep.*, vol. 4, 4132, 2014, doi: 10.1038/srep04132.
- [222] S. Schweidler, L. de Biasi, A. Schiele, P. Hartmann, T. Brezesinski, and J. Janek, "Volume Changes of Graphite Anodes Revisited: A Combined Operando X-ray Diffraction and In Situ Pressure Analysis Study," *J. Phys. Chem. C*, vol. 122, no. 16, pp. 8829–8835, 2018, doi: 10.1021/acs.jpcc.8b01873.
- [223] H. Li, L. Shen, B. Ding, G. Pang, H. Dou, and X. Zhang, "Ultralong  $\text{SrLi}_2\text{Ti}_6\text{O}_{14}$  nanowires composed of single-crystalline nanoparticles: Promising candidates for high-power lithium ions batteries," *Nano Energy*, vol. 13, pp. 18–27, 2015, doi: 10.1016/j.nanoen.2015.02.002.
- [224] S. Wang, L. Li, W. He, Y. Shao, Y. Li, Y. Wu, and X. Hao, "Oxygen vacancy modulation of bimetallic oxynitride anodes toward advanced Li-ion capacitors," *Adv. Funct. Mater.*, vol. 30, no. 27, pp. 1–11, 2020, doi: 10.1002/adfm.202000350.
- [225] J. Zhang and J. Li, "The oxygen vacancy defect of ZnO/NiO nanomaterials improves photocatalytic performance and ammonia sensing performance," *Nanomaterials*, vol. 12, no. 3, p. 433, 2022, doi: 10.3390/nano12030433.

- [226] S. Yang, Y. Liu, Y. Hao, X. Yang, W. A. Goddard III, X. L. Zhang, and B. Cao, "Oxygen-vacancy abundant ultrafine  $\text{Co}_3\text{O}_4$ /graphene composites for high-rate supercapacitor electrodes," *Adv. Sci.*, vol. 5, no. 4, 1700659, 2018, doi: 10.1002/advs.201700659.
- [227] S. Yang, Y. Lin, X. Song, P. Zhang, and L. Gao, "Covalently Coupled Ultrafine H-TiO<sub>2</sub> Nanocrystals/Nitrogen-Doped Graphene Hybrid Materials for High-Performance Supercapacitor," *ACS Appl. Mater. Interfaces*, vol. 7, no. 32, pp. 17884–17892, Aug. 2015, doi: 10.1021/acsami.5b04368.
- [228] G. C. Leindecker, A. K. Alves, and C. P. Bergmann, "Synthesis of niobium oxide fibers by electrospinning and characterization of their morphology and optical properties," *Ceram. Int.*, vol. 40, no. 10, pp. 16195–16200, 2014, doi: 10.1016/j.ceramint.2014.07.054.
- [229] S. Lou, X. Cheng, Y. Zhao, A. Lushington, J. Gao, Q. Li, P. Zou, B. Wang, Y. Gao, Y. Ma, and C. Du, "Superior performance of ordered macroporous  $\text{TiNb}_2\text{O}_7$  anodes for lithium-ion batteries: Understanding from the structural and pseudocapacitive insights on achieving high rate capability," *Nano Energy*, vol. 34, pp. 15–25, 2017, doi: 10.1016/j.nanoen.2017.01.058.
- [230] X. Lou, C. Lin, Q. Luo, J. Zhao, B. Wang, J. Li, Q. Shao, X. Guo, N. Wang, and Z. Guo, "Crystal structure modification enhanced  $\text{FeNb}_{11}\text{O}_{29}$  anodes for lithium-ion batteries," *ChemElectroChem*, vol. 4, pp. 3171–3180, 2017, doi: DOI: 10.1002/celec.201700816.
- [231] S. R. Sahu, V. R. Rikka, P. Haridoss, A. Chatterjee, R. Gopalan, and R. Prakash, "A Novel  $\alpha$ - $\text{MoO}_3$ /single-walled carbon nanohorns composite as high-performance anode material for fast-charging lithium-ion battery," *Adv. Energy Mater.*, vol. 10, 2001627, 2020, doi: doi.org/10.1002/aenm.202001627.

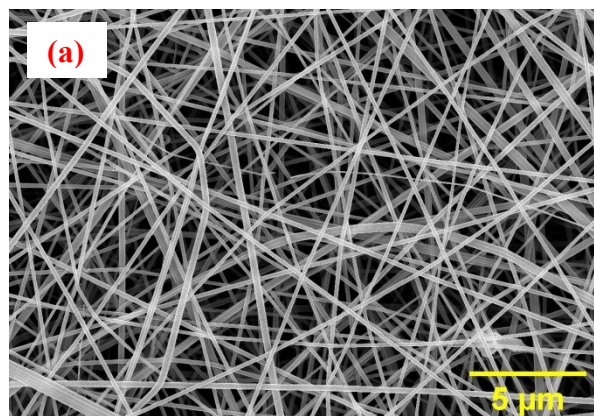
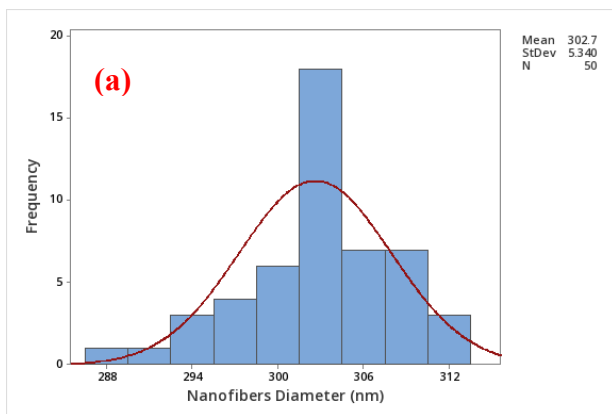
## Appendix

The appendix contains additional information obtained from the studies on influence of process parameters on morphology and diameter of electrospun  $\text{MoNb}_{12}\text{O}_{33}$  nanofibers.

### Appendix A

#### A-1: Design of experiment

The influence of process parameters on morphology and diameter of electrospun  $\text{MoNb}_{12}\text{O}_{33}$  nanofibers was investigated using the same approach reported for  $\text{Nb}_{18}\text{W}_{16}\text{O}_{93}$  in chapter three. An experiment involving five continuous factors (Table 3-2) was designed using the Box–Wilson Central Composite Design (CCD). The CCD produced a total of thirty-six experimental runs, ten of which were conducted as replications of the central points. The preparation of  $\text{MoNb}_{12}\text{O}_{33}$  precursor solution, spinning of the nanofibers, and measurement were carried out following the procedures described in chapter three and five. The results obtained for each of the experiments are presented in Table A-1. The representative SEM images of the nanofibers and corresponding histogram showing the distribution of the nanofibers are presented in Figure A-1.



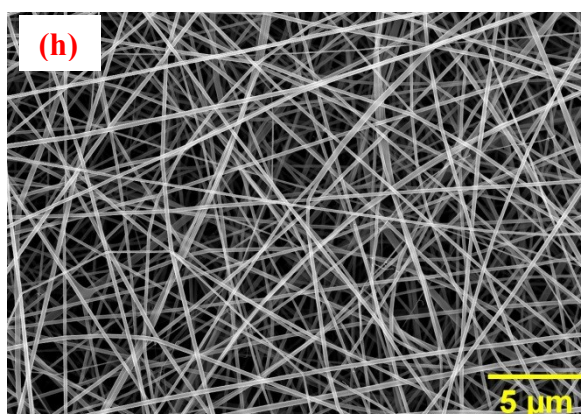
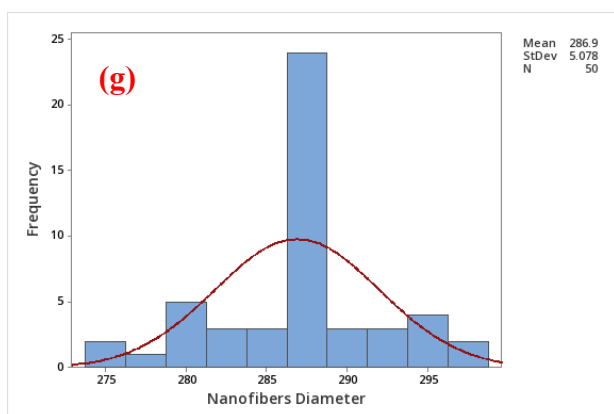
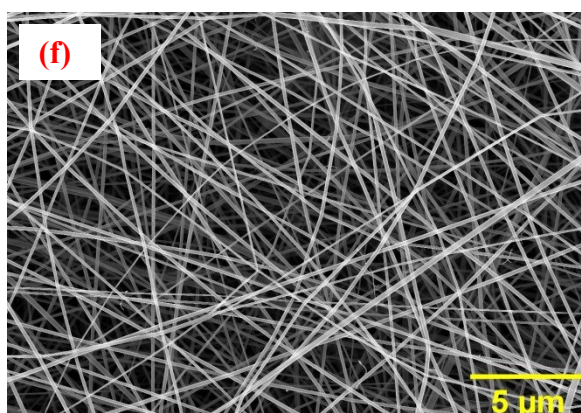
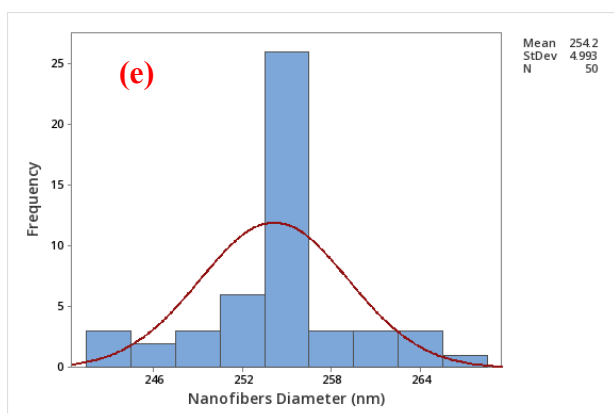
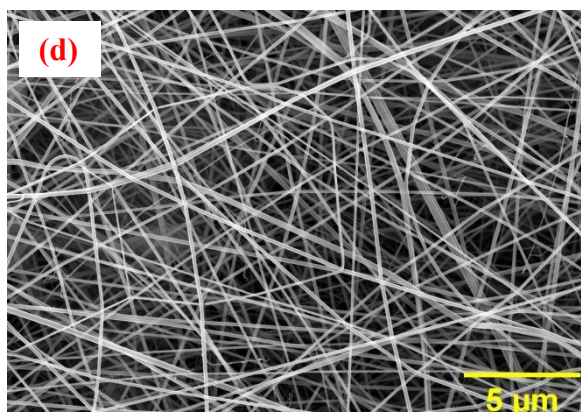
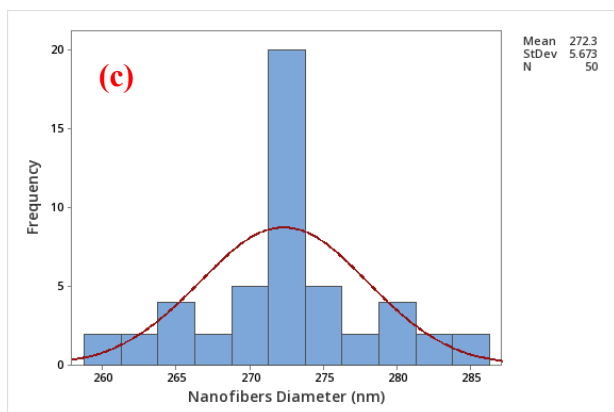


Figure A-1. SEM micrographs and nanofibers diameter distribution corresponding to the experimental run numbers in Table A-1, as follows: (a,b) 1, (c,d) 9, (e,f) 20, and (g,h) 30.

Table A-1: Experimental design and results

Run Order	Applied Voltage (kV)	Spinning Distance (cm)	Polymer Conc. (wt.%)	Flow Rate (ml/hr)	Conc of Nacl (wt.%)	Nanofibers Diameter (nm)
1	23	22	9.40	1.35	0.55	302.70
2	22	24	10.30	1.70	0.80	305.10
3	22	20	10.30	1.00	0.80	346.90
4	24	20	8.50	1.00	0.80	231.30
5	23	22	9.40	1.35	0.55	302.70
6	23	22	9.40	0.65	0.55	287.10
7	23	22	9.40	1.35	0.55	274.00
8	22	20	8.50	1.70	0.80	277.20
9	23	22	7.60	1.35	0.55	272.20
10	24	24	10.30	1.70	0.30	311.50
11	22	24	10.30	1.00	0.30	313.70
12	23	18	9.40	1.35	0.55	319.80
13	21	22	9.40	1.35	0.55	323.50
14	22	20	8.50	1.00	0.30	294.30
15	23	22	9.40	1.35	0.55	300.20
16	23	22	9.40	1.35	0.05	301.00
17	23	22	9.40	1.35	0.55	285.30
18	23	22	9.40	1.35	0.55	294.60
19	23	26	9.40	1.35	0.55	263.40
20	22	24	8.50	1.70	0.30	254.20
21	23	22	9.40	2.05	0.55	287.00
22	23	22	11.20	1.35	0.55	405.10
23	23	22	9.40	1.35	1.05	269.90
24	24	24	8.50	1.00	0.30	255.80
25	23	22	9.40	1.35	0.55	276.70
26	24	24	10.30	1.00	0.80	276.80
27	24	20	8.50	1.70	0.30	245.10
28	22	20	10.30	1.70	0.30	390.10
29	22	24	8.50	1.00	0.80	302.10
30	23	22	9.40	1.35	0.55	286.90
31	24	24	8.50	1.70	0.80	239.60
32	23	22	9.40	1.35	0.55	285.40
33	24	20	10.30	1.70	0.80	299.10
34	23	22	9.40	1.35	0.55	288.60
35	25	22	9.4	1.35	0.55	260.00
36	24	20	10.30	1.00	0.30	312.10

## A-2: Estimation of the model coefficient

The full second-order polynomial approximation of the response surface model was evaluated by conducting an analysis of variance (ANOVA) on the response at 95% confidence level. The results are presented in Table A2.

Table A-2: Estimation of the model coefficient and corresponding p-values

Source	Sum of Squares	DF	f-values	p-values
Model	42,546.43	17	24.12	<0.0001
V	8041.77	1	77.49	<0.0001
D	2606.25	1	25.11	<0.0001
P	21,690.09	1	209.03	<0.0001
F	5.32	1	0.05	0.8234
N	1078.70	1	10.40	0.0047
VD	1048.14	1	10.10	0.0052
DP	1312.25	1	12.65	0.0023
VF	154.38	1	1.49	0.2383
DF	263.25	1	2.54	0.1286
PF	956.36	1	9.22	0.0071
VN	200.93	1	1.94	0.1810
DN	356.27	1	3.43	0.0804
PN	628.76	1	6.06	0.0242
FN	223.33	1	2.25	0.1511
P <sup>2</sup>	3544.12	1	34.16	<0.0001
F <sup>2</sup>	180.658	1	1.74	0.2035
N <sup>2</sup>	246.61	1	2.38	0.1406
Lack of fit	933.09	9	0.99	0.5010
Pure error	934.65	9		
Cor total	44,414.16	35		

$$R^2 = 0.96, \text{ Adj. } R^2 = 0.92$$

According to the study's findings, the terms V, D, P, N, VD, DP, PF, PN, and  $P^2$  were determined to be significant in the model. To confirm the significance level of the model terms, the f-value was utilized, which indicates the magnitude of influence each term has on the studied process. A higher f-value represents a greater impact on the process. These f-values align with the p-values and their corresponding results. Therefore, the study's findings regarding the f-values support those of the p-values [147]. These results are consistent with the results obtained while investigating the influence of process parameters on morphology and diameter of electrospun  $Nb_{18}W_{16}O_{93}$  nanofibers.